DRAFT RESEARCH REPORT
Agreement T4118, Task 05
Rapid Construction
TNW 2008-06
TransNow Budget No. 61-4161

A Precast Concrete Bridge Bent Designed to Re-center after an Earthquake

by

Laila S. Cohagen
Graduate Research Assistant

Jason B.K. Pang
Graduate Research Assistant

John F. Stanton
Professor

Marc O Eberhard
Professor

Department of Civil and Environmental Engineering
University of Washington, Box 352700
Seattle, Washington 98195

Washington State Transportation Center (TRAC)
University of Washington, Box 354802
1107NE 45th Street, Suite 535
Seattle, Washington 98105-4631

Washington State Department of Transportation Technical Monitor
Jugesh Kapur, Bridge Design Engineer

Sponsored by

Transportation Northwest (TransNow)
University of Washington
129 More Hall, Box 352700
Seattle, Washington 98195-2700

Washington State Transportation Commission
Department of Transportation
Olympia, Washington 98504-7370

and in cooperation with
U.S. Department of Transportation
Federal Highway Administration

August 2008

TECHNICAL REPORT STANDARD TITLE PAGE

1. REPORT NO.	2. GOVERNMENT ACCESSION NO.	3. RECIPIENT'S CATALOG NO.
WA-RD 684.3/ TNW 2008-06		

4. TITLE AND SUBTITLE	5. REPORT DATE
A PRECAST CONCRETE BRIDGE BENT DESIGNED TO RE-CENTER AFTER AN EARTHQUAKE	August 2008
	6. PERFORMING ORGANIZATION CODE

7. AUTHORS	8. PERFORMING ORGANIZATION CODE
Laila Cohagen, Jason B.K. Pang, Marc O. Eberhard, John F. Stanton	

9. PERFORMING ORGANIZATION NAME AND ADDRESS		10. WORK UNIT NO.
Transportation Northwest Regional Center X (TransNow) Box 352700, 129 More Hall University of Washington Seattle, WA 98195-2700	Washington State Transportation Center (TRAC) University of Washington 1107 NE 45th St, Suite 535 Seattle, WA 98105	11. CONTRACT OR GRANT NUMBER Contract T4118, Task 05 DTRS99-G-0010

12. SPONSORING AGENCY NAME AND ADDRESS		13. TYPE OF REPORT AND PERIOD COVERED
Washington State Dept of Transp. Transportation Building, MS 47372 Olympia, Washington 98504-7372 Kim Willoughby, 360-705-7978	U.S. Department of Transportation Office of the Secretary of Transp. 400 7th St. SW Washington, DC 20590	Draft Research Report 14. SPONSORING AGENCY CODE

15. SUPPLIMENTARY NOTES

16. ABSTRACT

In this study the post-earthquake residual displacements of reinforced concrete bridge bents were investigated. The system had mild steel that was intended to dissipate energy and an unbonded, post-tensioned tendon that was supposed to remain elastic and re-center the column. The columns tested had different mild steel to prestress ratios, which affected their re-centering ability. A re-centering ratio developed by Hieber (2005), which took into account the external axial load, initial prestress force, and the mild steel ratio, was used to predict these re-centering capabilities.

Two 40 percent scale specimens with large-bar connection details and a central unbonded, post-tensioned tendon were tested by using pseudo-static loading. The large-bar system is a rapidly constructible precast system for use in seismic regions. The test columns had re-centering ratios of 1.6 and 1.2. A column with the same connection details but no prestress and a re-centering ratio of 0.9 was used as a reference. The displacement at zero force in the test was used as a proxy for the residual displacement after an earthquake.

The tests showed that columns with a larger re-centering ratio did experience lower residual drifts, although this distinction only became clear for drift ratios that exceeded 2 percent. The tests also showed that increases in post-tensioning force led to slight increases in damage at high drift ratios.

17. KEY WORDS	18. DISTRIBUTION STATEMENT
Posttensioning, precast concrete, bridge substructure, columns, residual displacement, residual drift	

19. SECURITY CLASSIF. (of this report)	20. SECURITY CLASSIF. (of this page)	21. NO. OF PAGES	22. PRICE

DISCLAIMER

The contents of this report reflect the views of the authors, who are responsible for the facts and accuracy of the data presented herein. This document is disseminated through the Transportation Northwest (TransNow) Regional Center under the sponsorship of the U.S. Department of Transportation UTC Grant Program and through the Washington State Department of Transportation. The U.S. Government assumes no liability for the contents or use thereof. Sponsorship for the local match portion of this research project was provided by the Washington State Department of Transportation. The contents do not necessarily reflect the views or policies of the U.S. Department of Transportation or Washington State Department of Transportation. This report does not constitute a standard, specification, or regulation.

TABLE OF CONTENTS

Page

Executive Summary ..... **xi**

Objective xi
Background xi
Results xii
Conclusions xiii

Chapter 1: Introduction **1**

1.1 Rapid Construction of Bridges 1
1.2 Re-Centering Systems 2
1.3 Research Scope and Objectives 3

Chapter 2: Development of the Re-Centering Large-Bar Connection **4**

2.1 Description of the Large-Bar Connection 4
2.2 Re-centering Ratio 6
2.3 Development of the Large-Bar Connection with Post-Tensioning 9
2.4 Application of the Post-Tensioned Connection to Practice 13

Chapter 3: Experimental Program **16**

3.1 Overview 16
3.2 Specimen Construction 17
3.2.1 Construction Overview 17
3.2.2 Cap-Beam and Vertical Bar Construction 17
3.2.3 Column and Loading Ring Construction 19
3.2.4 Post-Tensioning Installation and Stressing 20
3.3 Test Set-up 23
3.4 Displacement History 25
3.5 Instrumentation 26
3.5.1 Load Cells 26
3.5.2 Linear Potentiometers 28
3.5.3 Strain Gages 29
3.6 Data Acquisition and Documentation 31

Chapter 4: Damage Progression **33**

4.1 Definitions of Damage States 33
4.2 Specimen LB7-PT 34
4.3 Specimen LB6-PT 39
4.4 Comparison of Specimen Damage Progression 42

Chapter 5: Measured Response **45**

5.1 Material Test Results 45
5.1.1 Concrete Strength 45
5.1.2 Grout Strength 45
5.1.3 Mild Reinforcement Stress-Strain Results 45
5.1.4 PT Bar Stress-Strain Results 46

5.2 Friction Correction 47
5.3 Moment-Drift Response 48
5.4 Effective Force 53
5.5 Column Rotation 54
5.6 Column Curvature 57
5.7 Axial force in the PT Bar 59
5.8 Column Axial Lengthening 65
5.9 Strains in Mild Steel Reinforcement 66
5.9.1 Strain Distributions 66
5.9.2 Bar Curvatures 70

Chapter 6: Data Analysis 72

6.1 Strength Degradation 72
6.2 Energy Dissipation 73
6.3 PT Bar Behavior 78
6.4 Column Residual Displacements 82
6.5 Effectiveness of Re-Centering Ratio at Predicting Residual Displacements 86
6.6 Debonding of Mild Steel Reinforcing Bars 89
6.7 Analysis of Curvatures of Mild Steel Reinforcing Bars 90

Chapter 7: Comparison with Performance Models 92

7.1 Damage Progression Models 92
7.2 Force-Deformation Models 94
7.3 Comparison with ACI Nominal Flexural Strength 99

Chapter 8: Summary and Conclusions 10

8.1 Summary 100
8.2 Conclusions 101
8.3 Recommendations for Further Research 102

References **..... 103**

Appendix A: Specimen Construction Drawings A-1

Appendix B: Material Tests B-1

B.1 Concrete Strengths B-1
B.2 Grout Strengths B-2
B.3 Mild Steel Reinforcement Stress-Strain Behavior B-3
B.4 PT Bar Stress-Strain Behavior B-5

Appendix C: Re-centering Ratio Calculations C-1

Appendix D: Debonded Length Calculations D-1

Appendix E: Bar Curvature Schematics E-1

LIST OF FIGURES

Figure Number *Page*

Figure 2-1. Two-column bent. (figure from Steuck et al. 2007).....4
Figure 2-2. Pang (2008) test specimen schematic. 5
Figure 2-3. Counteracting forces used to calculate the re-centering ratio. 7
Figure 2-4. Nominal re-centering ratios for three cases of mild steel stresses. 9
Figure 2-5. Post-tensioned specimen schematic. 13
Figure 2-6. Re-centering bridge bent with prestressing strands. 15

Figure 3-1. Column vertical bar naming convention. 17
Figure 3-2. Specimen LB7-PT cap-beam after casting.....18
Figure 3-3. Loading Ring above specimen. 20
Figure 3-4. Close up of loading ring.....20
Figure 3-5. Section through the PT bar stressing setup. 21
Figure 3-6. Prestress force in post-tension bar over time, from initial stressing. 22
Figure 3-7. Specimen test setup. 24
Figure 3-8. Target displacement history. 25
Figure 3-9. Post-tensioned bar load-cell set-up. 27
Figure 3-10. Location of potentiometers. 28
Figure 3-11. Location of specimen strain gauges. 29
Figure 3-12. Strain gauge after gluing (picture courtesy of Jason Pang).....31
Figure 3-13. Two gauges at different stages of protecting. 31
Figure 3-14. Location of cameras (plan view). 32

Figure 4-1. LB7-PT: moment vs. drift ratio with major damage states marked. 35
Figure 4-2. LB7-PT: column flexural cracks, Cycle 5 (0.25%).....36
Figure 4-3. LB7-PT: onset of crushing, Cycle 20 (1.41%).....36
Figure 4-4. LB7-PT: south side, onset of column crushing, Cycle 22 (-1.85%). 36
Figure 4-5. LB7-PT: north side, Cycle 24 (2.26%). 36
Figure 4-6. LB7-PT: Bar V18 buckling and spiral necking, Cycle 32 (5.43%). 37
Figure 4-7. LB7-PT: spiral fracture, Cycle 32 (-5.32%).....37
Figure 4-8. LB7-PT: Bar V00 fracture, Cycle 35 (2.11%). 38
Figure 4-9. LB7-PT: Bar V18, Cycle 37 (-9.55%). 38
Figure 4-10. LB6-PT: moment drift ratio with major damage states marked. 39
Figure 4-11. LB6-PT: column flexural cracks, Cycle 9 (-0.47%). 40
Figure 4-12. LB6-PT: column flexural cracks, Cycle 20 (-1.53%). 40
Figure 4-13. LB6-PT: Cycle 24 (4.17%), tension side. 41
Figure 4-14. LB6-PT: Cycle 24 (4.17%), compression side.....41
Figure 4-15. LB6-PT: Bar V00 buckled and spiral fractured, Cycle 32 (-5.38%). 42
Figure 4-16. LB6-PT: Bar V00 fractured, Cycle 33 (6.75%). 42
Figure 4-17. LB6-PT: Maximum spall height at end of test. 42
Figure 4-18. Comparison of specimens' drift ratios for the major damage states. 44

Figure 5-1. Friction force model. 48

Figure 5-2. Approximating lateral displacements at the applied vertical load. 49
Figure 5-3. Specimen LB6-PT: moment-drift response. 50
Figure 5-4. Specimen LB7-PT: moment-drift response. 50
Figure 5-5. Comparison of moment-drift responses. 51
Figure 5-6. Normalized moment-drift comparison. 52
Figure 5-7. Specimen LB6-PT: effective force vs. displacement. 53
Figure 5-8. Specimen LB7-PT: effective force vs. displacement. 54
Figure 5-9. Schematic of the column-rotation instruments. 55
Figure 5-10. Specimen LB6-PT: column segment rotations. 56
Figure 5-11. Specimen LB7-PT: column segment rotations. 56
Figure 5-12. Comparison of interface rotations for cycle peak drift ratios. 57
Figure 5-13. Specimen LB6-PT: distribution of column curvatures. 58
Figure 5-14. Specimen LB7-PT: distribution of column curvatures. 58
Figure 5-15. Specimen LB6-PT: force in the PT bar vs. drift ratio. 60
Figure 5-16. Specimen LB7-PT: force in the PT bar vs. drift ratio. 60
Figure 5-17. Specimen LB6-PT: normalized force of the PT bar vs. drift ratio. 61
Figure 5-18. Specimen LB7-PT: normalized force in the PT bar vs. drift ratio. 62
Figure 5-19. Comparison of the envelope plots for PT force. 63
Figure 5-20. Comparison of the rate of increase of force in the PT bar. 64
Figure 5-21. Comparison of normalized PT force at zero drift 64
Figure 5-22. Specimen LB6-PT: axial lengthening of the column. 65
Figure 5-23. Specimen LB7-PT: axial lengthening of the column. 66
Figure 5-24. Specimen LB6-PT: strain profiles for Bar V00. 67
Figure 5-25. Specimen LB6-PT: strain profiles for bar V18. 68
Figure 5-26. Specimen LB7-PT: strain profiles for Bar V00. 68
Figure 5-27. Specimen LB7-PT: strain profiles for Bar V18. 69
Figure 5-28. Specimen LB6-PT: curvature profile for Bar V00. 70
Figure 5-29. Specimen LB7-PT: curvature profile for Bar V00. 71
Figure 5-30. Specimen LB7-PT: curvature profile for Bar V18. 71

Figure 6-1. Comparison of effective-force vs. drift ratio. 72
Figure 6-2. Normalized effective force vs. drift ratio. 73
Figure 6-3. Example of energy dissipation calculations for one cycle. 74
Figure 6-4. Above: energy dissipation per cycle. 75
Figure 6-5. Normalized energy dissipation per cycle. 76
Figure 6-6. Normalized energy dissipation for cycles 17-34. 77
Figure 6-7. Comparison of the equivalent viscous damping coefficient per cycle. 78
Figure 6-8. Equivalent viscous damping coefficients vs. drift ratio. 78
Figure 6-9. LB6-PT: PT force vs. column axial lengthening. 79
Figure 6-10. LB7-PT: PT force vs. column axial lengthening. 80
Figure 6-11. Comparison of tension tests and Specimen LB6-PT bar stress. 81
Figure 6-12. Comparison of tension tests and Specimen LB7-PT bar stress. 81
Figure 6-13. Explanation of terms used to calculate the residual displacements. 82
Figure 6-14. Comparison of the normalized residual displacement. 83
Figure 6-15. Normalized hysteresis curve slopes at zero force vs. drift-ratio. 85
Figure 6-16. Comparison of hysteresis loop shapes for a cycle. 86

Figure 6-17. Re-centering ratio at zero drift vs. peak drift. 87
Figure 6-18. Re-centering ratio at zero lateral force vs. peak drift. 88
Figure 6-19. Residual displacement vs. re-centering ratio. 89

Figure 7-1. Comparison of damage model predictions and observed occurrences 93
Figure 7-2. Displacement components' contribution to total at initial yield 96
Figure 7-3. Specimen LB6-PT force-displacement envelopes (with $P_{PT,\ initial}$). 97
Figure 7-4. Specimen LB7-PT force-displacement envelopes (with $P_{PT,\ initial}$). 97

Figure A-1. Specimen west elevation. A-1
Figure A-2. Specimen north elevation. A-2
Figure A-3. Above: Specimen cap beam plan view. Below: Cap-beam section. A-3
Figure A-4. Specimen cap-beam sections. A-4
Figure A-5. PT bar unbonded length and setup. A-5

Figure B-1. Concrete strength results. B-1
Figure B-2. Grout cube strengths. B-3
Figure B-3. Stress-strain curve for the #6 reinforcing bars. B-4
Figure B-4. Stress-strain curve for the #7 reinforcing bars. B-4
Figure B-5. Stress-strain curve for the #3 reinforcing bars. B-5
Figure B-6. Stress-strain curve for the unused PT bar. B-6
Figure B-7. Stress-strain curve for the used (LB7-PT) PT bar. B-6
Figure B-8. PT bar used in tension test. B-7

Figure C-1. Column cross section. C-2

Figure D-1. Parameters used for calculating the bar elongation. D-1
Figure D-2. Debonded length of the mild steel rebar vs. drift ratio D-3

LIST OF TABLES

Table Number *Page*

Table 2-1. Test specimen design parameters. 10
Table 2-2. Possible prestress configurations. 14

Table 3-1. Test matrix 16
Table 3-2. Target and actual prestress force at the beginning of the test. 23
Table 3-3. Target displacement history. 26
Table 3-4. Strain gauge types used in the specimens. 30

Table 4-1. Key damage types. 33
Table 4-2. Specimen LB7-PT key damage states. 34
Table 4-3. Specimen LB6-PT key damages states. 39
Table 4-4. A comparison of the specimens' drift ratios. 44

Table 5-1. Average concrete strength on day of test. 45
Table 5-2. Measured mild steel properties. 46
Table 5-3. Peak measured responses. 51
Table 5-4. Summary of key PT forces. 59

Table 7-1. Comparison of damage model predictions and observed occurrences. 94
Table 7-2. Comparison of damage model predictions and observed occurrences. 95
Table 7-3. Results from moment-curvature analysis. 95
Table 7-4. Displacement components at initial yield 96
Table 7-5. Comparison of results: model vs. measured. 98
Table 7-6. Comparison of results: ACI vs. measured. 99

Table B-1. Concrete cylinder strength test results. B-1
Table B-2. Specimen LB7-PT grout cube strengths. B-2
Table B-3. Specimen LB6-PT grout cube strengths. B-2
Table B-4. PT bar section lengths for test to 250 kips. B-9
Table B-5. PT bar section lengths for test to ultimate load and fracture. B-10

Table C-1. Three cases of stress value assumptions in the column bars. C-3

Table E-1. Bar curvature schematics. C-2

EXECUTIVE SUMMARY

Objective

In this study the post-earthquake residual displacements of reinforced concrete bridge bents were investigated. The system had mild steel that was intended to dissipate energy and an unbonded post tensioned tendon that was supposed to remain elastic and re-center the column. The columns tested had different mild –steel –to prestress ratios, which affected their re-centering ability. A re-centering ratio developed by Hieber (2005) that took into account the external axial load, initial prestress force, and the mild steel ratio was used to predict these re-centering capabilities.

Background

The large-bar system is a precast cap-beam-to-column connection system intended to accelerate construction through the use of prefabricated components. It is also suitable for use in seismic regions. The connection uses a few large, longitudinal bars that extend out of the column into large grouted ducts in the cap beam, which provide high construction tolerances. It also provides other benefits of precast construction. such as reducing traffic disruption, improving work-zone safety, lessening environmental impacts, and lowering life-cycle costs (Hieber et al., 2005a). This system was tested, without any prestress, by Pang (2008).

The system tested in this study featured details similar to those in the columns tested by Pang (2008), with an unbonded PT bar located at the center of the column. For large-scale columns, strands might prove more practical. Because the PT bar was unbonded, strain increases were distributed over the whole length of the bar. This allowed the bar to remain elastic at large displacements and thus provide a restoring force to the basic large-bar system. This force was intended to reduce the residual displacements of the columns following an earthquake. Reducing the residual displacements could make the difference between a bridge being open or closed directly following an earthquake.

Two column-to-cap-beam connections were tested at 40 percent scale as a part of this study, with the primary variable being the prestress to mild steel ratio. Re-centering

ratios larger than 1.0 were expected to improve a column's ability to re-center (Hieber 2005). To evaluate this expectation the columns were constructed with re-centering ratios of 1.2 and 1.6. These values were achieved primarily by changing the size of the mild steel reinforcing bars. The initial prestress force was also changed slightly, while the PT bar size remained the same for both columns. A comparable non-PT column from Pang (2008) was used as a reference; it had a re-centering ratio of 0.9. All columns were designed to have roughly the same flexural strength.

Results

The damage progression was similar for both the PT specimens and the non-PT one. Early damage states, such as significant crack formation and significant spalling, occurred later in the PT specimens than in the non-PT specimen. In contrast, the later and more serious damage states, such as bar buckling, first spiral fracture, and first bar fracture, occurred at slightly lower drifts for the PT specimens. The earlier occurrences of bar buckling and fracture in the PT specimens, in comparison to the non-PT one, was expected because the PT bar elongated and the force in it increased when it was displaced laterally. These damage states could possibly be delayed with the addition of a jacket around the column in the plastic hinge area.

Both PT specimens resisted at least 80 percent of their peak strength until a drift ratio of 4 percent. For drift ratios above about 1.5 percent, the energy dissipation increased with an increase in the mild steel ratio, as was expected. Before that point the energy dissipation was small and similar for all specimens.

The displacements of the column at zero applied force are an indirect measure of the expected residual displacements. These displacements were inversely correlated with the column's re-centering ratio for drifts of larger than 2 percent. At lower drifts, these displacements were small for all specimens. The PT bars started to exhibit non-linear behavior when they reached a load of about 170 kips (107 ksi on the nominal bar area); this happened at around a drift ratio of 2 percent in both specimens. The gradual yielding of the PT bars reduced the re-centering abilities of the columns.

Conclusions

- A larger re-centering ratio improves the re-centering abilities of the PT bar for drifts that exceed 2 percent.
- To maximize the re-centering capabilities of the PT bar, the bar stress should be kept within the proportional limit. This constraint should guide the selection of the bar size and initial bar stress.
- The energy dissipated is determined mainly by the mild steel ratio.
- An increase in the post-tensioning force led to slight increases in damage at high drift ratios.

CHAPTER 1: INTRODUCTION

1.1 Rapid Construction of Bridges

Several research projects at the University of Washington (Hieber et al., 2005a, Wacker et al., 2005, Steuck et al., 2007, and Pang, 2008) have focused on accelerating the construction of bridges in seismic regions by using precast concrete components. The use of precast components, as opposed to casting on site, has a number of benefits. Not only does this approach shorten construction time, but it also reduces traffic disruption, improves work-zone safety, lessens environmental impacts, improves constructability, and lowers life-cycle costs (Hieber et al., 2005a). In any precast structure, the connections between components are the most susceptible to damage. Most applications of precast bridge structures have been in regions of low seismicity where connection damage is not of great concern (Hieber et al., 2005b). However, in seismic regions, concerns about connection damage have limited the use of precast bridge sub-structures.

Hieber et al. (2005a) analyzed the performance of two types of precast concrete bridge pier systems under seismic loads. One system contained only mild steel reinforcing bars, whereas the second, hybrid, system also included unbonded post-tensioning intended to improve the re-centering of the system. The study concluded that both systems would perform well but that further tests on the connection details should be performed. Wacker et al. (2005) developed two design procedures, a force-based and a displacement-based method, to design both the mild steel and hybrid precast systems.

Research at the University of Washington also identified several precast cap-beam-to-column systems that provide the benefits of rapid bridge construction. These systems are listed in Steuck et al. (2007). The large-bar system was chosen from that list for experimental testing. Monotonic pullout tests of up to full-size reinforcing bars were conducted to ensure that adequate bond existed (Steuck et al. 2007). Testing of the system had to be scaled down because of limits on the size of the available testing equipment. Three scaled tests of the system and one reference test column were completed by Pang (2008). The tests showed that the proposed system would perform as well as traditional cast-in-place columns under seismic loading.

1.2 Re-Centering Systems

The goal of the re-centering system is to minimize the residual displacements of a bridge bent system following a seismic event. This goal is accomplished by including in the system an element that remains elastic throughout the event, which provides the system with a restoring force. High-strength, unbonded, prestressed tendons (bars or strands) have typically been used for this purpose. By virtue of being unbonded, the tendons are free to move relative to the concrete, so that increases in bar length are distributed over the whole unbonded length. This allows the system to reach a larger displacement without yielding the restoring element (Stanton et al. 1997).

In some systems this concept has been applied along with regular reinforcing bars (mild steel) that provide the system with the energy dissipation needed to limit the maximum displacements. The mild steel also provides flexural strength, as well as a means of confining the core (Stanton et al. 1997, AASHTO 2005).

A precast hybrid frame system for improved seismic performance was designed and tested in the PRESSS program (Stanton et al. 1997). This system incorporated an unbonded, post-tensioned tendon designed to remain elastic and thus supply a restoring force that would minimize residual displacements. The system also included mild reinforcing bars that would fulfill the typical function of increasing the flexural strength and would yield cyclically and dissipate the energy produced during a seismic event. This design allowed the beam ends to rock against the column faces in an earthquake with nearly all the deformations occurring at that interface, thus reducing the damage to the beams themselves (Stanton et al. 1997). Later stages of the program included testing of a scaled five-story precast test building that incorporated the hybrid frame system, as well as three other frame systems and a jointed shear wall system with re-centering abilities (Nakaki et al. 1999).

Palermo, Pampanin and Calvi (2005) extended the idea of improved seismic performance of the hybrid system from precast concrete buildings to bridge piers and systems.

At the University of Berkeley, Jeong (2005) studied the performance of cast-in–place hybrid bridge columns in a series of shaking table tests. He investigated the effects of the level of prestress force, the extent of debonding of the mild steel, and the existence

of steel jacketing on the re-centering ability of the columns. Work on modeling the behavior of hybrid columns to predict the re-centering behavior was also conducted.

1.3 Research Scope and Objectives

Previous research by Steuck et al. (2007) and Pang (2008) demonstrated that the large-bar bridge bent connection performs as well as, or better than, a conventional cast-in-place connection under seismic loading. This study built on that research, using the same connection configuration, by adding an unbonded post-tensioned bar with the intent of minimizing residual column displacements.

The objectives of this research were to study the effects of the relative proportions of prestress and mild steel on column re-centering, and to determine whether a simple equation (Hieber 2005) could be used as a guideline for predicting this re-centering ability.

Two columns were constructed with different prestressed –to mild steel ratios; one had a high re-centering ratio and the other had a lower one. A comparable column from Pang (2008), with the same connection details except without prestress, was used as a reference.

Chapter 2 describes the details of the large-bar connection and the changes made to incorporate the post-tensioned bar. The specimen construction, set-up, instrumentation, and test procedure are presented in Chapter 3. Experimental test observations are described in Chapter 4. Chapter 5 describes the measured response of the test specimens. Chapter 6 discusses the performance of the specimens and compares their behavior. Test observations and measurements are compared with analytical models in Chapter 7. Conclusions and research recommendations are provided in Chapter 8.

CHAPTER 2: DEVELOPMENT OF THE RE-CENTERING LARGE-BAR CONNECTION

2.1 Description of the Large-Bar Connection

University of Washington researchers, working with engineers from the Washington State Department of Transportation (WSDOT), selected the large-bar connection from a list of candidate connection types (Pang 2008). The advantages of this system are its short construction time, generous construction tolerances, and good seismic performance (Steuck et al. 2007). This system had been tested (Pang 2008) in its basic form, which contains no prestressed reinforcement. That system is described briefly below, as a precursor to describing the modifications included to prestressing.

Pang tested a precast cap-beam to precast column connection from a multi-column bent cap.

Figure 2-1 shows the schematic of a two-column bent with the tested portion boxed. The specimens tested by Pang (2008) were scaled at 40 percent of a prototype bridge typical of bridges in the state of Washington.

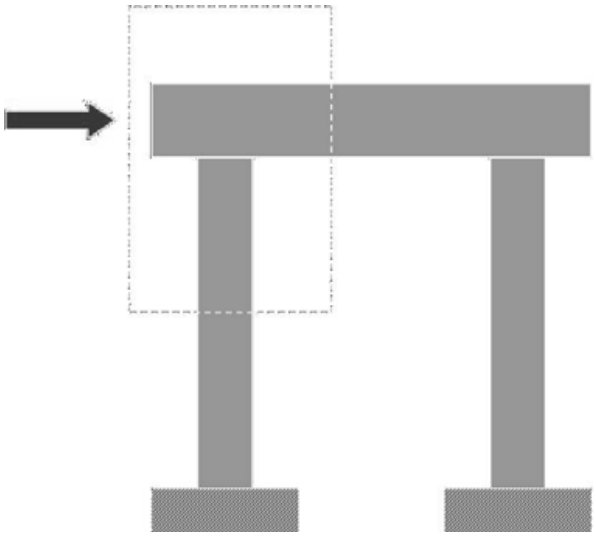

Figure 2-1. Two-column bent (Steuck et al. 2007).

The test columns had a diameter of 20 in. and a cantilever aspect ratio of 3. They were reinforced longitudinally with six #8 bars that extended up from the column and

into ducts in the cap-beam. The columns also had twelve #3 bars that terminated at the column interface, which were included to satisfy AASHTO requirements for core confinement (AASHTO 2005). For two of Pang's specimens (LB8-D1 and LB8-D2), the #8 bars were debonded for 8 in. below the interface to reduce strain concentrations. The column was reinforced transversely with a 0.25-in. diameter spiral with a center-to-center spacing of 1.25 in. The schematic drawing of the system in Figure 2-2 shows the column bars, ducts, and debonded section in Pang's test specimen. The reinforcement in the beam and transverse reinforcement in the column are not shown.

The precast beam was 36 in. high, 78 in. long and 25 in. wide. It approximated the full height of the scaled cap-beam, as well as a portion of the diaphragm. The #8 reinforcing bars fit into 17.5-in. long, 4-in. diameter ducts in the cap beam that were grouted with high-strength grout.

The specimens were tested upside down. The beam was anchored to the test floor, and axial load was applied to the column.

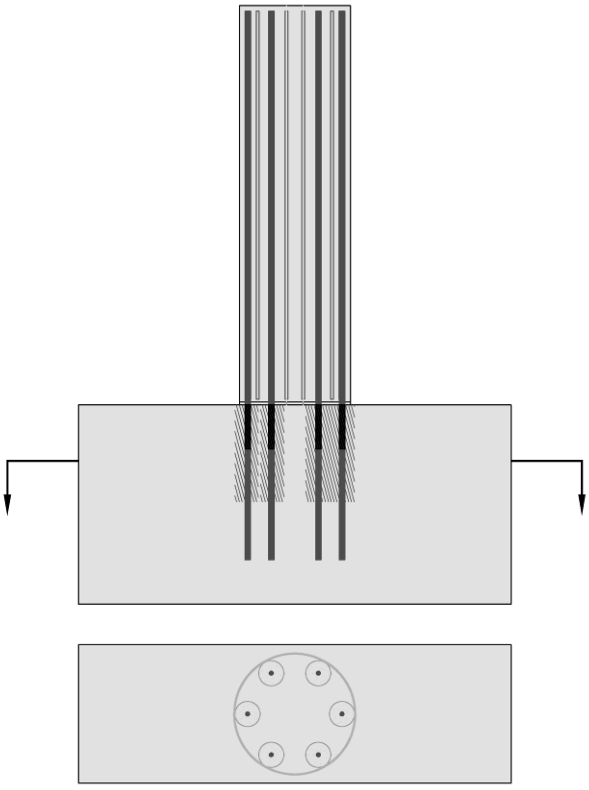

Figure 2-2. Pang (2008) test specimen schematic.

2.2 Re-centering Ratio

The objective of this research was to identify how varying the ratio of post-tensioning steel to mild steel would affect the force-displacement hysteresis, which affects the residual displacements. The moment strengths of the post-tensioned columns were kept close to the moment strengths of the previously tested, non-post-tensioned columns.

Hieber (2005) numerically examined the behavior of both cast-in-place reinforced concrete columns and hybrid (prestress and mild steel) columns. He defined a re-centering ratio, λ_{re}, to evaluate the hybrid columns' ability to re-center. The key parameter in the study was the column re-centering ratio, which is discussed below.

The following parameter was defined to help derive the re-centering ratio: αD = distance from the center of the column to the centroid of the concrete compression area. It is also assumed that at this critical location all the mild steel bars yield in compression and that a uniform concrete compressive stress exists over the cross-section. The total resisting force of the mild steel is then $F_s = A_s \cdot f_y$ and the force in the post-tension bar is then $F_p = A_p \cdot f_{po}$. If moments are taken about the centroid of the compression side, the re-centering or closing moment becomes:

$$M_{closing} = \left(P_{col} + F_p\right) \cdot \alpha D \qquad \textbf{2-1}$$

The resisting moment is:

$$M_{resisting} = F_s \cdot \alpha D \qquad \textbf{2-2}$$

If the closing moment exceeds the resisting moment, re-centering of the column is expected to happen. Combining equations 2-1 and 2-2,

$$\lambda_{re} = \frac{M_{closing}}{M_{resisting}} = \frac{P_{col} + F_p}{F_s} \qquad \textbf{2-3}$$

Assuming that the mild steel has yielded and that the PT has its initial stress, Equation 2-3 can be expressed as:

$$\lambda_{re} = \frac{P_{col} + A_p \cdot f_{po}}{A_s \cdot f_y} \qquad \textbf{2-4}$$

where

P_{col} = column axial load

A_p = total area of the prestress bars

f_{po} = initial prestress in the bar

A_s = total area of mild steel

f_y = yield strength of the mild steel.

This equation states that if the total compressive load on the column due to both axial load and prestess force is higher than the resisting yield-force of the mild steel reinforcement, then the re-centering ratio is larger than 1.0 and the column is likely to re-center. Figure 2-3 shows these counteracting forces that were used to calculate the re-centering ratios.

As a column goes through lateral displacement, the post-tensioned bar elongates and the bar force increases; if the post-tensioned bar remains elastic this will increase the re-centering ability. Therefore, the critical position for re-centering (minimum post-tensioning force) is when the column is close to vertical and the stress in the bar is at a minimum for that cycle.

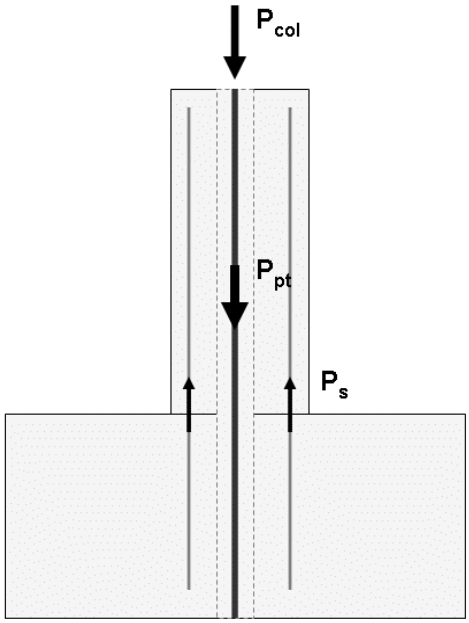

Figure 2-3. Counteracting forces used to calculate the re-centering ratio.

Equation 2-4 assumes that no post-tensioning is lost and that all the mild steel bars are at a stress of f_y in compression. In practice these conditions are unlikely to be met, so a value of $\lambda_{re} = 1$ will not represent a binary separation between significant residual drift and perfect re-centering. For example, concrete crushing during rocking would lead to partial loss of prestress, and cyclic yielding of the mild steel would induce the Bauschinger effect and eliminate the sharp yield point.

In addition, it is unlikely that all of the mild steel will be exactly at the yield stress. As the column is displaced in one direction, the bars in the concrete compression area could easily yield in compression and the bars in the tension area could yield in tension and pass their yield point. When the column displacement is reversed and the column is close to zero displacement, it is probable that the compressive stresses in the bars in the compression area will have decreased and could even possibly have become tensile. Similarly, the bars in the tension area could then yield in compression before the zero displacement is reached. To predict the exact stresses in the rebar, it would be necessary to keep track of the cyclic displacement history, as well as the amount of yielding in tension and compression by using a cyclic stress-strain model.

Two other sets of assumptions for stresses in the mild steel bars were considered for exploring the sensitivity of the re-centering parameter. In the first of these, three of the six bars were assumed to be yielding in compression, but the other three had a stress of zero. The second, additional case again assumed that three bars were yielding in compression, but two bars had zero stress and one bar had a tensile stress equal to a quarter of the yield stress. It is likely that the true value of λ_{re} is bounded by these values. The re-centering ratio for these three cases is given in Figure 2-4. The calculations of these values can be found in Appendix C.

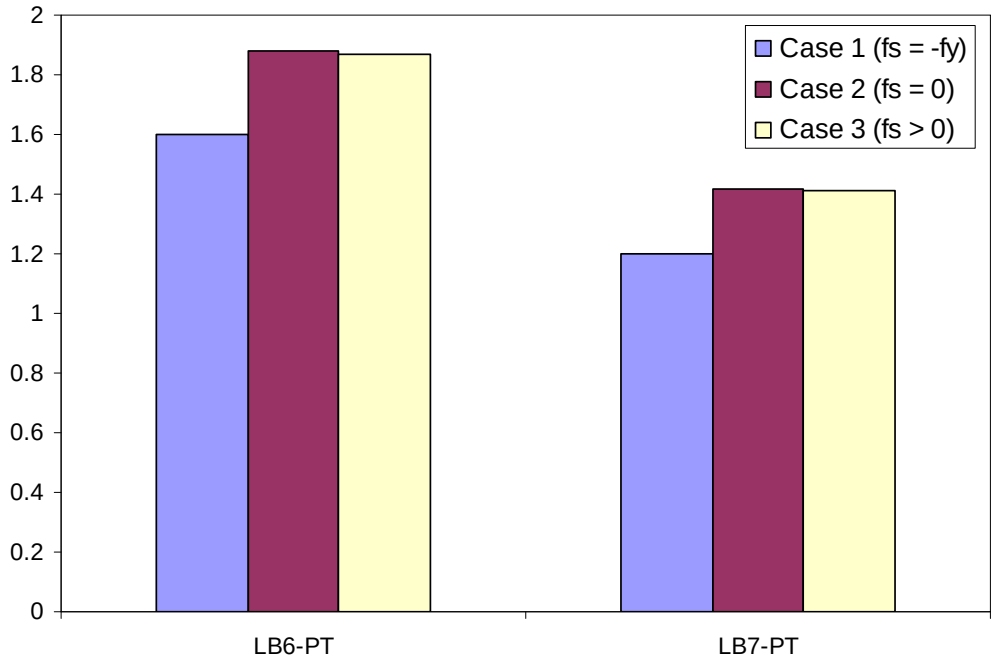

Figure 2-4. Nominal re-centering ratios for three cases of mild steel stresses.

2.3 Development of the Large-Bar Connection with Post-Tensioning

Various combinations of amounts of mild steel, prestress bars or strands, re-centering ratios, and axial loads were considered to investigate which ones would best fulfill the objectives of this research and be comparable with previously tested large-bar connection columns. The non-prestressed column from the previous study (LB8-D1) had a nominal re-centering ratio of 0.91, but its hysteresis implied no re-centering ability. Therefore, two columns were selected for this research, one with a re-centering ratio of 1.2 and another with a ratio of 1.6. The researchers also decided to design the post-tensioned bar to remain elastic up to at least 3 percent drift. This constraint imposed an upper bound on the permissible initial tension. Table 2-1 shows the main design parameters for the specimens. The choices were constrained by the availability of only discrete sizes of post-tensioning bars and the fact that the number of mild steel bars had to be an integer.

Table 2-1. Test Specimen Design Parameters.

	Key Parameters				Calculated Parameters		
Specimen	λ_{re}	A_p ($in.^2$)	A_s ($in.^2$)	$P_{col} + A_p f_{po}$ (kips)	f_{po} (ksi)	$M_{at\ 2\%\ drift}$ (M-C) (kip-in.)	$M_{at\ 2\%\ drift}$ (IAD) (kip-in.)
LB8-D1*	0.91	-	4.74	260	-	3428	3630
LB7-PT	1.2	1.58	3.60	240	88.1	3155	3370
LB6-PT	1.6	1.58	2.64	240	84.5	2813	3010

* Pang test specimen.

As shown in Table 2-1, the total initial axial load (gravity axial load plus initial post-tensioning force) was nearly constant. The main difference between the three specimens was the amount of mild steel, which ranged from 0.84 percent for LB6-PT to 1.51 percent for LB8-D1.

Two values are given for the moments at 2 percent drift in Table 2-1. The values in the left column were calculated by using a moment-curvature analysis (M-C), while those in the right column were obtained from an interaction diagram (IAD).

In the M-C analysis, the cross-section was divided into trapezoidal layers, and the stress was calculated for each layer. To calculate the stresses, the analysis used the following constitutive relationships in which tension was positive:

- Concrete in compression:

  For $0 > \varepsilon > -0.002$, a cubic equation with the following end conditions modeled the stresses:

  $$\sigma(0) = 0,$$

  $$\sigma'(0) = 4000, \text{ (Initial tangent stiffness)}$$

  $$\sigma(-0.002) = -6.5, \text{ (Concrete crushing strength)}$$

  $$\sigma'(-0.002) = 0,$$

  For $-0.06 < \varepsilon < -0.002$, a linear equation:

  $$\sigma(\varepsilon) = \frac{-6.5}{(-0.002 - (-0.06))}(\varepsilon - (-0.06)).$$

  And for $-0.06 > \varepsilon$:

  $$\sigma(\varepsilon) = 0.$$

- The concrete had no tensile strength.
- The mild steel assumed an elastic perfectly plastic relationship, with f_y = 60 ksi and E_s = 29000 ksi.
- The prestressed steel relationship was modeled by using a Menegotto-Pinto equation, with E_p = 28500/8 ksi, f_{py} = 120 ksi, f_{pu} = 150 ksi, e_{pu} = 0.05*8, and R = 7.

The program that implemented the analysis was written for a bonded prestress tendon, assuming strain compatibility between the steel and concrete. To obtain a reasonably good prediction of the moment for the unbonded post-tensioned bar, an equivalent elastic modulus of the unbonded prestress steel was defined as a multiple of the elastic modulus for the bonded prestress steel. For these calculations the following assumptions were made:

- The plastic hinge length of the column was assumed to be 3/4D, with D = column diameter.
- The neutral axis was assumed to be at the same location in both cases.

These assumptions led to the following equation:

$$E_{p,eq} = \frac{L_{ph}}{L_{pt}} \cdot E_p \qquad \textbf{2-5}$$

where

$E_{p,eq}$ = Equivalent elastic modulus of unbonded prestress steel

E_p = Elastic modulus of prestressed steel

L_{pt} = Length of the post-tension bar

L_{ph} = Length of the plastic hinge region.

$L_{pt} = 120$ in. and $D = 20$ in., so the elastic modulus becomes:

$$E_{p,eq} = \frac{1}{8} \cdot E_p$$

Embedded in these calculations was also the relationship between the drift ratio and the curvature of the column. The increase in strain in the post-tensioned bar due to increasing drifts was assumed to be:

$$\varepsilon = \frac{\delta}{L_{pt}} = \frac{\alpha \cdot D \cdot \vartheta}{L_{pt}} = \frac{\alpha \cdot D \cdot \varphi \cdot L_{ph}}{L_{pt}} \qquad \textbf{2-6}$$

where

$\delta =$ Length increase of the post-tension bar due to the strain increase

$\alpha \cdot D =$ Distance from the column center to the neutral axis

$\vartheta =$ Angle of rotation

$\varphi =$ Average curvature in the plastic hinge region.

The following also holds true, by virtue of similar triangles:

$$\frac{\Delta}{L_{col}} = \frac{\delta}{\alpha \cdot D} \qquad \textbf{2-7}$$

Combining equations 2-6 and 2-7 results in the following relationship, that was used to obtain the moment values presented in Table 2-1:

$$\varphi = \frac{\Delta}{L_{col} \cdot L_{ph}} \qquad \textbf{2-8}$$

The values in the right column of Table 2-1 were calculated by using an interaction diagram for the axial load and moment. The increase in axial load due to the unbonded post-tensioning was calculated by using elastic analysis, with the assumption that the column neutral axis was a distance of D/6 (D = column diameter) from the center of the column. This assumption allowed a strain, and thus a stress, in the post-tensioned bar to be calculated. The total load due to the post-tensioning and externally applied axial load could then be inserted into the columns interaction diagram to find the appropriate value for the moment.

Several changes were made to the cap-beam design to incorporate the post-tensioning bar, and these are described in Section 3.2, which discusses the construction of the specimens. As many elements as possible, such as column and cap-beam dimensions,

were left unchanged to facilitate construction and to allow for direct comparison. A schematic drawing of the system including post-tensioning is shown in Figure 2-5.

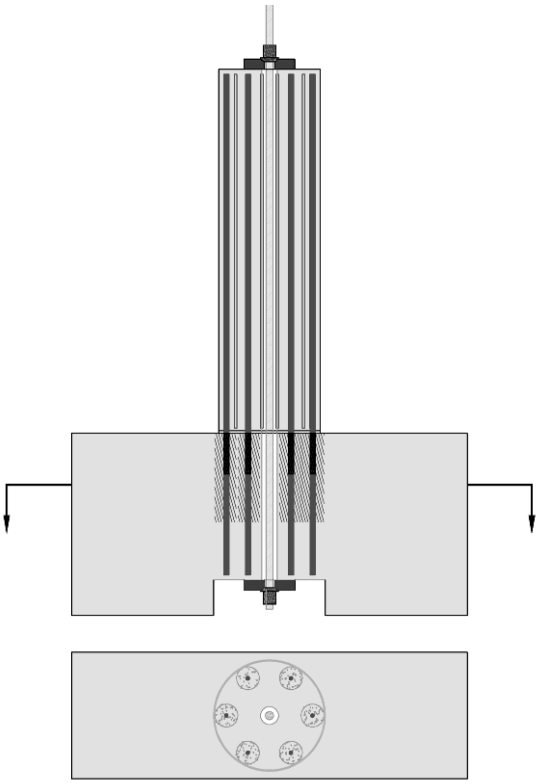

Figure 2-5. Post-tensioned specimen schematic.

2.4 Application of the Post-Tensioned Connection to Practice

For the scaled-down test specimens, one 1 3/8-in. post-tensioned bar was calculated to be sufficient to provide the needed restoring force. For the full-scale prototype, a different tendon arrangement would be necessary because no manufacturer makes a 4 1/8-in. diameter bar. Keeping the reinforcement ratio the same for the full-scale column would require using multiple post-tensioned bars, either two 2 ½-in. diameter bars or four 1 ¾-in. diameter bars. The need for multiple bars would complicate the anchorage of the bars. With one bar, a single bearing plate with a nut would be sufficient on each end, but using multiple bars would require a more complex system, and construction tolerances for the post-tensioned bar were fairly tight.

A solution to this problem would be to use strands instead of bars. Strands are commonly bundled together, and such anchorage systems are readily available. A key difference between strands and bars is their yield and ultimate strains. Strands typically have a nominal yield stress of about 240 ksi, whereas bars nominally yield at 120 ksi. A strand system could take advantage of the higher yield stress by using a higher initial stress and so reduce the total prestress area to obtain the same re-centering ability. Some possible configurations are shown in Table 2-2.

Table 2-2. Possible prestress configurations.

Scale	Bar/ Strand	Number of bars/strands	d_{ps} (in)	$A_{ps,tot}$ (in^2)	d_{duct} (in)
0.4	Bar	1	1 3/8	1.58	3
1.0	Bar	1	-*	9.88	7.5
1.0	Bar	2	2 1/2	10.38	7.5
1.0	Bar	4	1 3/4	10.40	7.5
1.0	Strand	24	0.6	5.21	7.5
1.0	Strand	24	0.6	5.21	7.5

*Idealized bar, if area of 1/38 in. bar is scaled up to full size.

The bars or strands would need to be anchored in both the foundation and the cap-beam or diaphragm. Figure 2-6 shows such a simple system. The bottom anchorage is cast in the foundation, and the top anchorage is located on top of the cap-beam. It is then cast in the diaphragm so both ends are embedded in concrete for corrosion protection.

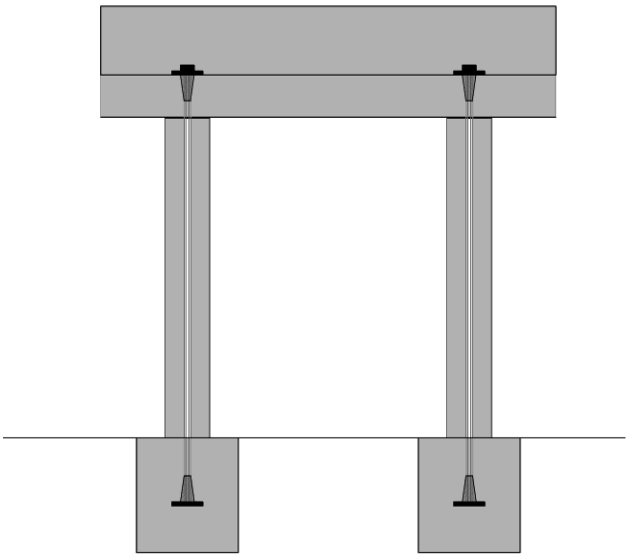

Figure 2-6. Re-centering bridge bent with prestressing strands.

CHAPTER 3: EXPERIMENTAL PROGRAM

3.1 Overview

Two columns with the large-bar, re-centering connection were tested to gather information about their re-centering abilities following an earthquake. The effects of earthquakes were simulated with a cyclic, displacement-controlled test. This chapter describes the specimen construction, test set-up, instrumentation, and data acquisition.

Table 3-1. Test Matrix

Specimen	Large-bar size	PT bar diameter	$P_{col}/(f'_c A_g)$	$P_{pt}/(f'_c A_g)$	λ_{re}
		in.	%	%	
LB8-D1*	#8	-	10	-	0.9
LB7-PT	#7	1 3/8	5	5	1.2
LB6-PT	#6	1/38	5	5	1.6

*Pang test specimen.

The main difference between the two specimens was that LB7-PT had six #7 vertical column bars, whereas LB6-PT had six #6 bars. Both specimens also had twelve #3 vertical bars and a 1 3/8-in. post-tensioned Williams bar (PT bar). The initial post-tensioning force differed slightly between the specimens. The bottom longitudinal bars in the cap-beam needed to be moved up 6 inches to accommodate a notch in the cap-beam that allowed for the placement of an anchor plate and a nut for the PT. Therefore, the total reinforcement area was increased for both the top and bottom bars by two bars for each section. The transverse hoop steel was also adjusted slightly.

The naming convention for the vertical column bars is shown in

Figure 3-1 and will be used to describe the bars and instrumentation locations.

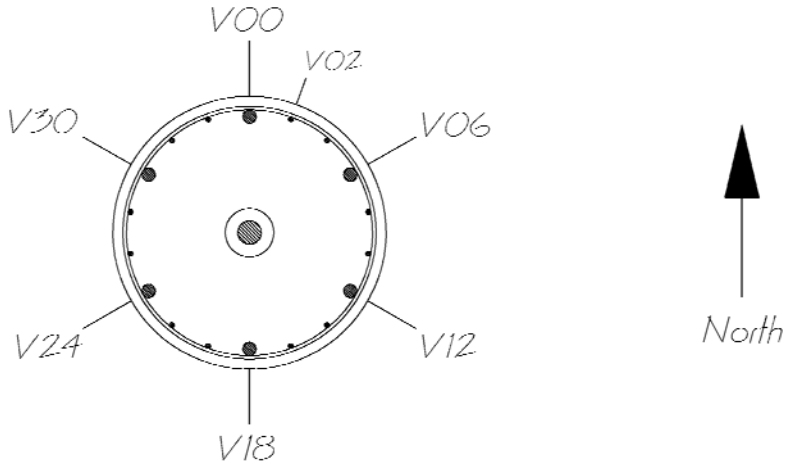

Figure 3-1. Column vertical bar naming convention.

3.2 Specimen Construction

3.2.1 Construction Overview

The two post-tensioned specimens tested in this study were similar to specimens tested by Pang (2008). The same construction methods were used where possible.

To facilitate the construction process in the laboratory the construction sequence differed from what it would be in the field. For example, the large column bars were first grouted into the ducts, then placed in the cap-beam form. Next the cap-beam was cast, and the column, with a grout pad between it and the cap-beam, was cast on top of the cap-beam a few weeks later. This process is described in sections 3.2.2 and 3.2.3.

3.2.2 Cap-Beam and Vertical Bar Construction

The cap-beam dimensions were the same as that in the previous study, 36 in. high, 78 in. long and 25 in. wide. First the cap-beam rebar cage was constructed and strain gauged. Next the large column vertical bars were strain gauged and debonded over 8 in. from the interface down into the cap-beam. The debonding method (method D1 in Pang 2008) used a PVC pipe cut in half length-wise and fitted tightly around the bar. The seams and ends of the PVC pipe were then taped tight with duct tape, and all openings were caulked to prevent any concrete from entering. Then the bars were grouted into corrugated metal ducts. The ducts were 4 in. in diameter and 17.5 in. long. A device had been constructed for the purpose of keeping the ducts at the right height relative to the

bars and the bars in the center of the ducts. The grout used was Dayton Superior Sure Grip High Performance Grout. For each batch of grout, grout test cubes were made to measure the strength of the grout.

Formwork from the previous study was reused. In addition, a box of dimensions 6 in. x 22 in. x 25 in. was constructed out of 2x4s and plywood and screwed to the bottom of the formwork. This provided a notch in the cap-beam, shown in Figure 2-5, to allow for a bearing plate and spherical nut for anchoring the post-tension bar. Once the formwork had been assembled, the cap-beam cage was put in, and the grouted vertical bars were set in place. The post-tensioned duct was cut into two pieces, one placed in the cap-beam and the other in the column. Four 2-in. diameter PVC pipes were placed in the cap-beam to provide an opening for the 1 ¼ post-tensioned bars that anchored the specimen down to the test rig. The test setup is described in more detail in Section 3.3.

The column vertical bars, the post-tensioning duct, and the PVC pipes were all braced and the cap-beam was cast. The vertical bar ducts and the debonded length were designed to extend from the interface down into the cap-beam, as was done in the previous study, but during construction the tops of many of the ducts ended about 1 inch below the surface, as can be seen in Figure 3-2.

Figure 3-2. Specimen LB7-PT cap-beam after casting.

3.2.3 Column and Loading Ring Construction

To simulate construction in the field, a grout pad was poured at the column-to-cap beam interface. Then the post-tensioned bar duct was ground flush with the grout pad. To connect the two pieces of post-tensioned bar duct, a plastic pipe of the same diameter as the duct and 6 in. long was sliced longitudinally, and small slices were cut off until it fit tightly inside the duct. Half of the plastic piece went inside the cap-beam duct and half of it stood up above it. The edges were then caulked. The column duct was fit over the upper half of the plastic pipe, and the space between the two duct pieces was caulked to prevent any concrete from entering into the duct. Next the column spiral was tied to the vertical bars, and then the #3 column bars were tied onto the spiral.

The concrete form used for the column was a Sonotube. It was cut to the length needed, and about 1-in. diameter holes were cut in it to accommodate instrumentation. The Sonotube was then placed over the tied column and over the grout pad on the bottom and attached to the beam formwork to prevent the tube from uplifting during casting of the columns. Concrete spacers were positioned in several places on top to keep the column cage in place, and formwork was added on top to fasten the post-tensioned duct in the center of the column. The rods used to measure rotation of the column were inserted through the lower holes, and strain gauge wires were collected together and threaded out of a hole cut in the Sonotube about half way up the column. The curvature rods were assembled with methods developed in previous studies (see Pang 2008).

An axial-loading ring was constructed in parallel with the column. The loading ring was used to transfer axial load from the Baldwin testing machine to the column. It is shown in figures 3-3 and 3-4.

Figure 3-3. Loading ring above specimen.

Figure 3-4. Close up of loading ring

The loading ring was needed because the PT bar and its load-cell extended up through the top of the column, as can be seen in Figure 2-5, so the Baldwin head could not sit on top of the column. The loading ring was a 20-in. long and 20-in. wide concrete cylinder with a 12-in. diameter hole in the center. The cylinder also had a ¼-in. thick steel tube around its perimeter and a 22-in. x 22-in. x 2-in. steel plate on top, welded to the tube. The steel and a 12-in. diameter Sonotube were used as formwork for casting. The concrete was reinforced with ten #5 bars that were held in place with tied spiral and welded to the steel plate. Four tabs were welded onto the bottom edge of the steel tube to guide the loading ring onto the top of the column. A 1-in. diameter hole was cut in the steel tube and the Sonotube on the inside at about mid height, and a greased PVC pipe was placed through the tube wall to provide a path for the load-cell wire. The column and loading ring were cast.

3.2.4 Post-Tensioning Installation and Stressing

Once the column and loading ring had been cast and the concrete had reached the strength needed, the formwork was removed. Next the top and bottom bearing plates were hydro-stoned in place, and the PT bar was inserted into the duct. The bottom plate

was a dished 8-in. x 8-in. x 1 ½-in. steel plate onto which a spherical, greased nut was threaded and hand-tightened. The top plate was an 8-in. x 8-in. x 1-in. steel plate onto which a hexagonal nut was temporarily threaded and tightened.

The PT bar was stressed from the top of the column, as shown in Figure 3-5. Wood blocks were placed under the bottom end of the PT bar to keep it in place, and the top nut was removed to allow the load-cell to be placed over the bar. A dished plate was placed on top of the load-cell, and a greased spherical nut was hand tightened against that. The load-cell was connected to the data acquisition system prior to stressing to monitor the load.

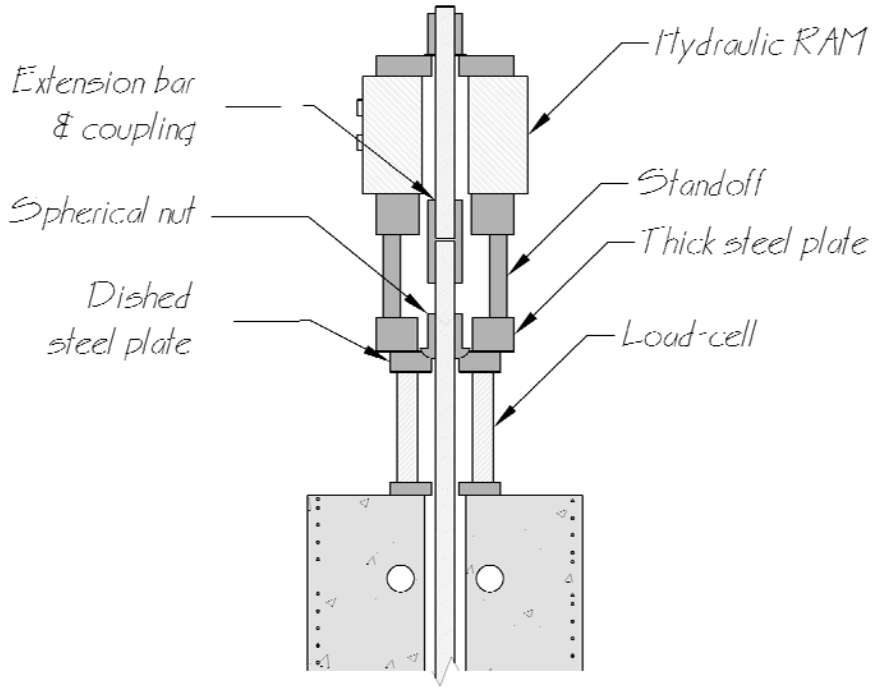

Figure 3-5. Section through the PT bar stressing setup.

The initial stressing set-up differed from the final stressing set-up shown in Figure 3-5, as it had no thick plate under the standoff. This initial set-up proved to be deficient, as the dished plate seemed to deform under the stressing, and so its central hole deformed. As a result, the nut would not move and could not be tightened. To distribute the force more evenly, a steel plate of dimensions 10 in. x 10 in. x 3 in. with a 4-in. diameter hole was placed on top of the dished plate during stressing.

The standoff sat on top of the thick steel plate and provided access to the spherical nut. The hydraulic jack had a capacity of 300 kips and consisted of a double acting ram connected by two hoses to an electric pump. A Williams 150-ksi high-strength extension bar with a coupling was threaded on to the end of the PT bar and extended up through the standoff and pump with enough extra length for a plate and nut on top.

A plate was then placed on top of the ram, and a nut was threaded tightly on to it. Next the pump was turned on, and the PT bar was tensioned to a stress of about 7.5 percent higher than the target stress for testing because some loss in the prestress force before testing day was expected. The spherical nut was tightened, and the pressure in the pump was released.

The prestressing force lost in the next few days was larger than expected, so the researchers had to re-stress the bar. After stressing, the bar force measured by the load-cell on top of the column was monitored periodically. Figure 3-6 shows the loss of prestress force plotted against time from initial stressing, for both the initial stressing and re-stressing of the bar for both specimens.

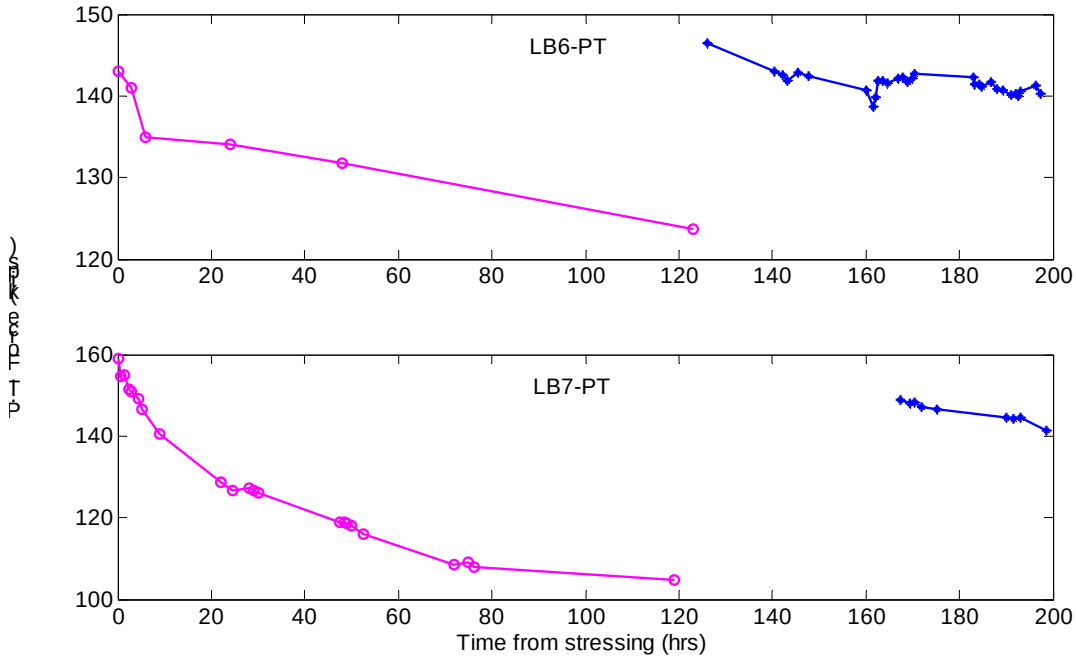

Figure 3-6. Prestress force in post-tensioned bar over time, from initial stressing.

Table 3-2 provides the target prestress force for testing and the actual prestress force on test day, $P_{pt,o}$. The force in Specimen LB6-PT on test day was slightly higher than the target value, but it could not be reduced because the PT bar was no longer accessible.

After the PT bar had been stressed, the loading ring was leveled and hydro-stoned to the top of the column. The specimen was painted white, so that cracks could be identified more easily during the test. A grid was drawn on the lower half of the column and on the top of the base so that the cracks could be located precisely.

Table 3-2. Target and actual prestress force at the beginning of the test.

Specimen	Target $P_{pt,o}$ (kips)	$P_{pt,o}$ (Test Day) (kips)
LB6-PT	133.5	140.3
LB7-PT	139.0	141.3

3.3 Test Set-up

The test specimen was placed in the test rig on top of a concrete anchor block, as shown in Figure 3-7. It was connected to the anchor block by a pad of hydro-stone at each end of the beam to simulate the end conditions on site. It was then post-tensioned down to the anchor block with four 1 ¼-in., Williams 150-ksi, all-thread bars. These passed through PVC pipes cast into the beam and into threads embedded in the anchor block. The bars prevented uplift of the beam during the testing. The anchor block was in turn fastened to the laboratory floor.

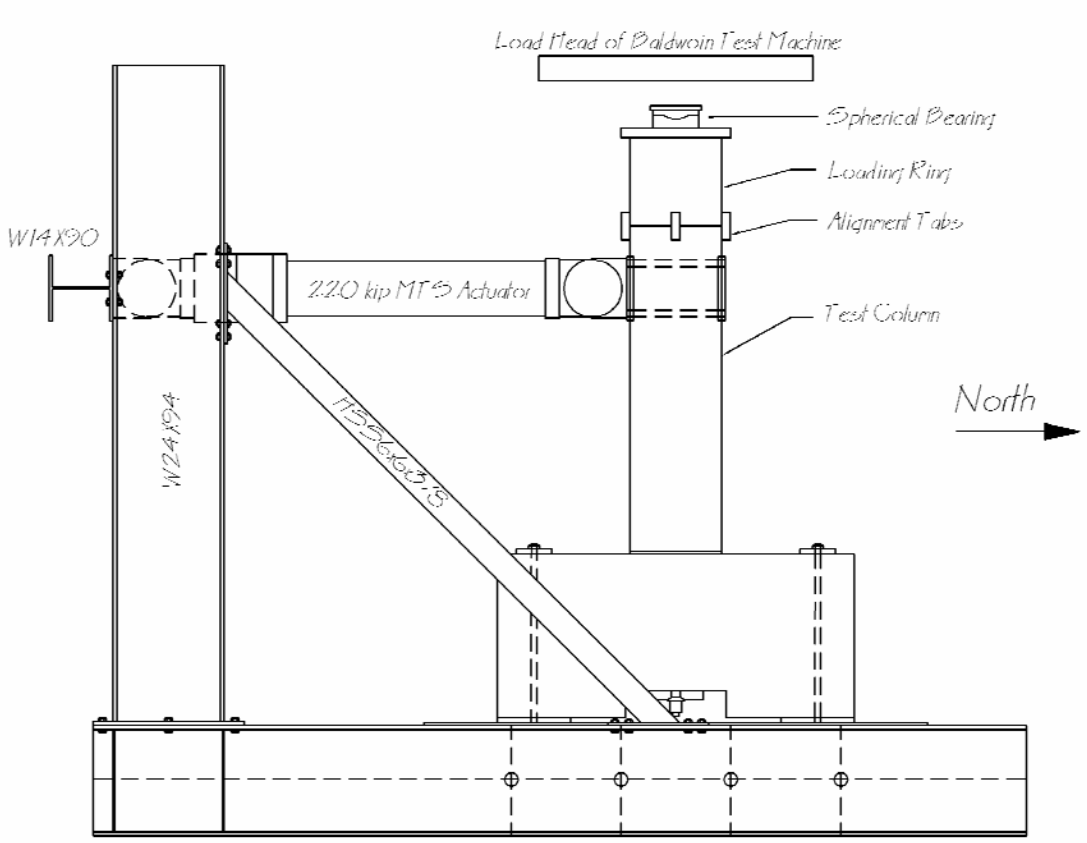

Figure 3-7. Specimen test set-up.

The axial load was applied to the column by a 2.4-million lbs. Baldwin Universal Testing Machine. A channel attached to the loading head of the machine served as a track along which the specimen moved and prevented out-of-plane movement. To minimize the friction between the stationary Baldwin and the moving specimen, sheets of stainless steel were attached underneath and to the sides of the channel, and greased pieces of polytetrafluoroethylene (PTFE) were attached to a steel plate on the specimen side. The steel plate to which the PTFE was attached rested on a spherical bearing that transferred the axial load from the Baldwin to the test specimen. The bearing rested on top of the loading ring described in section 3.2.3. It was placed inside four tabs, with dimensions of about ½ in. x 2 in. x ½ in., and welded onto the top of the loading ring to prevent the bearing from sliding off the column in the unlikely event of the friction proving insufficient.

The lateral load was applied by a horizontal 220-kip, servo-controlled actuator that was attached to the self-reacting, steel braced frame.

3.4 Displacement History

The same displacement history was applied to these specimens that was used in the previous study on the large-bar configuration. It was controlled by a linear variable differential transformer (LVDT) inside the actuator. Because of flexibility in the steel beam to which the actuator was attached, the actual column displacement was somewhat less than the input displacement. This difference was most noticeable during the smaller cycles when the column was essentially elastic. The displacement history is shown in Figure 3-8, and target peak displacements for each cycle are reported in Table 3.3.

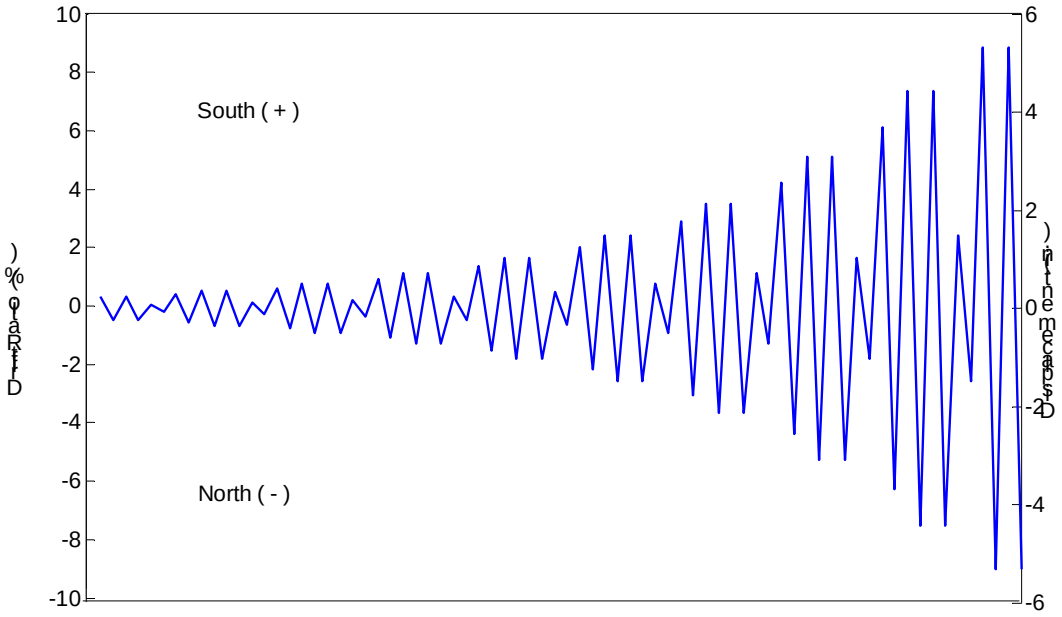

Figure 3-8. Target displacement history.

The target history is a modification of the loading history for precast structural walls recommended in Chapter 9.6 of NEHRP (Building Seismic Safety Council). The load was applied in sets of four cycles of amplitude: 0.33A, 1.2A, 1.4A, and 1.4A, where A was the amplitude of the final cycle of the previous set. The small cycle was intended

to supply information about the specimen stiffness. Through the test, the actuator moved from zero to the peak displacement in 20 seconds.

Table 3-3. Target displacement history.

Cycle	Drift Ratio (%)	Disp. (in)	Cycle	Drift Ratio (%)	Disp. (in)
1	±0.40	±0.240	20	±2.06	±1.238
2	±0.40	±0.240	21	±2.48	±1.486
3	±0.13	±0.080	22	±2.48	±1.486
4	±0.48	±0.288	23	±0.83	±0.495
5	±0.58	±0.346	24	±2.97	±1.783
6	±0.58	±0.346	25	±3.57	±2.140
7	±0.19	±0.115	26	±3.57	±2.140
8	±0.69	±0.415	27	±1.19	±0.713
9	±0.83	±0.498	28	±4.28	±2.568
10	±0.83	±0.498	29	±5.14	±3.081
11	±0.28	±0.166	30	±5.14	±3.081
12	±1.00	±0.597	31	±1.71	±1.027
13	±1.19	±0.717	32	±6.16	±3.698
14	±1.19	±0.717	33	±7.40	±4.437
15	±0.40	±0.239	34	±7.40	±4.437
16	±1.43	±0.860	35	±2.47	±1.479
17	±1.72	±1.032	36	±8.87	±5.325
18	±1.72	±1.032	37	±10.65	±6.39
19	±0.57	±0.344	38	±10.65	±6.39

3.5 Instrumentation

3.5.1 Load Cells

A 220-kip load-cell, located in the actuator, measured the applied horizontal loads during the test.

A second load-cell was placed over the post-tensioned bar to measure the force in the bar. It sat on top of an 8-in. x 8-in. x 1-in. steel plate that was hydro-stoned to the top of the column. The plate had a hole in the center through which the post-tensioned bar went. On top of the load-cell was a dished 8-in. x 8-in. x 1 ½-in. steel plate that was tightened down with a spherical nut. The load cell was connected before the bar was stressed to monitor the losses before testing, as well as the total load in the bar during the test (Figure 3.9).

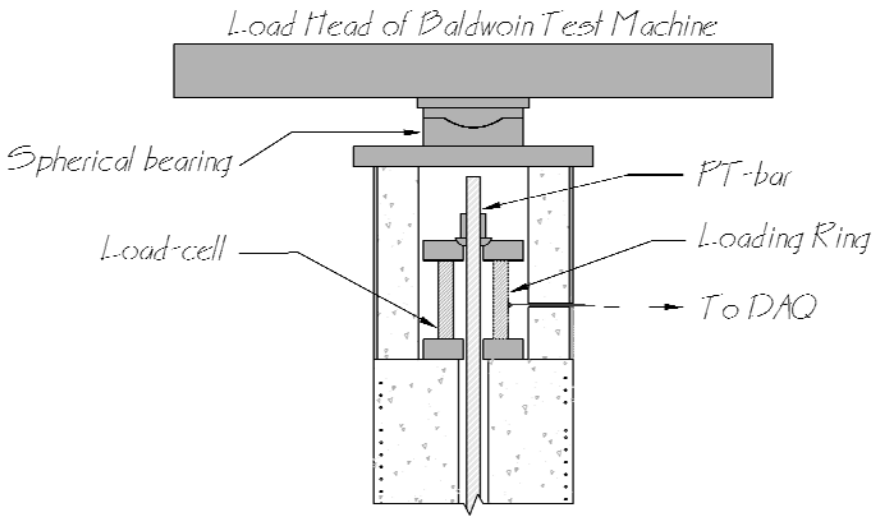

Figure 3-9. Post-tensioned bar load-cell set-up.

3.5.2 Linear Potentiometers

A total of 25 potentiometers (pots) were used to measure and monitor the behavior of the specimen and test set-up. They are shown in Figure 3-10.

Eight potentiometers (numbered 1 through 8) were used to measure the column rotation. They were attached to the rods cast in the column at nominal distances of 1.75, 6.5, 11.75, and 21.5 inches above the base. These relative rotations were subsequently converted to average curvatures.

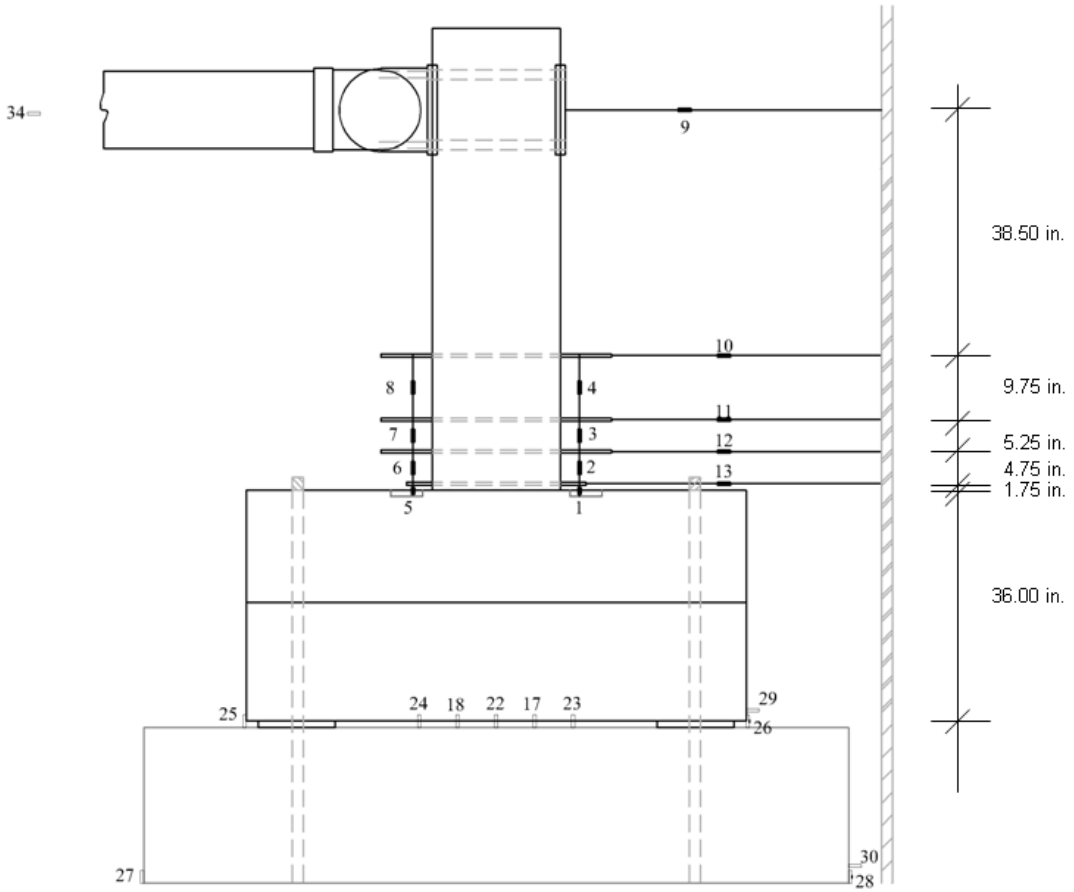

Figure 3-10. Locations of potentiometers.

Five string potentiometers (numbered 9 through 13) were used to measure the horizontal displacement of the column at the locations of the curvature rods and at the location of the applied lateral load.

Five potentiometers (numbered 17 through 18, and 22 through 24) were attached to the bottom of the east side of the base; they measured the vertical displacements, at the center, as well as 6 and 12 in. from center in both the north and south directions.

One cylinder potentiometer (numbered 34) measured the deflection of the reaction beam to which the actuator was connected. The remaining potentiometers (numbered 25 through 30) measured slip and uplift of the specimen and anchor block.

3.5.3 Strain Gages

A total of 25 strain gauges from Texas Measurements were placed on the mild steel rebar to measure strains. Figure 3-11 shows the locations of the strain gauges.

Because of a long shipping time for the strain gauges, the gauges that needed to be placed before casting of the cap-beam were acquired from previous projects' overstock so as not to delay construction. The gauge types and locations are listed in Table 3-4.

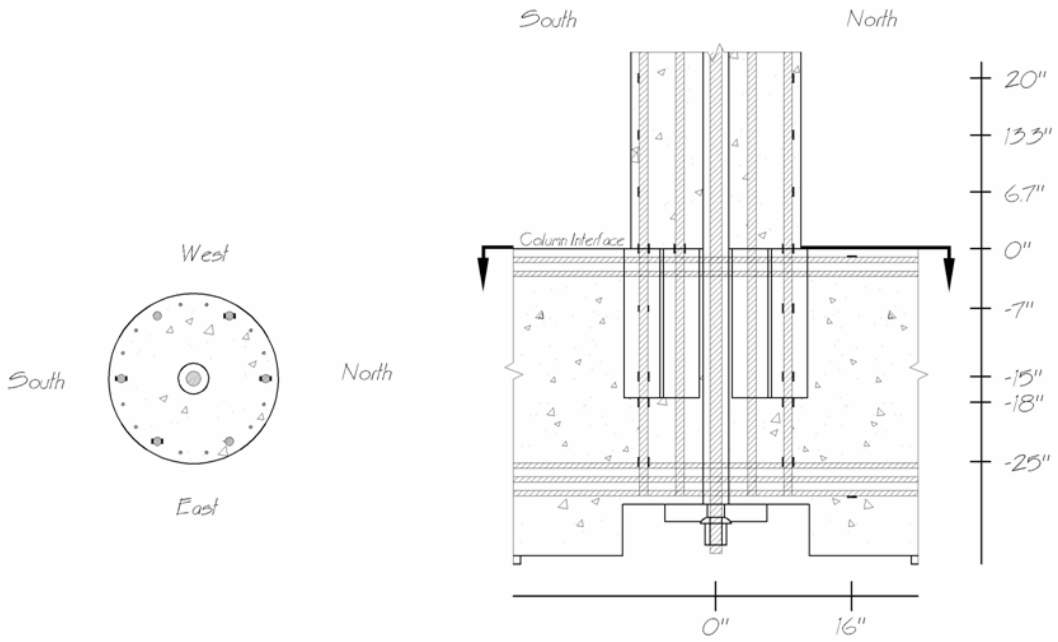

(a) Column Cross Section Showing Interface Gauges

(b) Location of V00, V12, V18 and Cap-Beam Longitudinal Bar Strain Gauges

Figure 3-11. Locations of specimen strain gauges.

Table 3-4. Strain gauge types used in the specimens.

Location	Quantity	LB6-PT	LB7-PT
Vertical "column" bars, below interface (in cap beam)	24	FLA-5-11-5L YFLA-5-11-5L	FLA-5-11-5L YEFLA-5-5L
Vertical column bars, above interface	9	FLA-5-11-5L	FLA-5-11-5L
Top and bottom cap-beam reinforcement	2	FLA-5-11-5L	YFLA-5-3L

The north (V00) and south (V18) bars experienced the largest displacements during testing and were the most heavily gauged. On each of these main bars, three gauges were located in the column at 1/3-, 2/3- and 1-column diameter up from the interface on the outside face of the bar. At the interface, as well as at 7, 15, 18, and 25 in. down in the cap beam, the bars had gauges on both sides.

Bars V12 and V30 also had gauges on both sides, but at the interface only. Bars V06 and V24 had no gauges.

One #3 bar (V02) had gauges up the column at the same heights as V00 and V18. Lastly, two gauges were placed on the longitudinal bars in the cap beam, one on the top of one of the top bars and the other on the bottom of a bottom bar.

The strain gauges were fastened with a CN strain gauge adhesive on a patch of rebar that had been ground flat, smoothed, and cleaned (see Figure 3-12). A small patch of gauge installation tape was placed over the gauge, and it was then coated for protection with M-Coat D, a type of moisture barrier from Vishay Micro-Measurements. To further protect the gauges, a layer of electrical tape was wrapped around the M-Coated area, and the lead wire was zip-tied to the bar. The gauge wire was then looped over the taped area with a layer of reversed electrical tape to allow the wire to move during the test without ripping (see Figure 3-13). One layer of low voltage rubber tape from Plymouth Rubber co. was then wrapped over everything.

Figure 3-12. Strain gauge after gluing (Picture courtesy of Jason Pang).

Figure 3-13. Two gauges at different stages of protecting (Picture courtesy of Jason Pang).

3.6 Data Acquisition and Documentation

The test data were recorded with the data acquisition system LabVIEW (Laboratory Virtual Instrument Engineering Workbench) from National Instruments. The sampling rate was 0.20 seconds. The recording was stopped at most cycle peaks to allow for pictures, damage observations, and crack mapping. Recording was also sometimes stopped at zero displacements for observation and pictures.

Four digital cameras were set up around the specimen. Pictures were taken at the peak displacements and zeros of each cycle. Two video cameras were used to record the latter half of the test. The locations of the digital cameras and video cameras are shown in Figure 3-14.

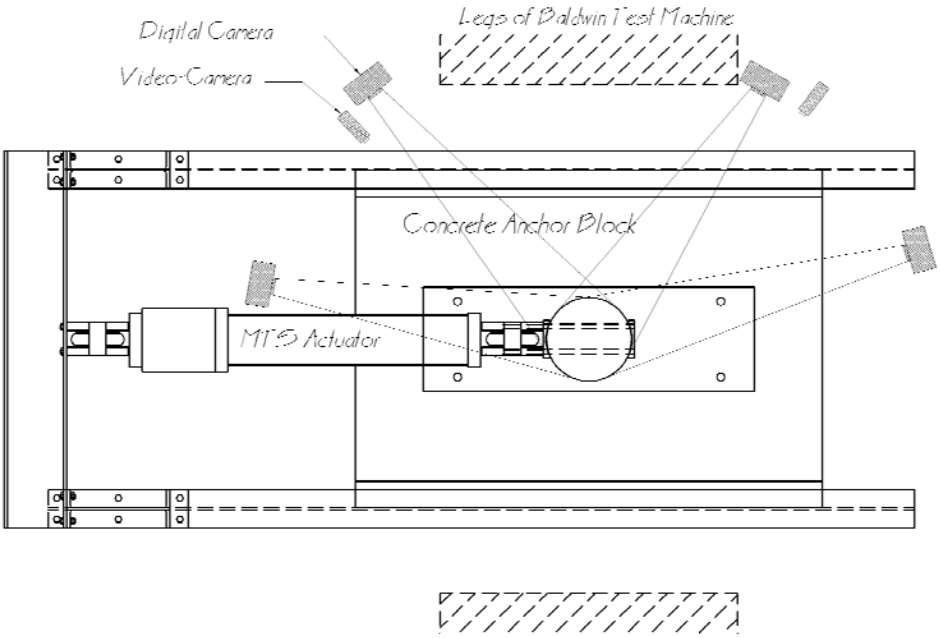

Figure 3-14. Locations of cameras (plan view).

CHAPTER 4: DAMAGE PROGRESSION

4.1 Definitions of Damage States

To evaluate the progression of damage throughout the test and to allow for comparison among specimens, the following terms, established for the UW/PEER Structural Performance Database (Berry et al. 2003a), were used to define key damage states.

Table 4-1. Key damage types.

Damage Type	Definition
First "significant" horizontal crack	Crack width ≥ 0.5 mm
First "significant" diagonal crack	Diagonal crack extends over ¼ of cross section depth. Crack width $\geq$ 0.5 mm
First residual open crack after unloading	Crack width $\geq$ 0.25 mm
First yield of longitudinal reinforcement	Strain gauge reading reaches yield strain at any location
First spiral yield	Strain gauge reading reaches yield strain at any location
Onset of crushing	Observed flaking, minor spalling
"Significant" spalling	Spall height $\geq$ 1/10 of column diameter.
Fully spalled	Spall height no longer increases with increasing deformation
Longitudinal steel exposed	First observation of vertical steel
First sign of longitudinal bar buckling	Visual observation
Large cracks within concrete core	Crack width $\geq$ 2.0 mm within core
Spiral fracture	Observation, sound
Longitudinal-bar fracture	Observation, sound
Loss of axial-load capacity	Instability of member

The yield strain used to determine the yielding of the longitudinal reinforcing bars was the yield strain measured from tension tests conducted on test bars for each bar size. A summary of the material test results can be found in Section 5.1.3. The complete stress-strain curves are shown in Appendix B.

$$\varepsilon_y = \sigma_y / E \text{, with } E = 29{,}000ksi$$

In the following sections, the first occurrences of the key damage states listed in Table 4-1 are identified for each specimen. Each corresponding table provides the cycle

number in which each damage state first occurred, as well as the peak drift ratios that the specimen had experienced to that point in the test.

4.2 Specimen LB7-PT

Specimen LB7-PT had six #7 bars that crossed the column-to-beam interface, and it had a prestress force of 141.3 kips at the start of testing. The specimen underwent a total of 37 displacement cycles, as shown in Figure 3-8. The first occurrences of key damage states for LB7-PT are listed in Table 4-2 and are plotted in Figure 4-1.

Table 4-2. Specimen LB7-PT key damage states.

Damage Type	Cycle	Drift Ratio (%)	Comments
First "significant" horizontal crack	12	0.53/-0.58	Crack widths: 0.5-0.75 mm. This was the first time that crack widths were measured.
First "significant" diagonal crack	16	-1.43	
First residual open crack after unloading	21	1.80/-1.84	Residual crack widths: 0.17-0.25 mm (interface)
First yield of longitudinal reinforcement	12	0.41	Strain gauge V00-00S yielded during a cycle to a drift ratio of 0.53%
First spiral yield	NA	NA	NA
Onset of crushing	20	1.41 / -1.46	Onset of spalling observed on North side of column
"Significant" spalling	25	2.82 / -2.86	
Fully spalled	37	10.07 / -9.55	
Longitudinal steel exposed	28	3.51 / -3.52	Bar V18 exposed
First sign of longitudinal bar buckling	30	4.45	Bar V18 showing signs of buckling
Large cracks within concrete core	-	-	Not observed
Spiral fracture	32	-5.32	Spiral on South side was necked at peak displacement and fractured upon unloading
Longitudinal-bar fracture	35	6.74	Bar V00 fractured at 1.04% on a small cycle with a peak drift ratio of 2.11%
Loss of axial-load capacity	NA	NA	Not observed

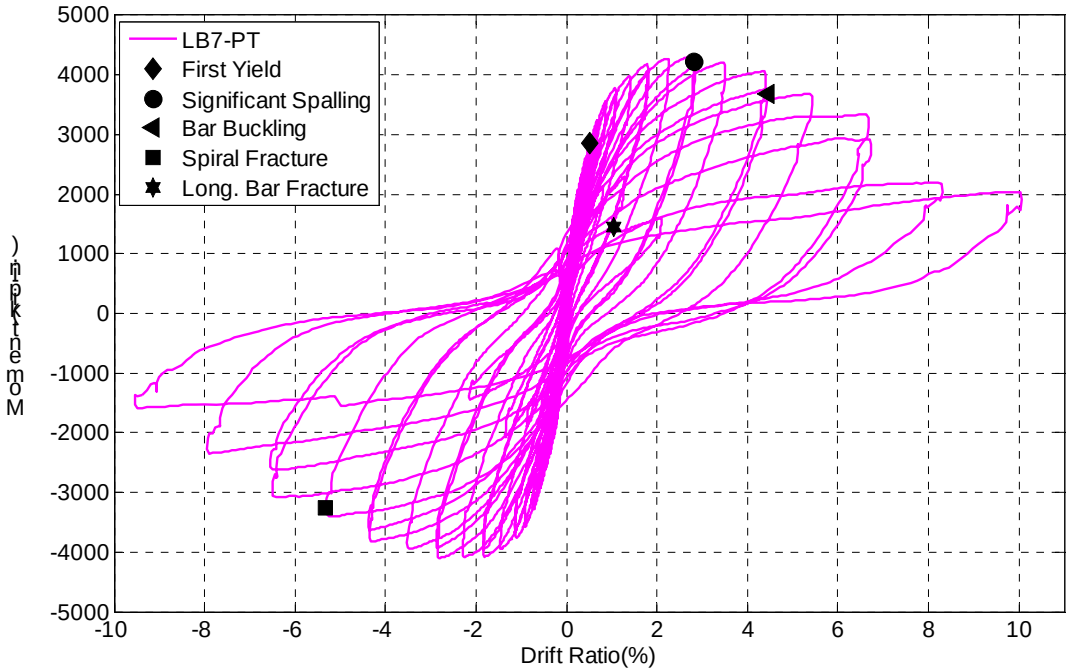

Figure 4-1. LB7-PT: moment vs. drift ratio with major damage states marked.

The test was not stopped to look for cracks for the first four test cycles. Cracks were first observed after Cycle 5, which had maximum/minimum drift ratios of 0.25 percent/-0.29 percent, respectively (Figure 4-2). Residual (zero displacement) cracks were first visible after Cycle 13 (0.68 percent/-0.72 percent).

The longitudinal column bars yielded first at 0.41 percent drift during Cycle 12. The first gauge to measure the yield strain (ε_y = 0.00222) was V00+00S (interface gauge on the south side of Bar V00). This was on the positive drift excursion of Cycle 12 (0.53 percent). The interface gauge on the north side of Bar V00 (V00+00N) yielded shortly after that, on the same cycle. The interface gauge on the south side of Bar V18 also yielded on Cycle 12, close to the peak negative drift.

The onset of column crushing (Figure 4-3) was first noticed on the north side of the column at Cycle 20, which had a positive peak drift ratio of 1.41 percent, and at the next cycle, with 1.80 percent drift ratio, for the south side. Over the next few cycles, the flaking and spalling increased (figures 4-4 and 4-5). At Cycle 28 (3.51 percent/-3.52 percent) the cover had spalled off on both sides of the column, exposing the spiral and Bar V18. Kinks in the spiral were not visible until a few cycles later, during a small cycle (Cycle 31) with peak drift ratios of 1.28 percent/-1.35 percent.

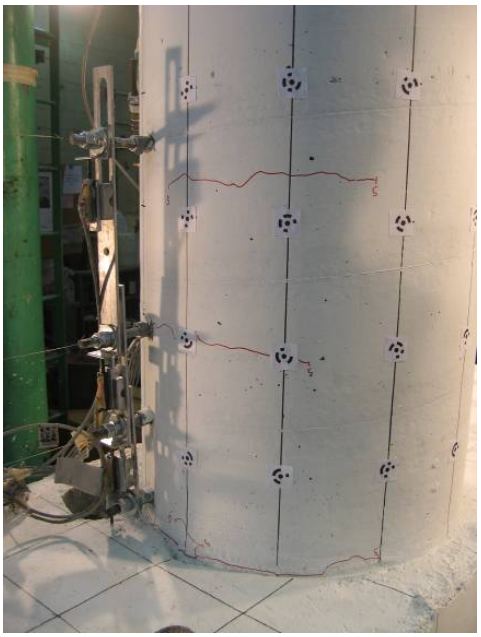

Figure 4-2. LB7-PT: column flexural cracks, Cycle 5 (0.25%).

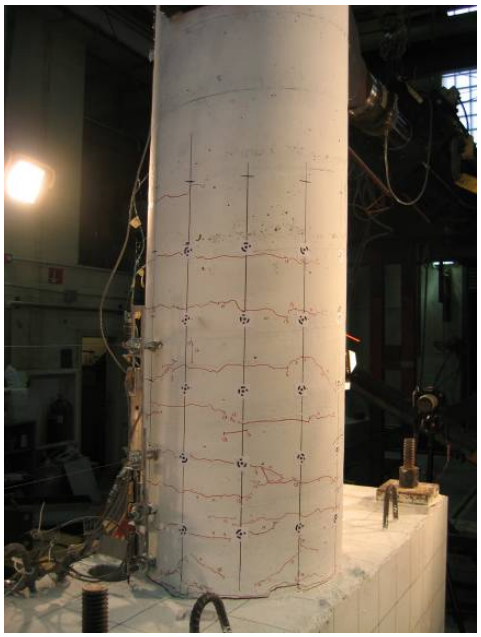

Figure 4-3. LB7-PT: onset of crushing, Cycle 20 (1.41%).

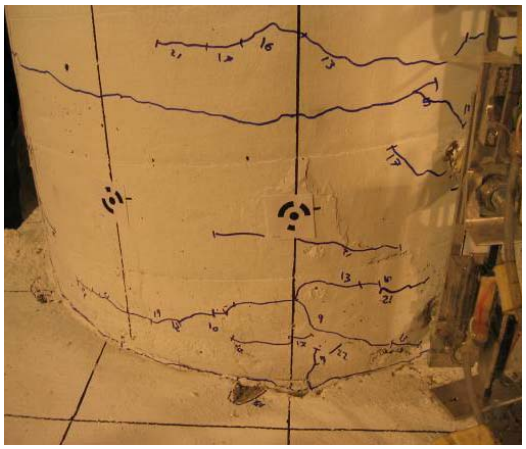

Figure 4-4. LB7-PT: south side, onset of column crushing. Cycle 22 (-1.85%).

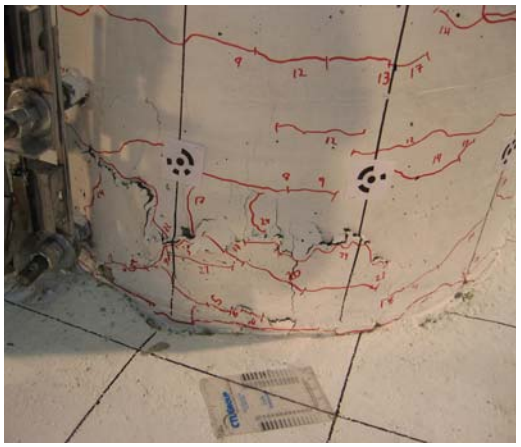

Figure 4-5. LB7-PT: north side, Cycle 24 (2.26%).

Buckling of Bar V18 was first observed during Cycle 30. On Cycle 32 (5.43 percent/-5.32 percent) buckling of Bar V18 had increased (Figure 4-6), and the first turn of the spiral around that bar was starting to neck. It then fractured during the load reversal

(Figure 4-7). Bar V00 had also buckled on the peak negative drift of this cycle. At Cycle 33 (6.6 percent/-6.5 percent), the second turn of the spiral around Bar V18 fractured, and on unloading of this cycle in the other direction, the third turn also fractured.

Longitudinal Bar V00 fractured two cycles later (Figure 4-8) in a small cycle with a maximum drift ratio of 2.11 percent after undergoing peak drifts of 6.74 percent/-6.56 percent in the previous cycle. The specimen was cycled until Bar V18 fractured at Cycle 37 (10.07 percent/ -9.55 percent) (Figure 4-9). The fracture of Bar V18 occurred about ½ in. below the interface, where the debonded region of the bar started. A partial fracture on the inward facing side of the bar, about 6 in. up from the interface, was also observed; this was in the upper region of the bulging caused by the buckling.

Figure 4-6. LB7-PT: Bar V18 buckling and spiral necking, Cycle 32 (5.43%).

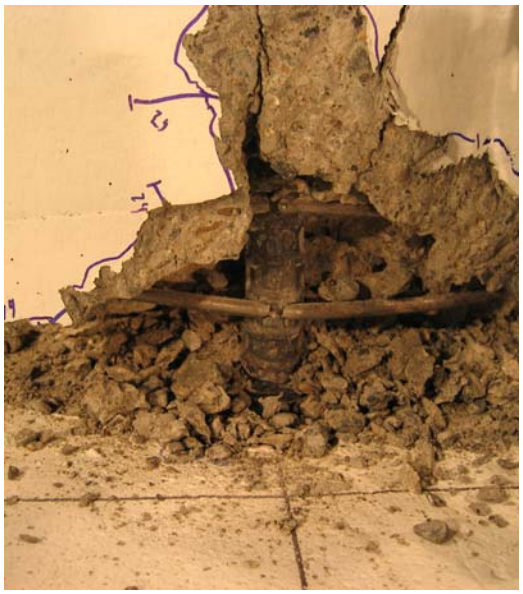

Figure 4-7. LB7-PT: spiral fracture, Cycle 32 (-5.32%).

Figure 4-8. LB7-PT: Bar V00 fracture, Cycle 35 (2.11%).

Figure 4-9. LB7-PT: Bar V18, Cycle 37 (-9.55%).

4.3 Specimen LB6-PT

Specimen LB6-PT had six #6 bars that crossed the column-to-beam interface, and it had a prestress force of 140.3 kips at the start of testing. This specimen underwent 34 displacement cycles, as shown in Figure 3-8. Key damage states are listed in Table 4-3 and superimposed on the force-displacement curves in Figure 4-10.

During curing of LB6-PT, shrinkage cracks formed in the cap beam because it was located directly under the Structures Lab heater. These cracks were marked before testing was started. As was the case for LB7-PT, the first four test cycles for LB6-PT had no stops. At peak drift ratios of 0.26 percent/-0.30 percent, for Cycle 5, two small interface cracks, about 2 in. long, formed on the north side. Over the next few cycles, new interface cracks formed and elongated, but no cracks formed in the column. Not until Cycle 9 (0.42 percent/-0.47 percent) did cracks start to form in the column, on the south side (Figure 4-11). These first cracks were very small; they did not crack the paint but rather seemed to “stretch” it. It is possible this could have been due to the type of paint used and the temperature difference during and after painting. For LB6-PT, an interior latex paint was used instead of the primer used on LB7-PT. Residual cracks were first measured after Cycle 21 (1.81 percent/-1.90 percent).

Table 4-3. Specimen LB6-PT key damages states.

Damage Type	Cycle	Drift Ratio %	Comments
First "significant" horizontal crack	17	1.09/-1.18	First measurement of interface crack (1.75 mm, both sides)
First "significant" diagonal crack	24	4.17	Drift Ratio of 4.95% input by mistake for Cycle 24. Target Drift Ratio was 2.97%
First residual open crack after unloading	21	1.81/-1.90	Crack-width at zero: 0.3-0.4 mm
First yield of longitudinal reinforcement	12	-0.58	V18+00S yielded during cycle 12 to a drift ratio of -0.60%
First spiral yield	NA	NA	NA
Onset of crushing	22	1.81/-1.85	Onset of spalling observed on North side of column
"Significant" spalling	25	2.95/-2.94	
Fully spalled	32	-5.38	
Longitudinal steel exposed	24	4.17	Drift Ratio of 4.95% input by mistake for Cycle 24. Target Drift Ratio was 2.97%
First sign of longitudinal bar buckling	29	-4.32	Bar V00 buckled
Large cracks within concrete core	-	-	Not observed
Spiral fracture	32	-5.38	3 turns on North-side fractured
Longitudinal-bar fracture	33	6.75	Bar V00 fractured at 3.69% drift
Loss of axial-load capacity	NA	NA	Not observed

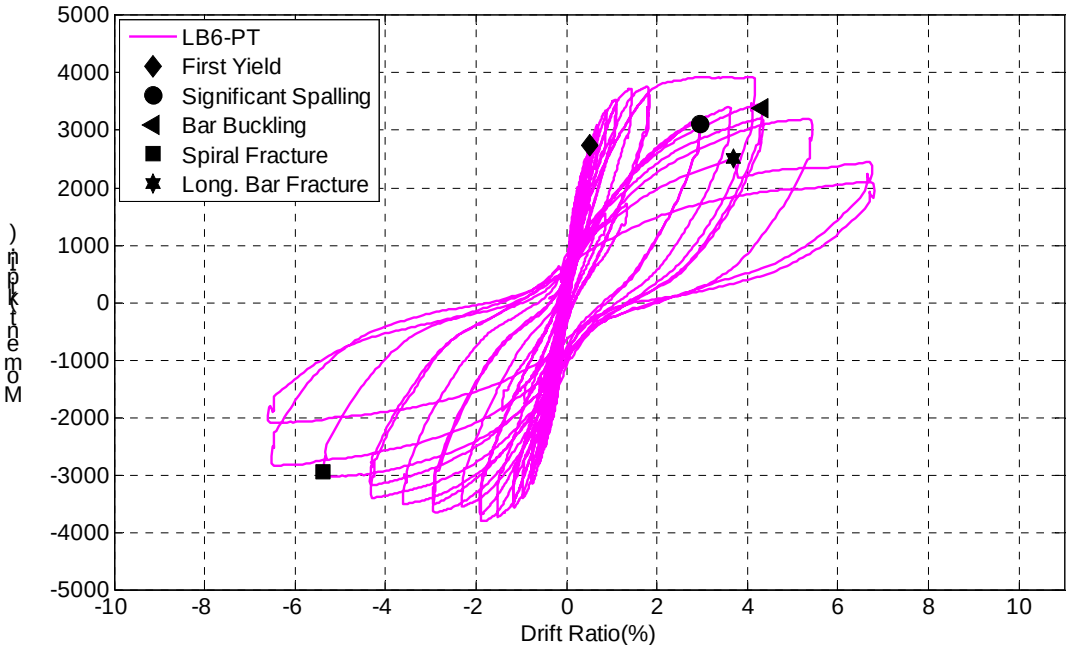

Figure 4-10. LB6-PT: moment drift ratio with major damage states marked.

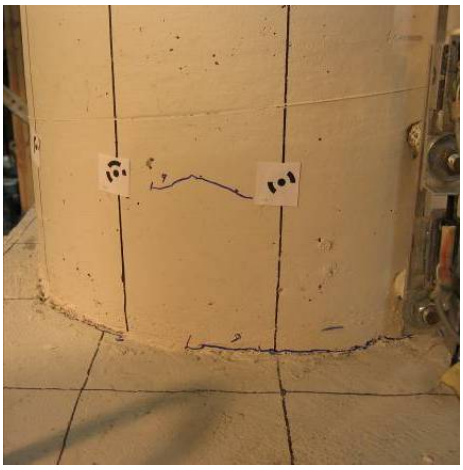

Figure 4-11. LB6-PT: column flexural cracks, Cycle 9 (-0.47%).

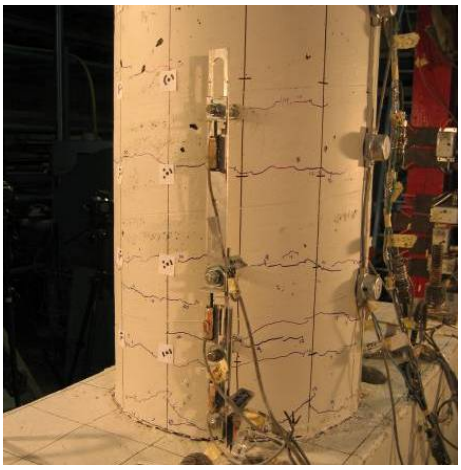

Figure 4-12. LB6-PT: column flexural cracks, Cycle 20 (-1.53%).

The tension yield strain (ε_y = 0.00254) in the longitudinal column bars was first measured at -0.58 percent drift by an interface gauge on the south side of Bar V18. This drift was near the peak negative drift of Cycle 12 (0.53 percent/-0.60 percent).

Until Cycle 24 (4.17 percent/-2.32 percent) the only new damage to the column was new flexural cracks (Figure 4-12). Most of the deformation was still concentrated at the interface crack. At Cycle 24 the peak south displacement was set to a drift ratio of 4.94 percent by mistake, almost 70 percent more than the intended drift ratio of 2.97 percent. Consequently the interface crack width at that cycle peak measured 10 mm, Bar V00 became visible through the crack, and the south side started spalling (figures 4-13 and 4-14). When the column was displaced north, the north side started spalling and the spiral became visible. On cycle 25 (2.95 percent/-2.94 percent) a portion of the cover spalled off on both sides of the column, exposing the first few spiral turns.

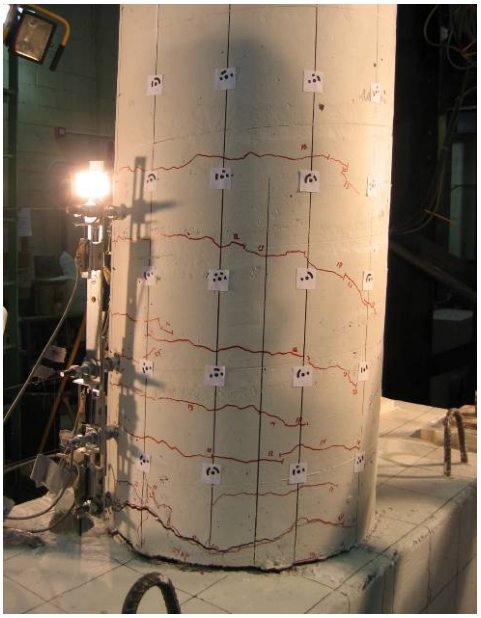

Figure 4-13. LB6-PT: Cycle 24 (4.17%), tension side.

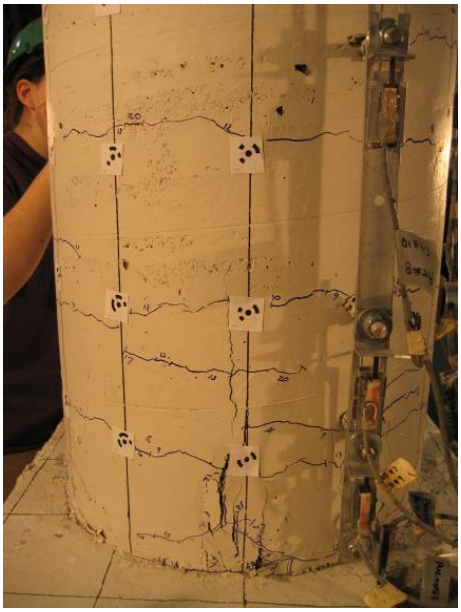

Figure 4-14. LB6-PT: Cycle 24 (4.17%), compression side.

Spalling increased over the next cycles, and on Cycle 28 (3.62 percent) Bar V00 became visible, and the spiral on the north side kinked. Bar V00 buckled on Cycle 29 (4.32 percent). The first spiral fractured (Figure 4-15) on the north side of the column (near Bar V00) during Cycle 32 (5.44 percent/-5.38 percent). On the next cycle (6.75 percent/-6.53 percent) Bar V00 fractured (Figure 4-16), and Bar V18 buckled. Bar V18 fractured on the cycle after that, which was a repeat of the same displacement as the previous one cycle. At this point the test was terminated (Figure 4-17).

Figure 4-15. LB6-PT: Bar V00 buckled and spiral fractured, Cycle 32 (-5.38%).

Figure 4-16. LB6-PT: Bar V00 fractured, Cycle 33 (6.75%).

Figure 4-17. LB6-PT: Maximum spall height at end of test, Bar V18 fractured, Cycle 34 (-6.61%).

4.4 Comparison of Specimen Damage Progression

The progression of damage was quite similar for the two test specimens and the one tested by Pang (2008). Initial cracking had occurred by Cycle 5 (~0.25 percent) for

both LB7-PT and LB6-PT, while it occurred at Cycle 1 for Pang's specimen LB8-D1 (~0.20 percent). First yield measured by a strain gauge happened at Cycle 12 for both PT specimens. Specimen LB7-PT yielded a little earlier, at a drift ratio of 0.41 percent whereas LB6-PT yielded at a drift ratio of -0.58 percent. Information about the yield strain of specimen LB8-D1 was not available because the gauges failed prior to yield. Pang's specimen LB8-D2, which was essentially the same as LB8-D1 but used a different debonded method, yielded at a drift ratio of 0.5 percent.

Flexural cracks extended farther up the column for specimen LB7-PT than for LB6-PT. At about 1 percent drift, cracks were visible as high as 20 in. up for LB6-PT and 25 in. up for LB7-PT. At about 2 percent drift cracks had formed as high up the column as 25 in. for LB6-PT and 35 in. for LB7-PT. Because the prestress-to-mild steel ratio was higher in LB6-PT than in LB7-PT, this difference was expected. In Specimen LB8-D1 cracks extended up to 36 in.

The column concrete started crushing two cycles earlier for LB7-PT, at a drift ratio of 1.41 percent and at a drift ratio of 1.81 percent for LB6-PT. The maximum spall height for LB7-PT was 14 in., while the maximum spall height for LB6-PT was only 9.5 in. The maximum spall height for LB8-D1 was 12 in.

Bar buckling in LB6-PT occurred during Cycle 29 at a drift ratio of -4.32 percent. In LB7-PT the first sign of bar buckling was in Cycle 30, which was a repeat of the previous cycle, at drift ratio of 4.45 percent. In specimen LB8-D1 both extreme longitudinal bars buckled in Cycle 32 (5.77 percent/-5.67 percent).

The first spiral fractured at Cycle 32 for both PT specimens; at a drift ratio of -5.32 for LB7-PT and at a drift ratio of -5.38 for LB6-PT. Specimen LB8-D1 suffered spiral fracture in Cycle 33 (7.11 percent/-7.06 percent). Bar fracture occurred in Cycle 33, for LB6-PT, but LB7-PT was cycled twice, with the second cycle being a repeat before bar fracture occurred on the next small cycle. Specimen LB8-D1 suffered longitudinal bar fracture in Cycle 34, which had a peak drift ratio of 7.20 percent.

The accidental "overload" of Specimen LB6-PT during Cycle 24 did not seem to affect the subsequent damage progression. Initial buckling and fracture of both of the column bars still happened at very similar drift levels.

A comparison between the specimens' drift ratios for major damage states can be found in Table 4-4 and Figure 4-18.

Table 4-4. A comparison of the specimens' drift ratios for the major damage states.

Specimen	Drift at initial cracking	Drift at initial yield	Drift at initial buckling	Drift at spiral fracture	Max. drift before bar fracture
LB7-PT	0.25%	0.41%	4.45%	-5.32%	6.74%
LB6-PT	0.26%	0.58%	-4.32%	-5.38%	-5.38%
LB8-D1	0.20%	0.50*	5.7%	7.11%	7.20%

* Strain gauges damaged prior to yield for LB8-D1. Drift ratio reported for LB8-D2

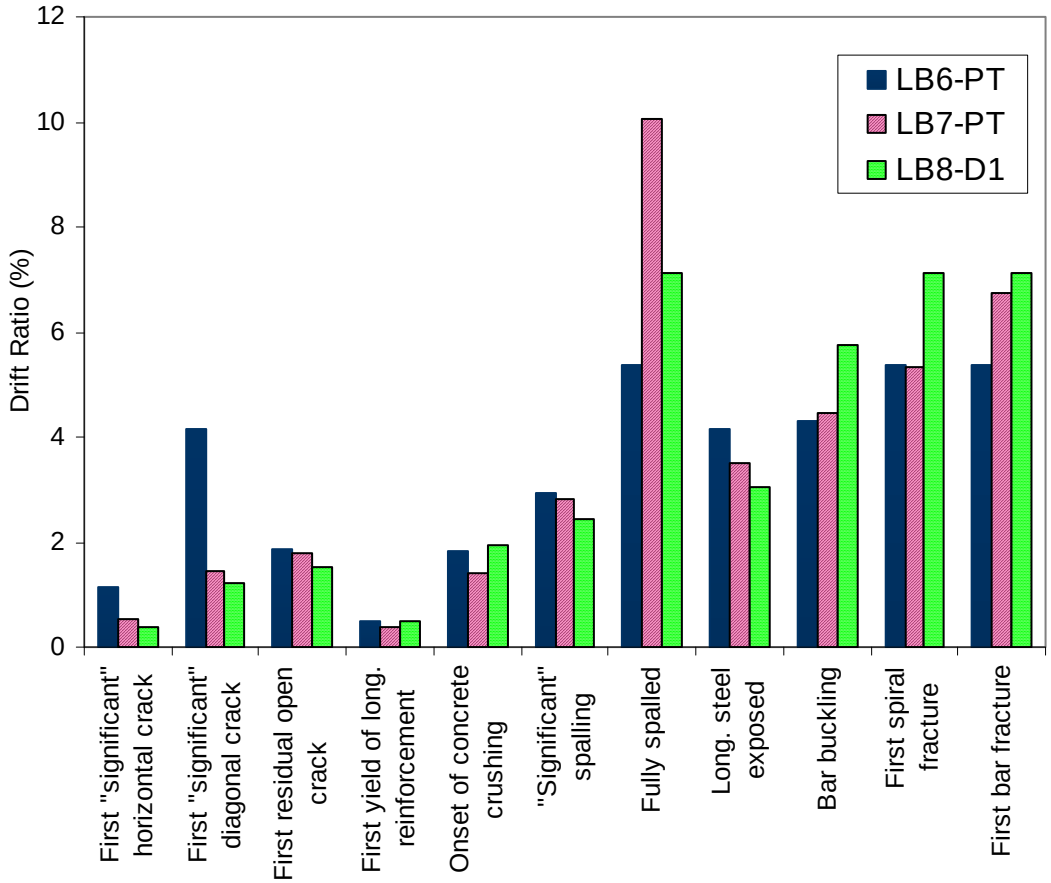

Figure 4-18. Comparison of specimens' drift ratios for the major damage states.

CHAPTER 5: MEASURED RESPONSE

5.1 Material Test Results

5.1.1 Concrete Strength

The specimens were constructed together in two concrete batches. Both cap-beams were cast first, followed by the columns. Concrete test cylinders (6 in. x 12 in.) were made from each batch to measure the concrete strengths at 7, 14, and 28 days, as well as test days. The concrete mix and details of these measurements can be found in Appendix B. The average cylinder strengths on the test day are reported in Table 5-1.

Table 5-1. Average concrete strength on day of test.

Specimen	Beam Concrete Strength (psi)	Column Concrete Strength (psi)
LB6-PT	7020	6530
LB7-PT	7420	6580

5.1.2 Grout Strength

For the large-bar grouted ducts, 2-in. x 2-in. grout cubes were made. Grout cube strength measurements were taken at 5, 15, and 30 days, as well as on test days. The average strength of the grout on the test day was 9.8 ksi for specimen LB6-PT and 9.7 ksi for LB7-PT. The details of the strength measurements can be found in Appendix B.

5.1.3 Mild Reinforcement Stress-Strain Results

To obtain the yield stress and ultimate strength of the mild steel, tension tests were performed on #6, #7, and #3 bars taken from the same heats as the bars in the specimens.

The measured stresses were based on nominal bar dimensions. Strains were measured with a clip-on extensometer, with an active gauge length of 3 in. for the #3 and #6 bars, and 3.25 in. for the #7 bar.

The #7 and #6 bars had yield plateaus, but the #3 bar did not. The yield strength for all of the bars was taken as the stress at 3.5 percent strain so as not to introduce any subjectivity into the result. The elastic modulus was calculated as the slope of a best fit line to the force-strain data in the elastic range, divided by the bar nominal area. Table 5- presents the yield stresses, ultimate stresses and the elastic moduli for the three test bars. The complete stress-strain curves can be found in Appendix B. The stresses and elastic modulus in Table 5-2 were calculated on the basis of the nominal value.

The calculated values for the elastic modulus were unusually small for the #6 and #7 bars, and rather large for the #3 bar. To evaluate the effects of using the nominal bar area as apposed to the real one, the actual bar area was assessed. The unit weight of each bar was calculated by weighing a known length of each bar. The actual bar area was then calculated by dividing that number by the rebar density. As presented in Table 5-2, the actual values were smaller, but the differences were not enough to account for the small value of E. The stress-strain curves for the #6 and #7 bars were smooth, with a very linear elastic portion. The #3 bar had noticeable stair-stepping in the stress-strain curve, which made evaluation of a representative E value more difficult.

Table 5-2. Measured mild steel properties.

Bar	f_y (ksi)	f_u (ksi)	E (ksi)	$A_{nominal}$ ($in.^2$)	A_{actual} ($in.^2$)
#7	59.8	93.7	21410	0.60	0.57
#6	70.6	100.7	25660	0.44	0.43
#3	66.5	98.7	33060	0.11	-

5.1.4 PT Bar Stress-Strain Results

The tensile stress-strain behavior for the PT bars was measured from two tension tests. One test was done on an unused coupon. A second test was done on a used coupon from the LB7-PT specimen test. The yield strength was determined to be 204 kips (129 ksi on the nominal area) by applying the 0.2 percent offset method to the unused bar results. The complete stress strain curves are presented in Appendix B.

5.2 Friction Correction

The test set-up, presented in Chapter 3 introduced external friction forces into the system, which contributed to the column resistance measured in the tests. The two sources of friction were the two sliding surfaces of the bearing. Rotation occurred at a greased, steel-on-steel, spherical element, and translation occurred across a flat, greased PTFE-on-stainless steel sliding surface. Both surfaces contributed to the overall frictional resistance, and it is likely that their relative contributions varied with displacement level. In the interest of simplicity the friction was modeled as arising from a single, constant source.

The friction coefficient used in this analysis was measured in earlier experiments with an identical test setup. Brown (2008) established a value of approximately 1.6 percent, although that value was measured for a higher axial load. That value was used here to be consistent with the analysis of Pang's four columns, for which that value was also used.

The friction force was modeled as a linear spring, limited by a maximum force, as shown in Figure 5-1. In this figure, $F_{\max} = \mu \cdot P_{col}$ and $F_{\min} = -\mu \cdot P_{col}$, where μ is the coefficient of friction and P_{col} is the target axial load. The spring stiffness, k, was taken as 60 kips/in., based on the test data for the two test columns in this study and the four test columns from Pang (2008). It represented the flexibility of the nominally rigid head of the test machine.

The friction force at data point *j* was calculated as:

$$F_j = \min\left\{ \begin{array}{c} F_{\max} \\ \max\left\{ \begin{array}{c} F_{j-1} + k \cdot \left(\Delta_j - \Delta_{j-1}\right) \\ F_{\min} \end{array} \right. \end{array} \right. \qquad \textbf{5-1}$$

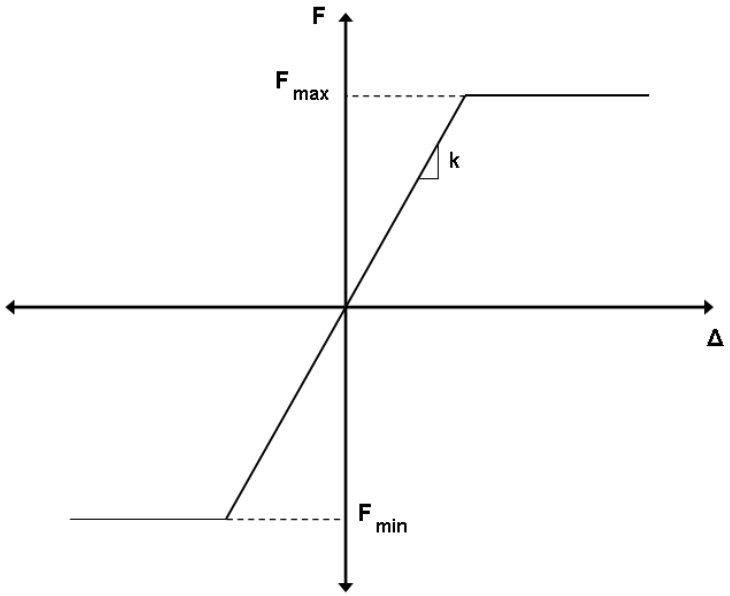

Figure 5-1. Friction force model.

5.3 Moment-Drift Response

Figure 5-2 illustrates the procedure for calculating the column moments. The friction acted at the top of the column rather than at the height of the horizontal load, H. However, Brown (2008) determined its value from measured data by treating it as though it acted at the same elevation as the horizontal load, so the same was done here. The use of the loading ring for transferring the axial load to the column resulted in a larger distance from the column interface to the applied vertical load, h_P, for the two PT specimens than for the column tested by Brown (2008) and LB8-D1 tested by Pang (2008). Nevertheless, the same friction coefficient was used for all columns. It was necessary to approximate the lateral displacement at the top of the column by using similar triangles because the displacement Δ_H was available, but no instrument could easily be placed at the sliding bearing.

The moment was calculated as follows:

$$M = h_H \cdot (H - F) + \Delta_H \cdot \frac{h_P}{h_H} \cdot P_{col} \qquad \textbf{5-2}$$

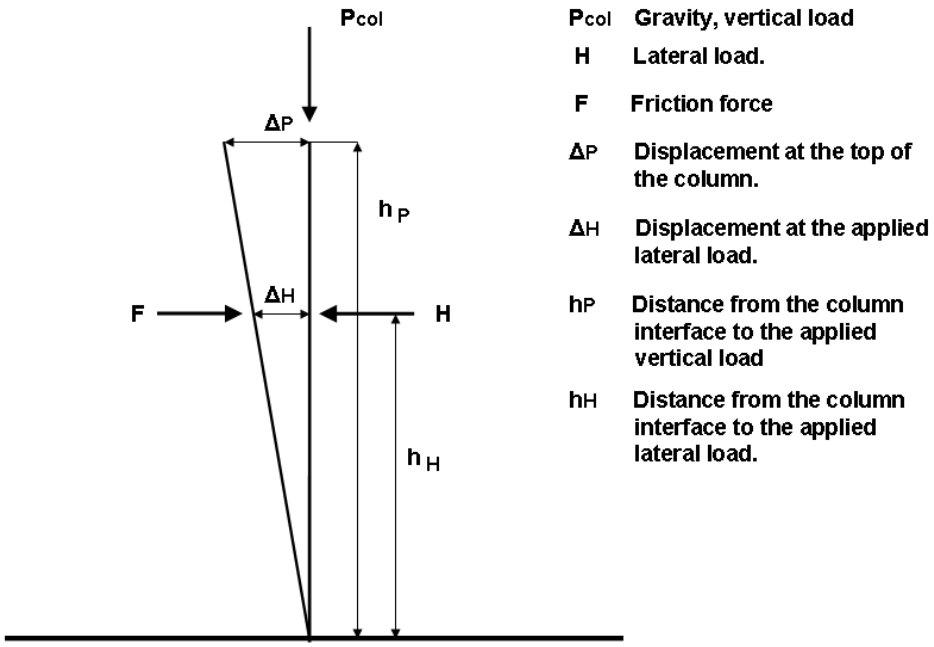

Figure 5-2. Approximating lateral displacements at the applied vertical load.

The drift ratio was calculated as the measured lateral displacement at the applied lateral load (Δ_H) divided by the distance from the column-to-beam interface to the applied lateral load (h_H)

The moment-drift responses for specimens LB6-PT and LB7-PT are shown in figures 5-3 and 5-4.

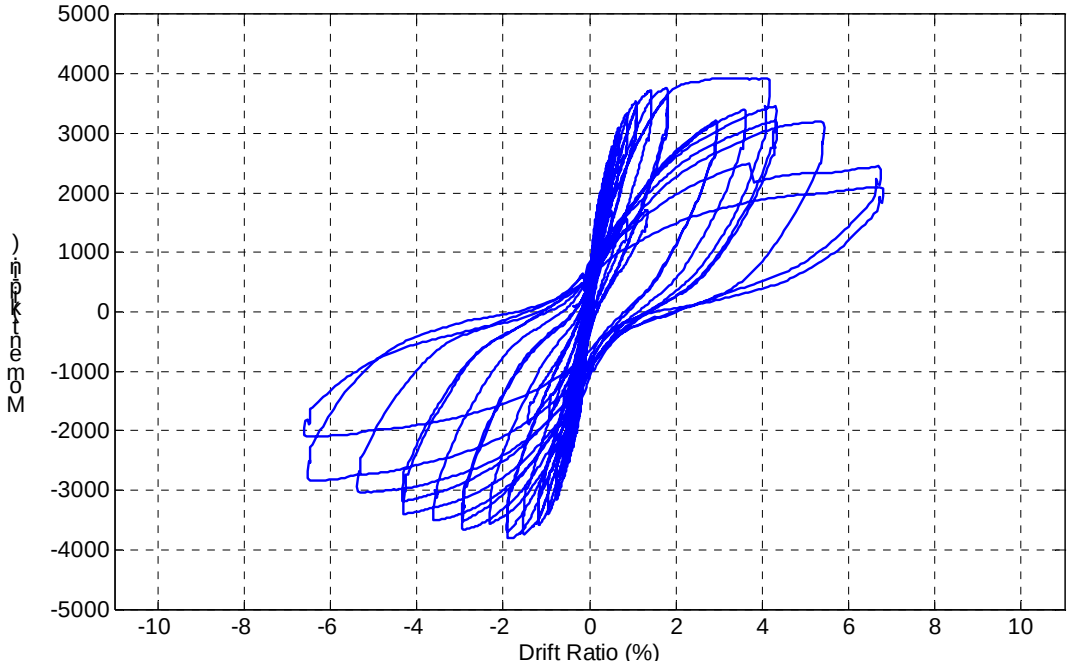

Figure 5-3. Specimen LB6-PT: moment-drift response.

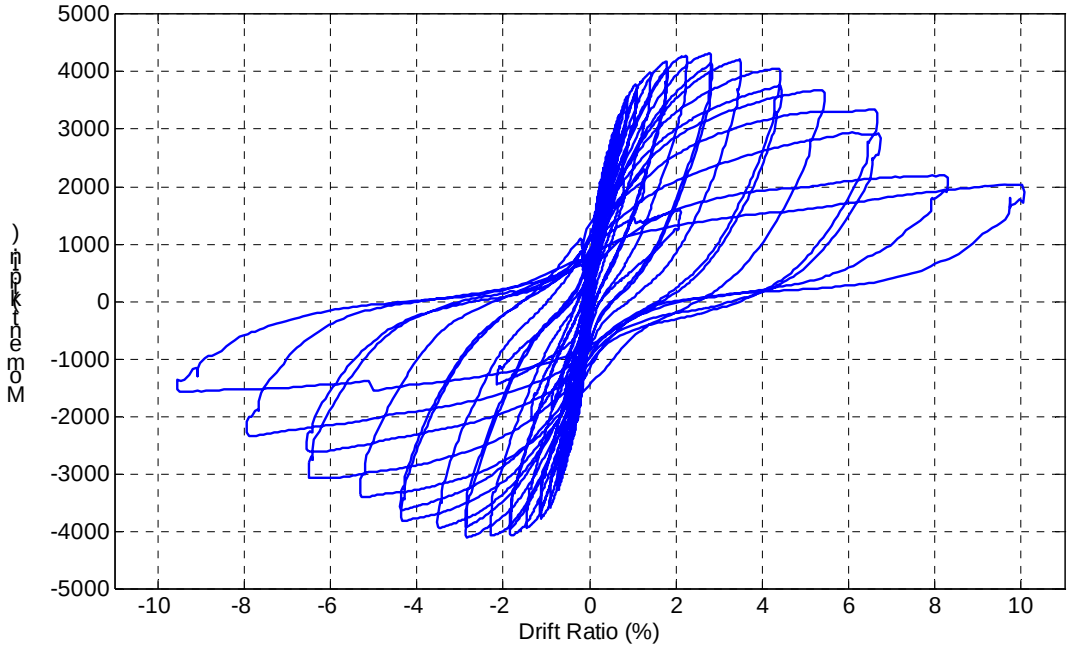

Figure 5-4. Specimen LB7-PT: moment-drift response.

Specimens LB6-PT and LB7-PT were both subjected to the displacement history described in Section 3.4, with the exception of Cycle 24 in the testing of LB6-PT. During

that cycle the specimen was unintentionally overloaded to a drift ratio of 4.2 percent in the positive loading direction instead of the target drift ratio of 2.97 percent. This cycle can be seen in the moment-drift response in Figure 5-3.

A comparison of the moment-drift responses for the two PT specimens and Specimen LB8-D1 from Pang is shown in Figure 5-5.

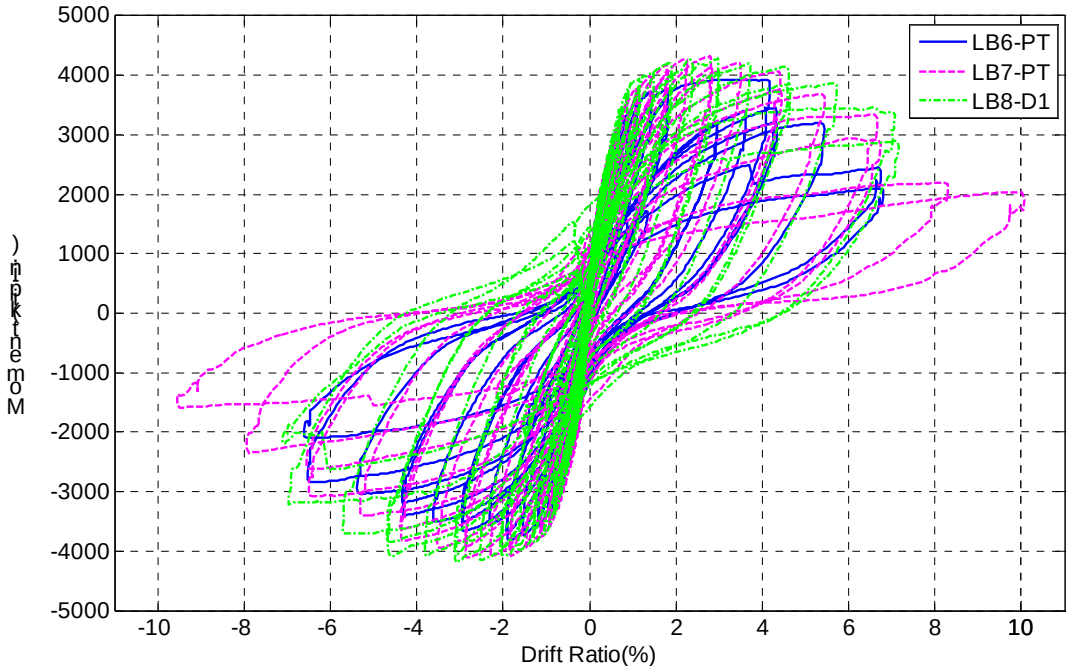

Figure 5-5. Comparison of moment-drift responses.

Table 5-3 presents the key measured peak responses during testing. The peak responses of the three specimens were similar but not identical. Discussions of the effective force and PT force can be found in Section 5.4 and Section 5.7, respectively.

Table 5-3. Peak measured responses.

Key Peak Responses	LB6-PT	LB7-PT	LB8-D1
Max. Moment (kip-in.)	3924	4323	4288
Min. Moment (kip-in.)	-3809	-4110	-4180
Max. Effective Force (kips)	65.4	72.1	71.5
Min. Effective Force (kips)	-63.5	-68.5	-69.7
Max. PT Force (kips)	188	197	N.A.

A dimensionless comparison of the moment-drift relationship for the three specimens is shown in Figure 5-6. Here the applied moment of each test was normalized by its respective overall peak moment from the test. The normalization makes it easier to compare the shapes of the response curves.

At the load reversal points, specimens LB6-PT and LB7-PT had almost identical responses. These were also very close to the response of the non-prestressed specimen LB8-D1. However, at larger drift ratios LB8-D1 showed a slightly higher resistance.

A distinct difference in the moment-drift behaviors at larger drifts can be seen between the prestressed specimens and LB8-D1 at the points where the curves cross the zero-load axis. At that location the LB6-PT curves are closer to the origin than the curves for LB7-PT. LB8-D1 is even farther away from the origin than is LB7-PT. This trend is consistent with the fact that LB6-PT had the highest calculated re-centering ratio. Specimen LB8-D1 had a re-centering ratio lower than 1.0, which implies little or no re-centering capability. Residual displacements are discussed in Section 6.4, and they are compared with the re-centering ratios calculated over the course of the tests in Section 6.5.

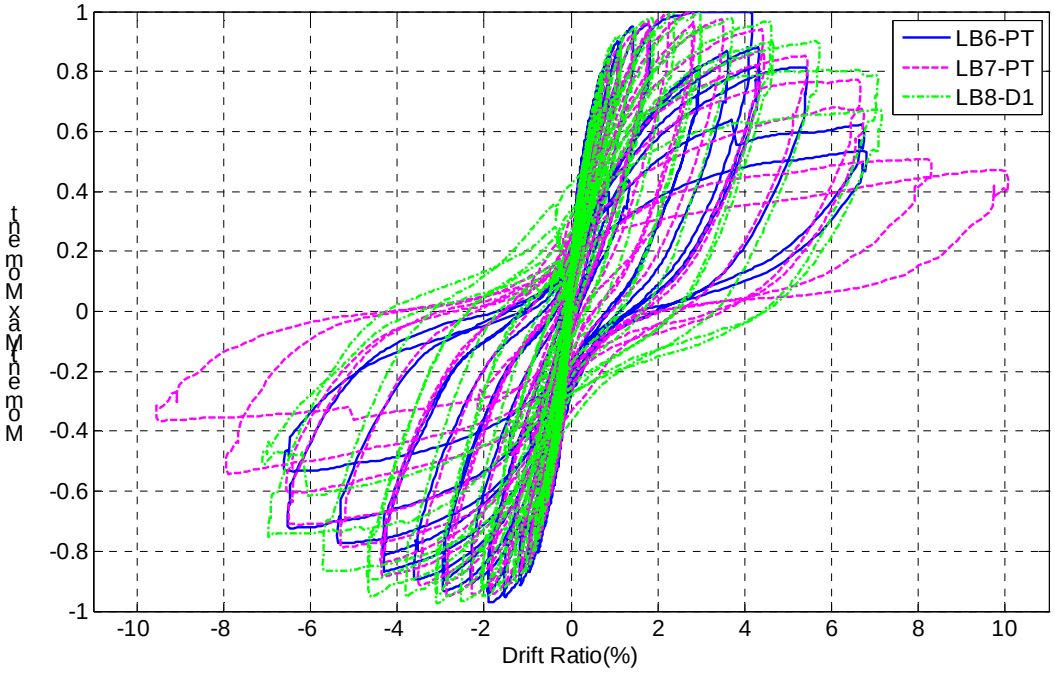

Figure 5-6. Normalized moment-drift comparison.

5.4 Effective Force

The effective force was calculated by dividing the moment calculated with Equation 5-2 by the distance from the column interface to the applied lateral load:

$$F_{Eff} = M / h_H \qquad \textbf{5-3}$$

Figures 5-7 and 5-8 show the effective force vs. displacement for specimens LB6-PT and LB7-PT. Aside from the $1/h_H$ factor and that they show displacement as opposed to drift ratio, these plots are identical to figures 5-3 and 5-4.

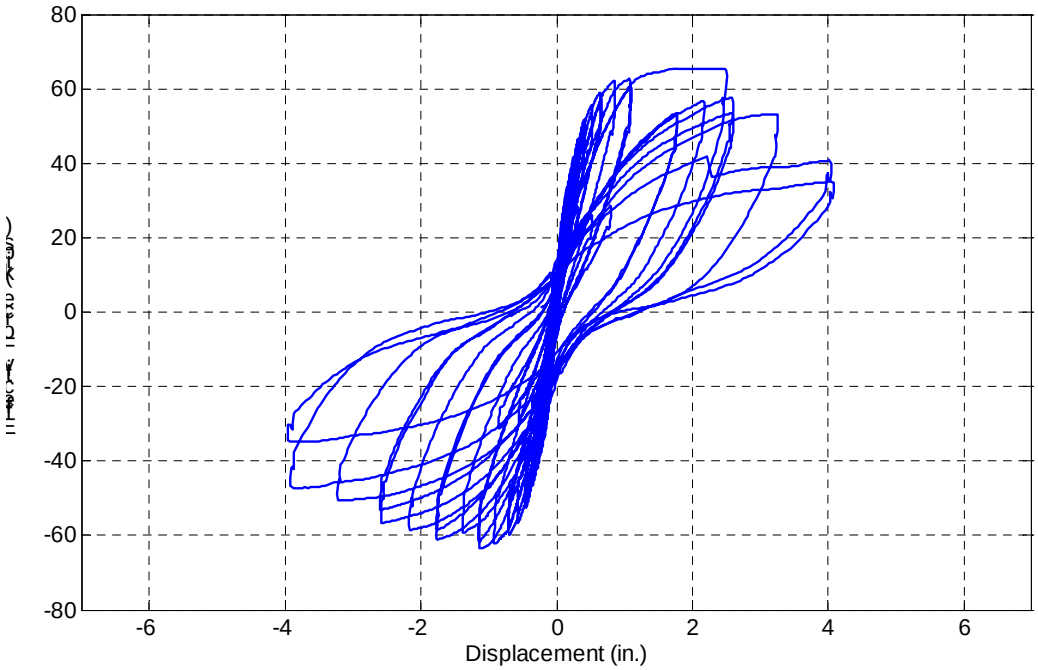

Figure 5-7. Specimen LB6-PT: effective force vs. displacement.

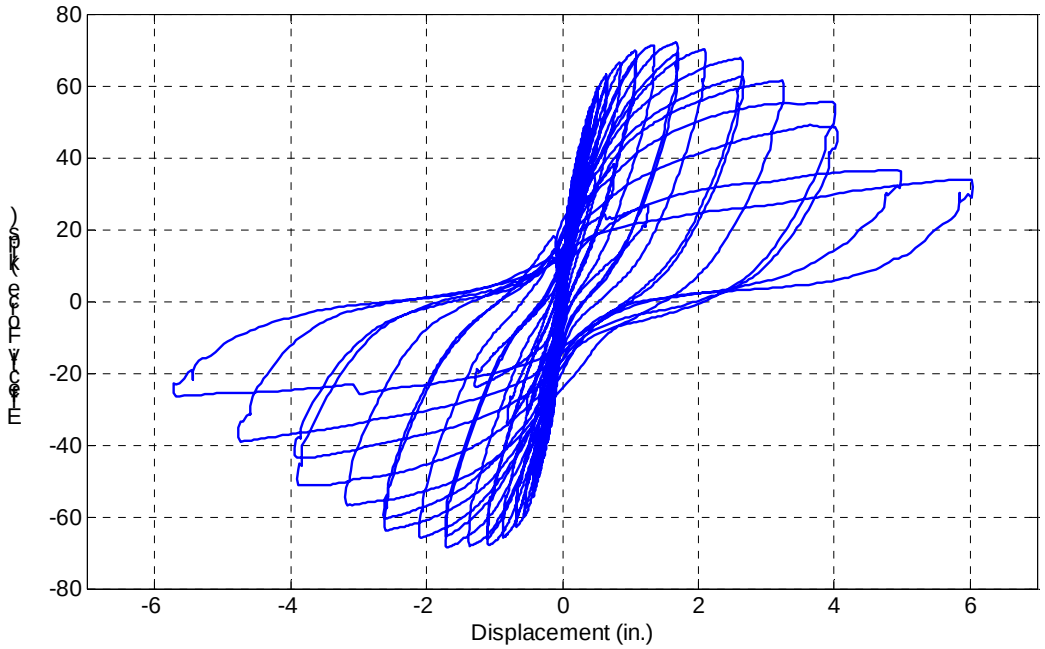

Figure 5-8. Specimen LB7-PT: effective force vs. displacement.

5.5 Column Rotation

Vertical potentiometers were located in pairs at four places along the column. They measured the rotations occurring in the segments 0 to 1.75 in., 1.75 to 6.50 in., 6.50 to 11.75 in., and 11.75 to 21.50 in. up from the interface. Figure 5-9 shows the set-up for these instruments. The rotations were calculated according to Equation 5-4 for each section by using measurements from the pots located at the top of each section.

$$\vartheta_i = \frac{\delta_{i,N} - \delta_{i,S}}{L_i} \qquad \textbf{5-4}$$

where δ_i is the displacement measured at section *i* by the north side or south side potentiometer and L_i is the horizontal distance between the two instruments.

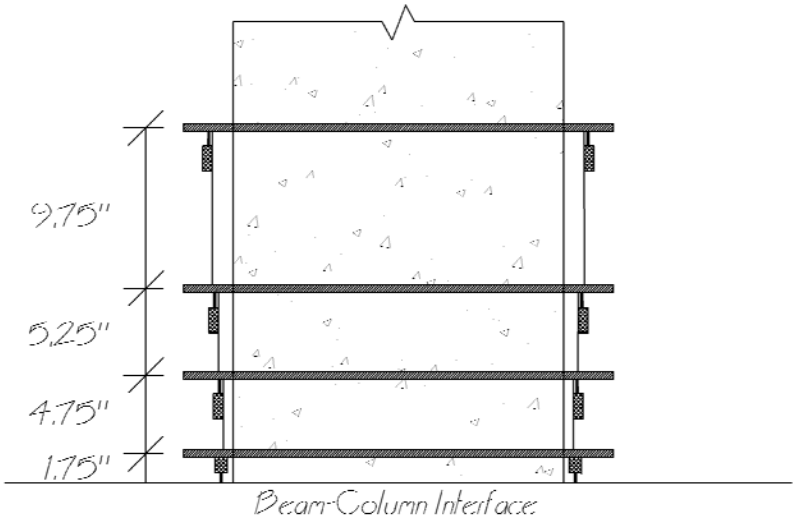

Figure 5-9. Schematic of the column-rotation instruments.

The segment rotations for LB6-PT and LB7-PT are plotted in figures 5-10 and 5-11. For both specimens, rotations were concentrated at the interface. This behavior was to be expected, as the connection was weaker than that of either the column or cap-beam, and the largest moment occurred there, so the crack that formed there was much larger than the cracks elsewhere. This behavior was consistent with the behavior expected in a connection of precast elements in which the members move like rigid bodies and nearly all the deformation occurs at the connections. Figure 5-12 shows that the rotations at the column interfaces for peak drift ratios of each cycle were very similar for the two PT specimens and LB8-D1.

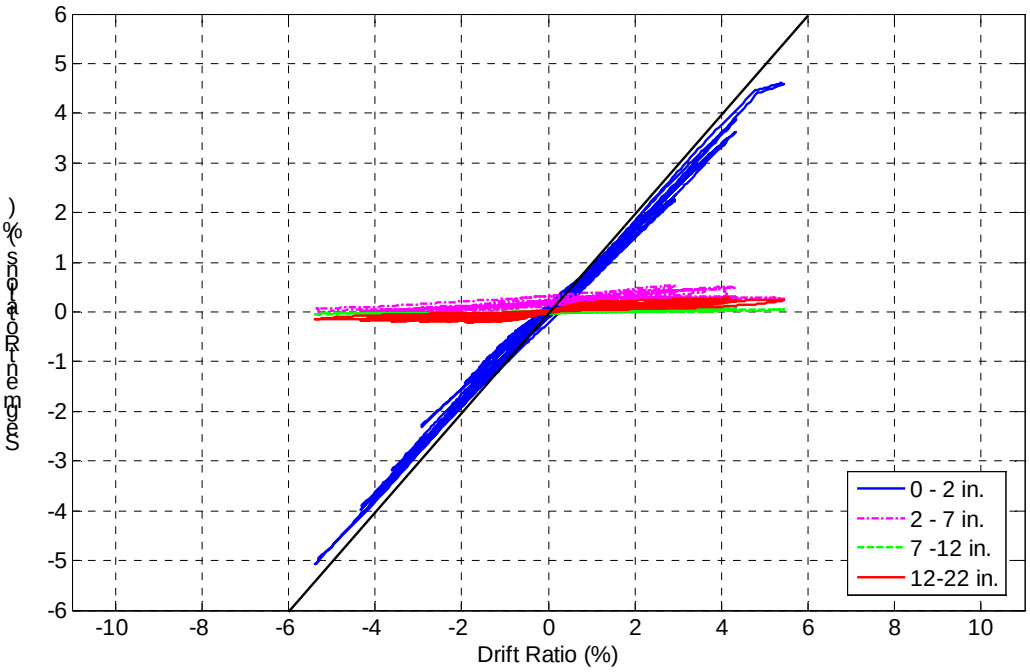

Figure 5-10. Specimen LB6-PT: column segment rotations.

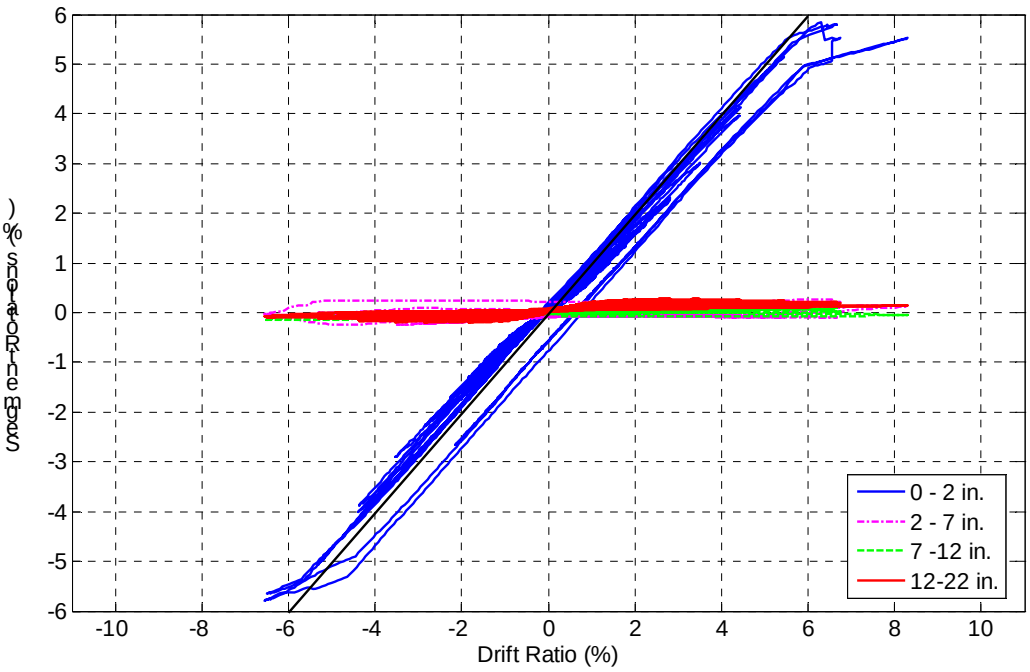

Figure 5-11. Specimen LB7-PT: column segment rotations.

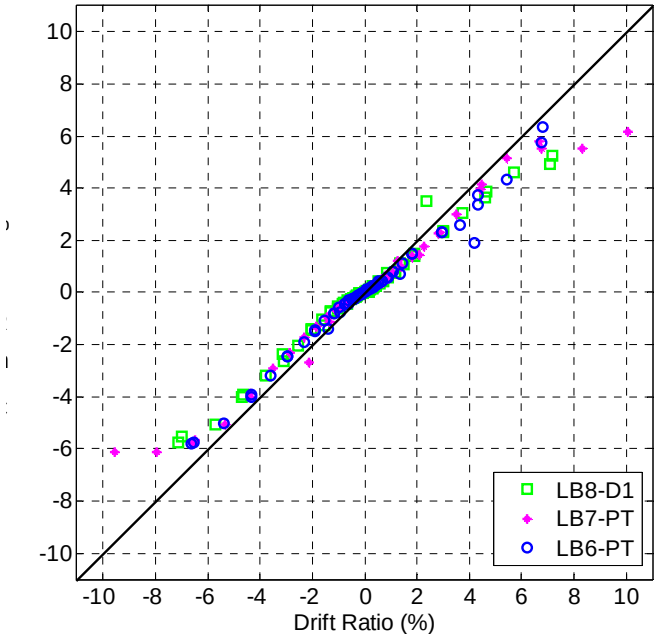

Figure 5-12. Comparison of interface rotations for cycle peak drift ratios.

5.6 Column Curvature

The average curvature for each segment was calculated by using Equation 5-5:

$$\varphi_i = \frac{\delta_{i,N} - \delta_{i,S}}{L_i} \Big/ H_i \qquad \textbf{5-5}$$

where δ_i is the displacement measured at that segment by the north side or south side pot, L_i is the horizontal length between the two pots, and H_i is the height of each segment.

Figures 5-13 and 5-14 present the curvature profiles at various drift levels for LB6-PT and LB7-PT, respectively. The curvatures presented are those that occurred when the specimens reached a given drift ratio for the first time. The curvature at the top of the column was always taken as zero. The average curvature within any segment applies to the whole segment, but for clarity it is shown as a point value in the middle of the segment.

As was the case for the column segment rotations, the curvature distributions show that the columns were moving essentially as rigid bodies, with all the deformation occurring in the bottom segment.

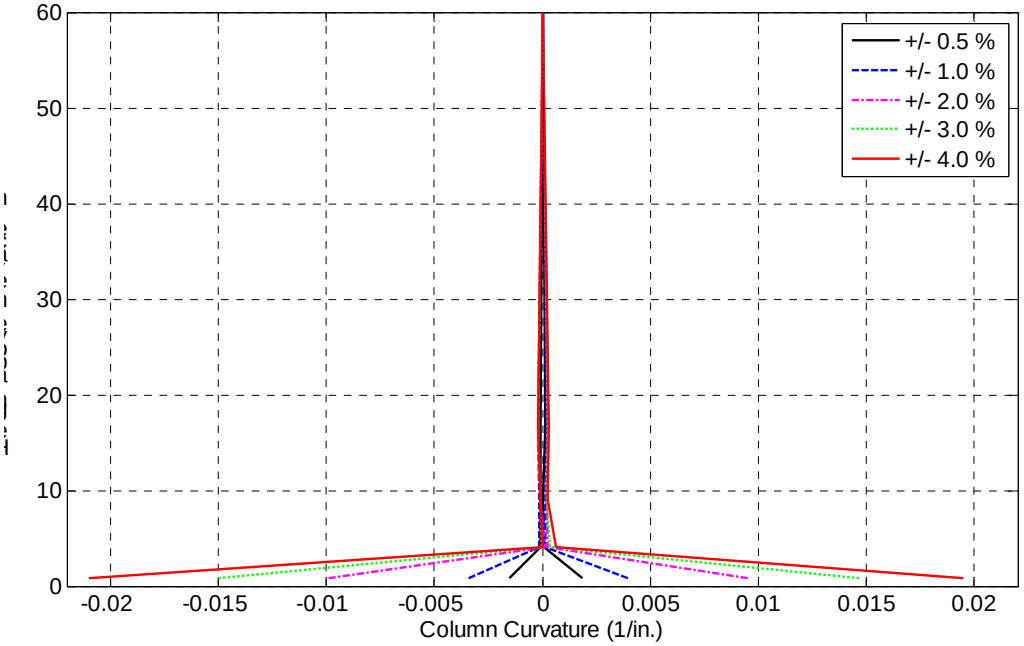

Figure 5-13. Specimen LB6-PT; distribution of column curvatures.

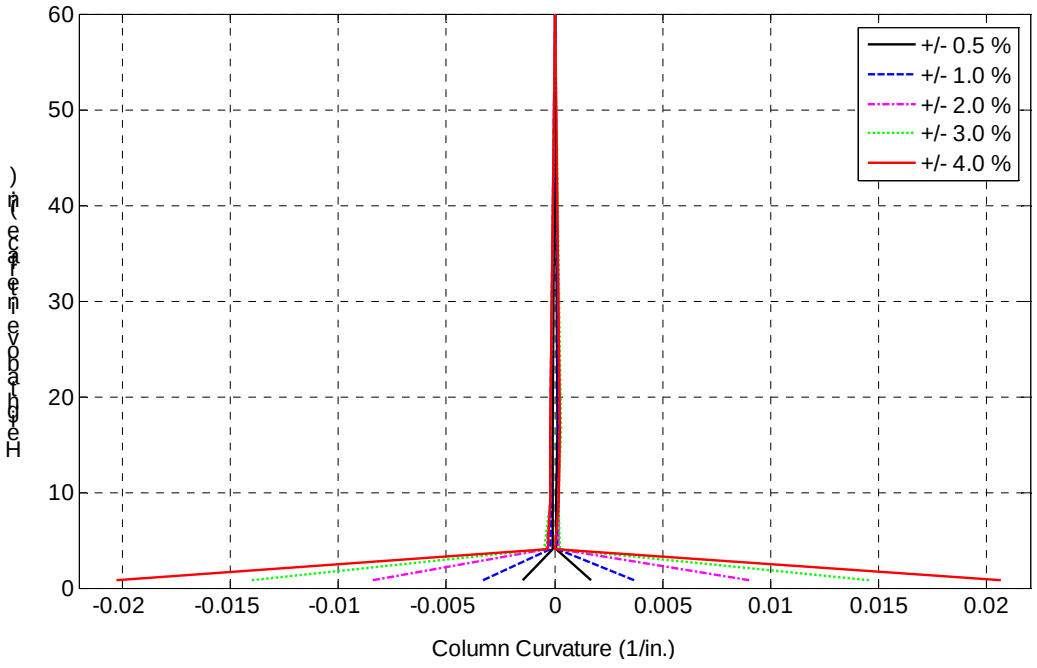

Figure 5-14. Specimen LB7-PT: distribution of column curvatures.

5.7 Axial force in the PT Bar

The axial force in the PT bar varied during the test. It is plotted in figures 5-15 and 5-16 against drift ratio for specimens LB6-PT and LB7-PT, respectively. The small drop in axial load close to zero drift in both figures was due to column shortening as the external axial load was applied. As the column displaced laterally, the PT bar elongated and the force in the bar increased.

While the column remains elastic, the strains increase to peak displacement is recovered when the displacement returns to zero. However, when the bar yields or damage occurs in the column, such as spalling and concrete crushing, the force in the PT bar is expected to decrease. The behavior of the bar was monitored by a load-cell, which measured the change in force in the bar during the test. Key PT forces for both specimens are presented in Table 5-4. The bar was threaded, so no gauges could be applied without damaging the threads. Therefore, it was not possible to measure the residual strain at the end of the test, which would have indicated directly the extent of yielding. The relative contributions of bar yielding and concrete crushing to the loss of PT force evident in figures 5-15 and 5-16 are investigated in Section 6.3.

Table 5-4. Summary of key PT forces.

Specimens	LB6-PT	LB7-PT
Force at test initiation (kips)	140.3	141.3
Maximum force (kips)	188.1	197.2
Percentage increase	34%	39%
Minimum force (kips)	93.0	92.3
Percentage decrease	34%	35%

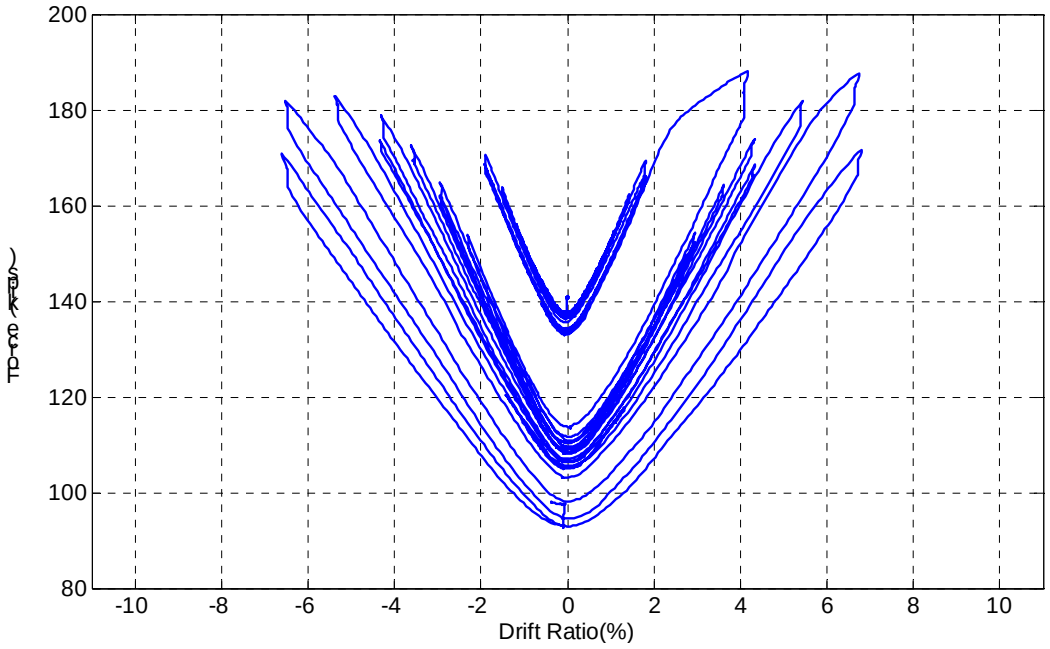

Figure 5-15. Specimen LB6-PT: force in the PT bar vs. drift ratio.

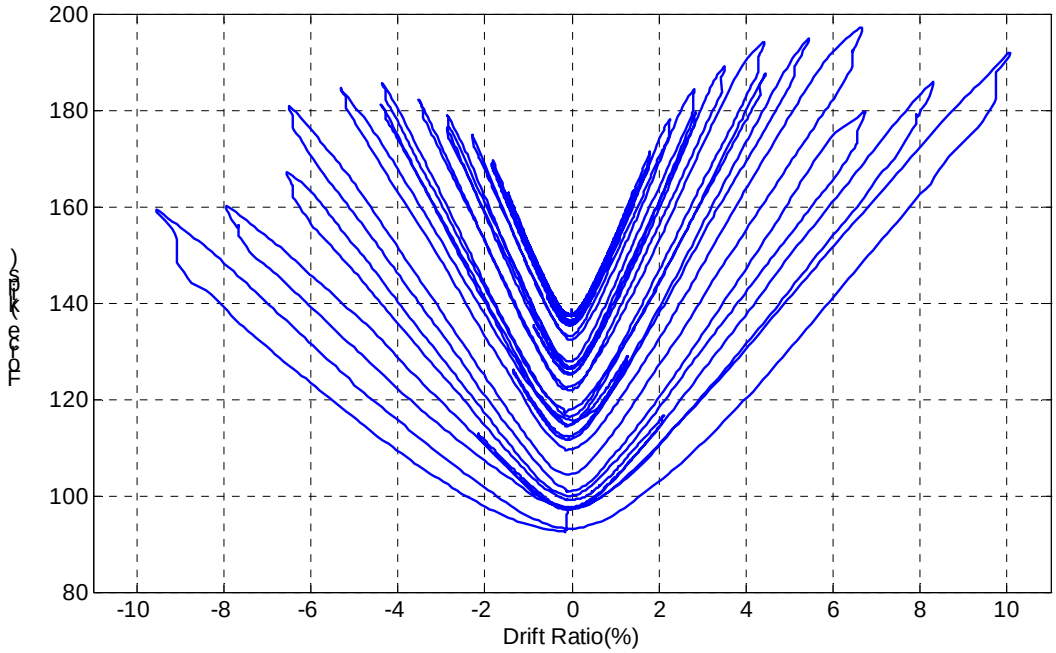

Figure 5-16. Specimen LB7-PT: force in the PT bar vs. drift ratio.

Figures 5-17 and 5-18 show the PT bar force during the test normalized by the bar force at the beginning of testing, before axial load was applied (when the DAQ measurements were initiated) for specimens LB6-PT and LB7-PT, respectively.

The maximum PT force increase in Specimen LB6-PT was 34 percent of the PT force at the start of the test and 39 percent for Specimen LB7PT. These maxima occurred in both specimens in the positive loading direction at 6.7 percent drift. For cycles up to ± 2 percent drift ratio, the behavior was essentially elastic and the bar lost almost no force at zero drift. At the end of the test, the loss of the PT bar force at zero drift was about 35 percent of the starting force for the specimens.

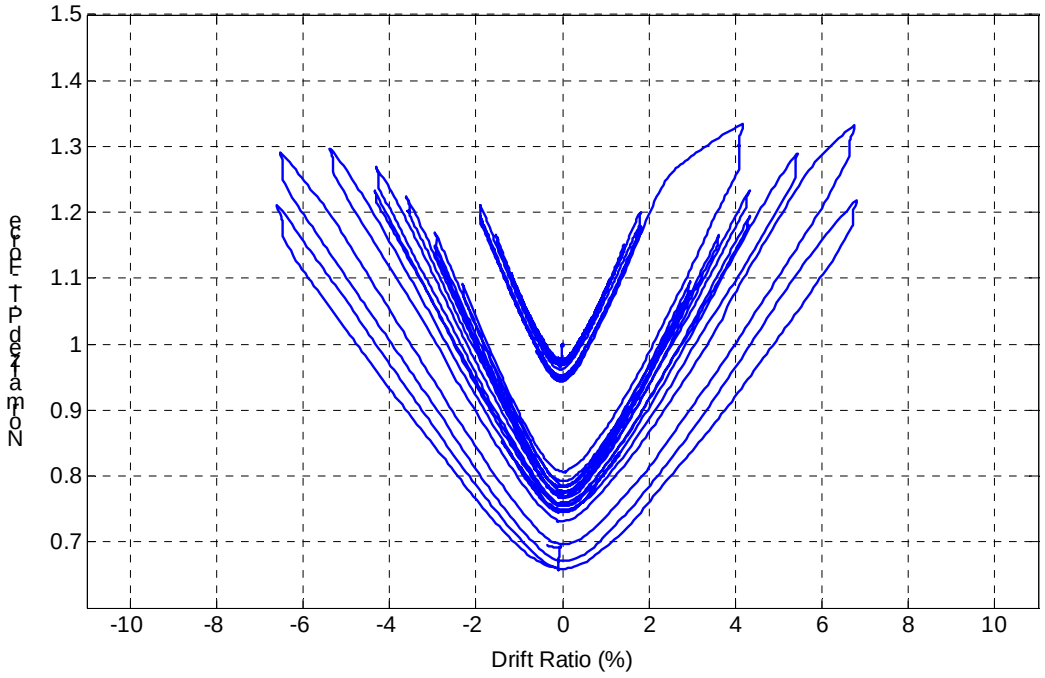

Figure 5-17. Specimen LB6-PT; normalized force of the PT bar vs. drift ratio.

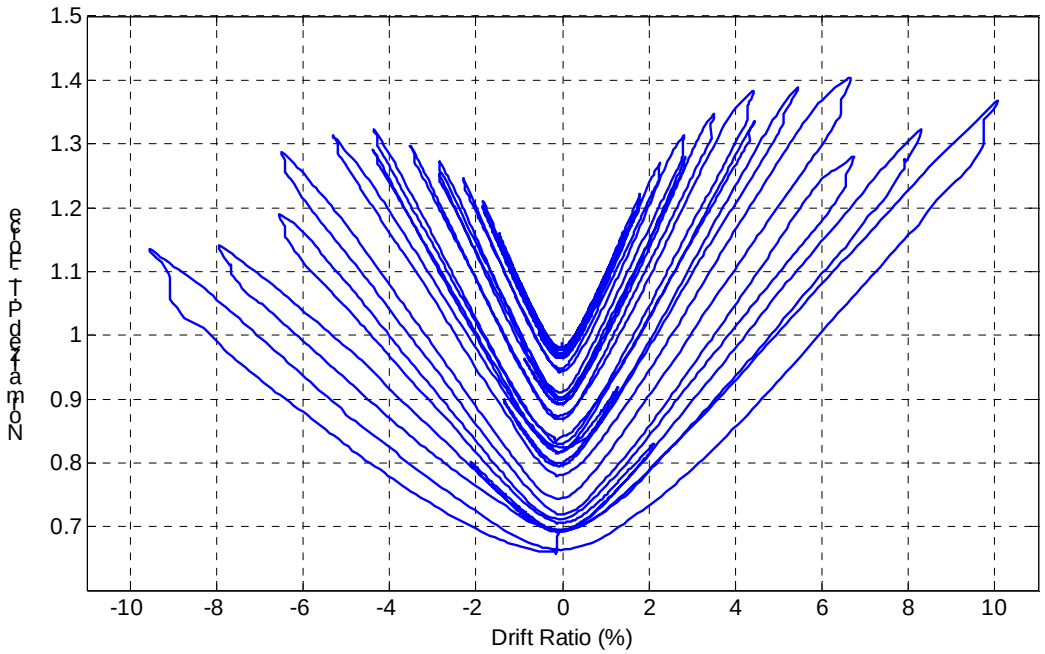

Figure 5-18. Specimen LB7-PT; normalized force in the PT bar vs. drift ratio.

The behaviors of the PT bars in the two specimens are compared in Figure 5-19, which shows the envelope of the PT bar force during testing, normalized by the bar force at the beginning of each test. The loss of the PT bar force as the axial load was applied can be seen as the small drop in force close to zero drift. The rate of change of the PT bar force with drift is approximately linear up to a drift ratio of 2 percent for both specimens. At drift ratios exceeding 2 percent, losses in the PT bar force started to occur as a result of yielding of the bar or damage to the column. At the 2 percent drift level in the positive direction, the unintentional overloading of Specimen LB6-PT is apparent; this resulted in a considerable loss in the PT bar force in both directions.

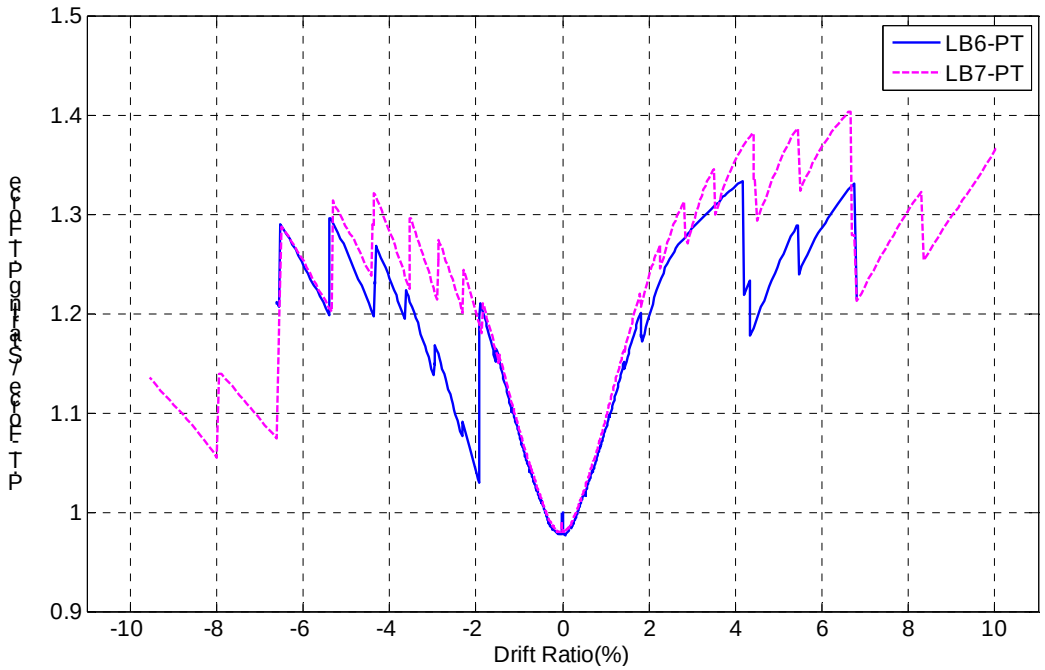

Figure 5-19. Comparison of the envelope plots for PT force normalized vs. drift ratio.

Figure 5-20 shows the relationship between the changes in bar force during the cycle vs. peak drift ratios for both specimens LB6-PT and LB7-PT. The slope, plotted on the vertical axis, is the ratio of the change in bar force and the change of the drift ratio from zero to peak drift of each half-cycle. The response is similar for both specimens. It reaches a maximum in both loading directions at around 2 percent drift. This is when loss of PT bar force is first noticeable in Figure 5-19. In the positive direction, the slope of LB6-PT after 2 percent is lower than that of LB7-PT. This is attributed to the overloading in cycle 24, because the slopes are similar in the negative direction.

The PT bar force at zero drift normalized by the respective PT bar force at the beginning of testing is plotted vs. the previous maximum or minimum drift ratio for both specimens in Figure 5-21. It shows the decrease of the PT bar force at zero drift that starts occurring after both specimens reach and pass the 2 percent drift level.

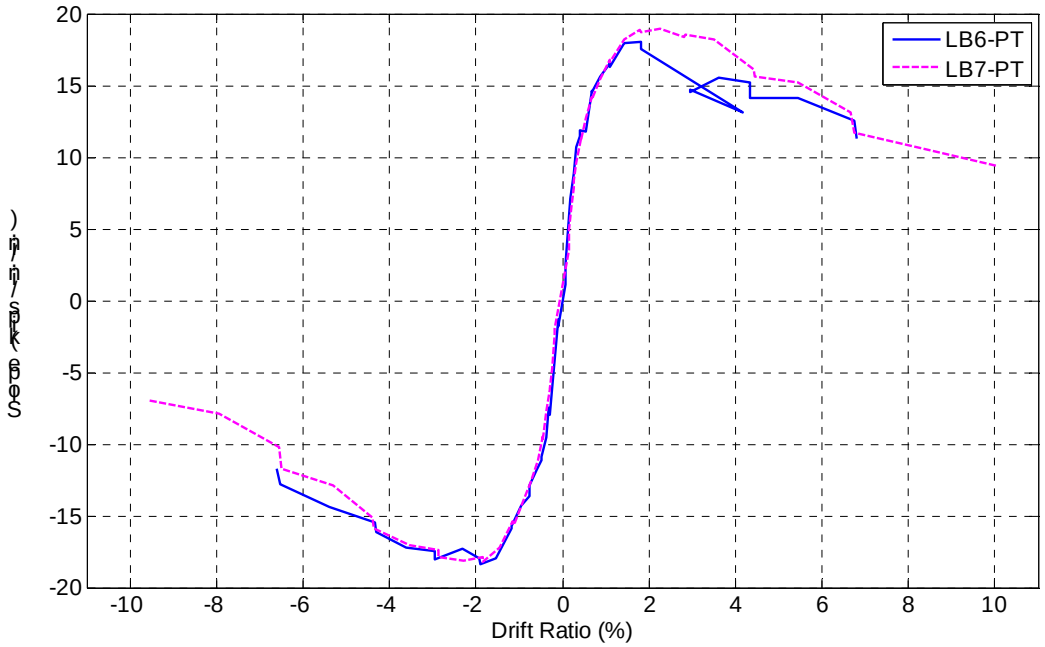

Figure 5-20. Comparison of the rate of increase of force in the PT bar vs. drift ratio.

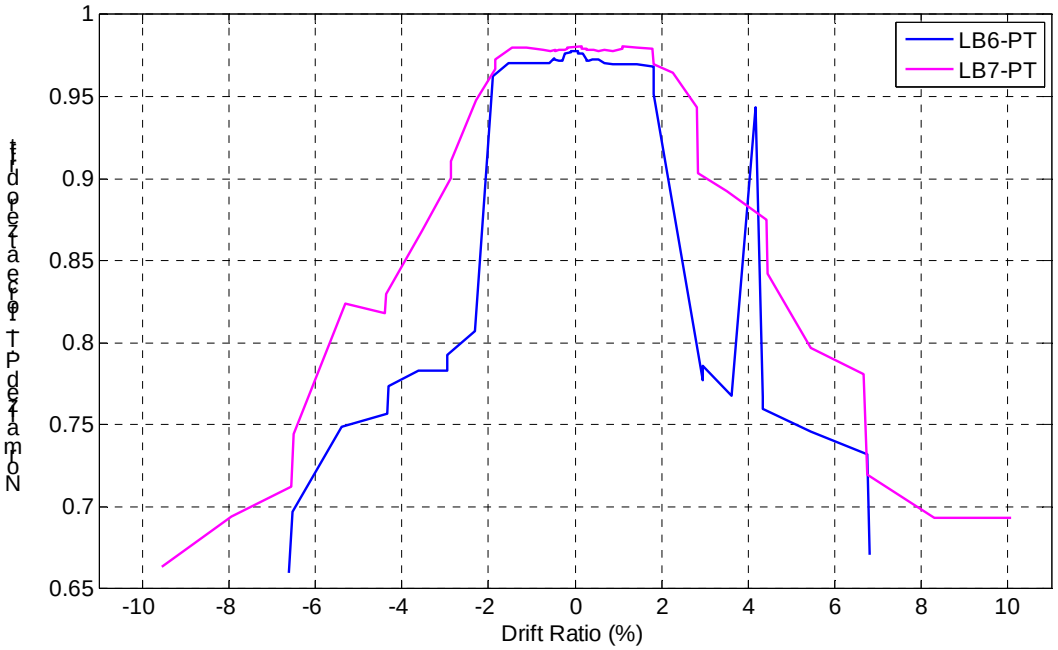

Figure 5-21. Comparison of normalized PT force at zero drift vs. peak drift ratio.

5.8 Column Axial Lengthening

The four sets of two potentiometers located on the north and south sides of the column (Figure 5-9) were used to compute the rotations at the segments as described in Section 5.5. They were also used to compute the average elongations at the column centers throughout the tests, and these are shown in figures 5-22 and 5-23. It is interesting to note that the column height at zero displacement increased during the test.

This will be discussed further in connection with the PT bar force in Section 6.3.

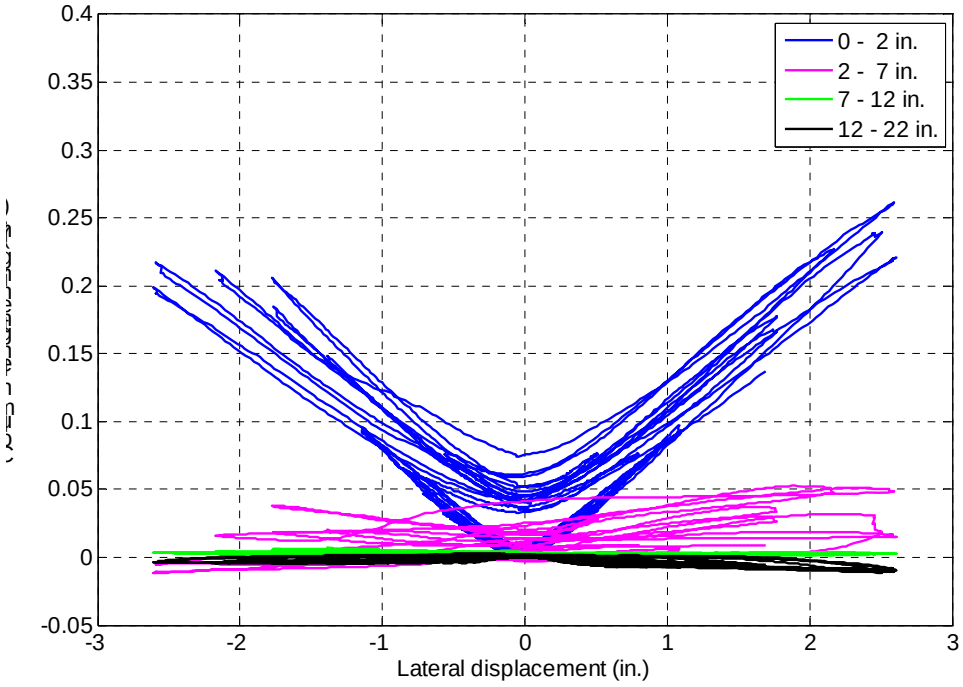

Figure 5-22. Specimen LB6-PT: axial lengthening of the column vs. displacement.

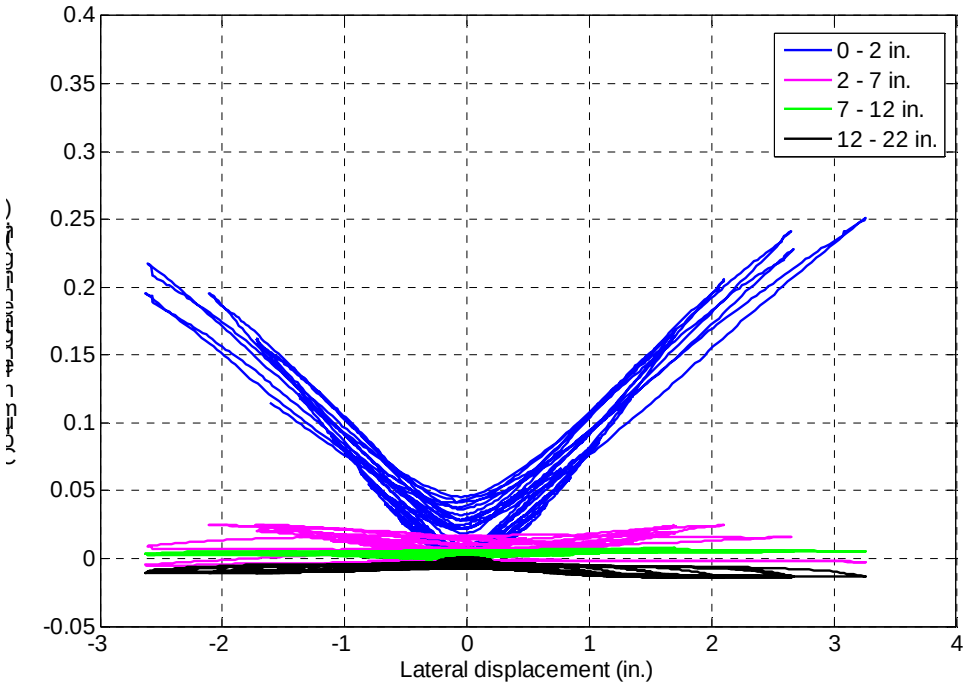

Figure 5-23. Specimen LB7-PT: axial lengthening of the column vs. displacement.

5.9 Strains in Mild Steel Reinforcement

5.9.1 Strain Distributions

Vertical column bars V00 and V18 were expected to develop the largest strains during the tests, because they lay farthest from the axis of rotation. They were therefore instrumented the most heavily. On each bar, three gauges were located above the interface in the column. The gauges were placed at 1/3-, 2/3-, and one-column diameter up the column from the interface. These gauges were placed on the outside of the bars. At and below the interface, ten gauges were located in pairs on each outside and inside of the bar, at 0, 7, 15, 18, and 25 inches below the interface. All gauges functioned well except for gauge V18-07N (located on the inside of bar V18, 7 in. down in the cap beam) in Specimen LB6-PT. Strain gauge V18-07N was most likely damaged during casting of the cap beam. A detailed explanation of the strain gauge instrumentation can be found in Section 3.5.3.

Profiles of the strains in both bars (V00 and V18) for both test specimens are plotted for a variety of drift levels in figures 5-24 through 5-27. The strains are plotted only up to a drift ratio of ±1.4 percent because after that, strain gauge V00+00N (located

at the interface of bar V00, north side) for both specimens started to delaminate and did not provide reliable strain readings. The figures show strains for all gauges, and lines are drawn to connect single markers or the averages of two markers when gauges were located on both the outer and inner sides of the bar.

The lines drawn to connect the average strains for the location of the damaged gauge in LB6-PT (Figure 5-25) are affected by the damaged gauge and should be viewed with that in mind.

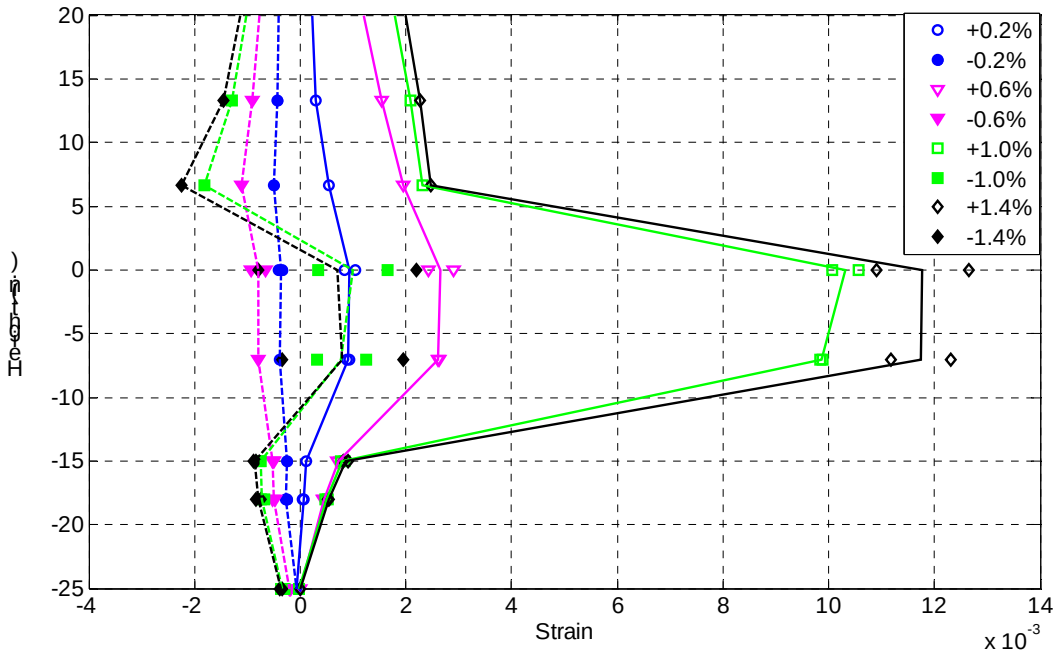

Figure 5-24. Specimen LB6-PT: strain profiles for Bar V00.

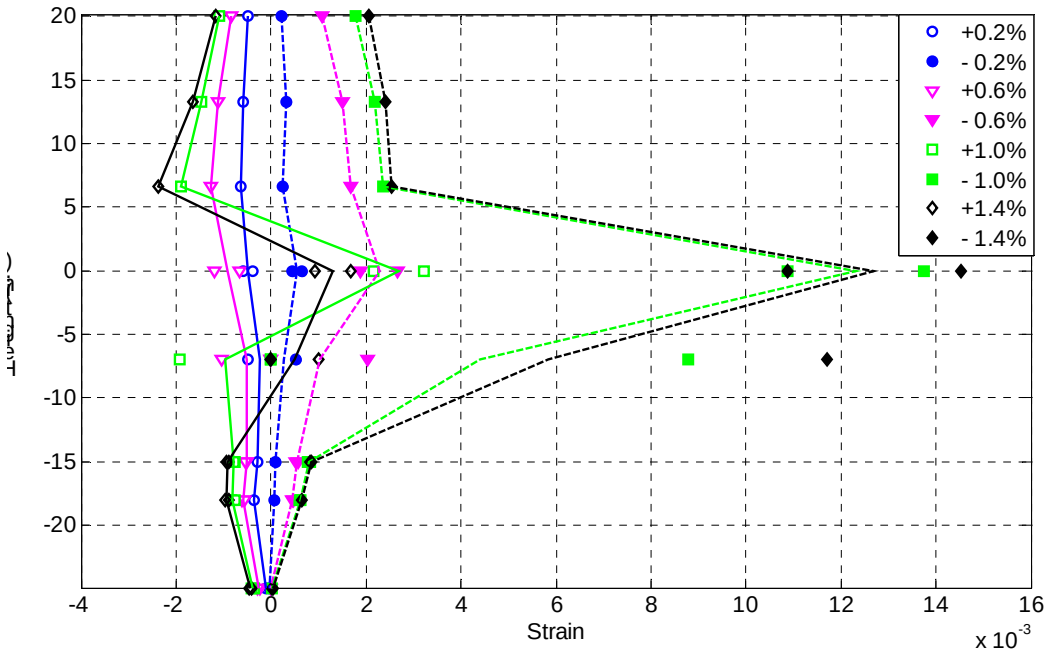

Figure 5-25. Specimen LB6-PT: strain profiles for bar V18.

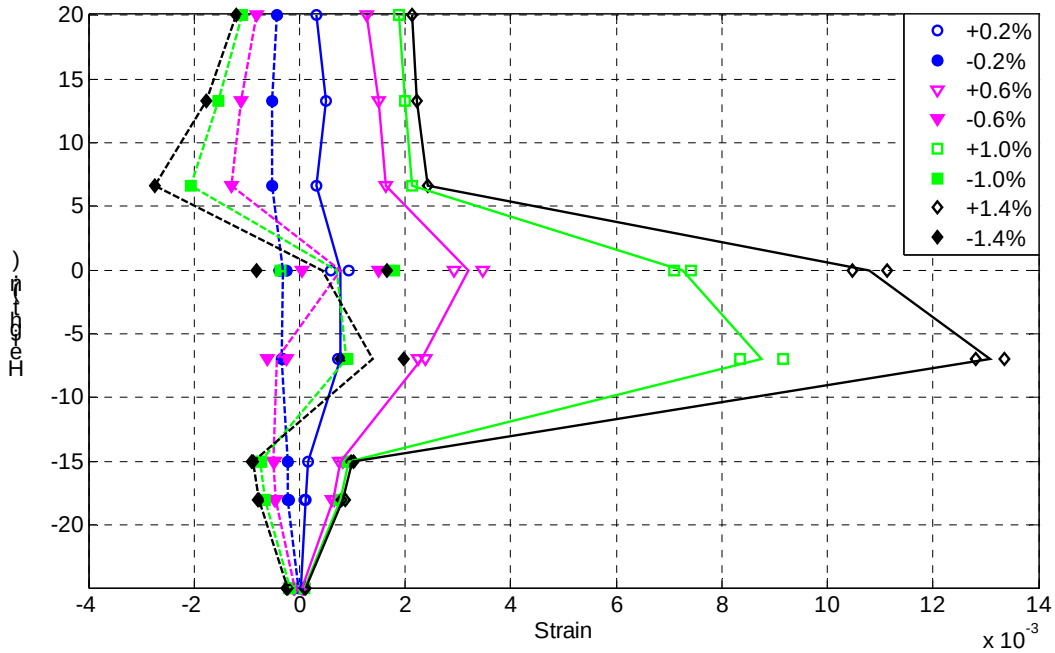

Figure 5-26. Specimen LB7-PT: strain profiles for Bar V00.

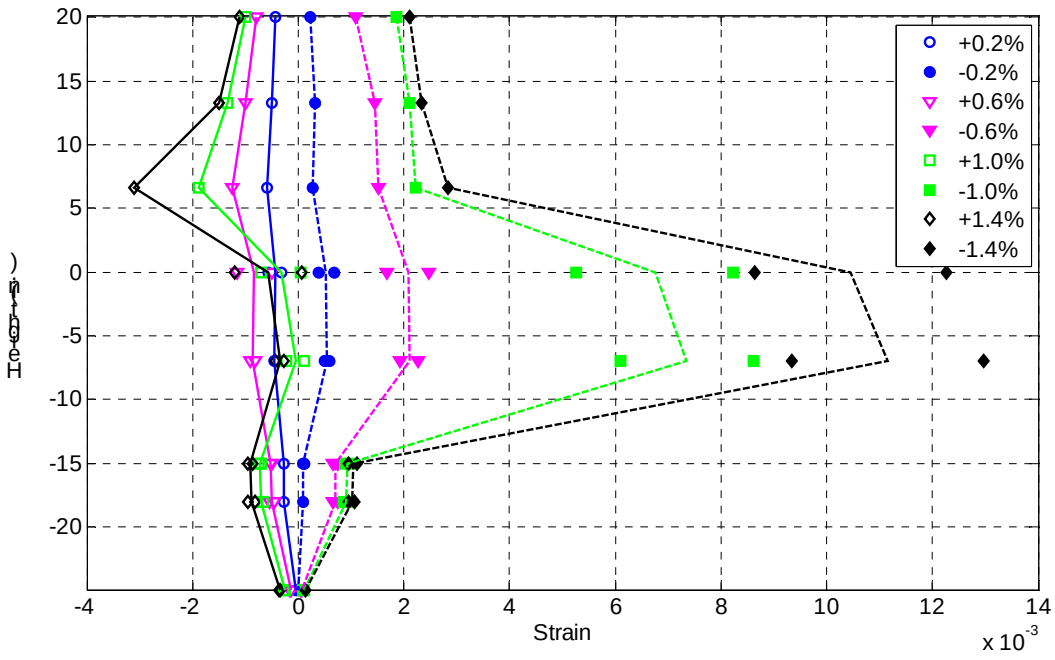

Figure 5-27. Specimen LB7-PT: strain profiles for Bar V18.

All four strain profiles were similar. At lower drift ratios (below 1.0 percent), all gauges on the north bar (V00) measured tensile strains when the column was displaced south and compressive strains when the column was displaced north (with the exception of the interface gauges on V00 in LB7-PT at -0.6 percent) and vice versa for the south bar (V18). All interface gauges and the gauges located 7 in. below the interface exceeded the yield strains of the bars between drift ratios of 0.4-0.6 percent, except for the gauge on bar V18 in LB6-PT at 7 in. down, as that gauge broke during casting of the concrete. After yield the tensile strains in all bars at the interface and in the debonded region increased greatly. When the column was next displaced in the other direction, the strains in the bars at those locations decreased but did not go into compression. This trend could possibly be due to the concrete crushing with pebbles and concrete rubble displacing, and thus preventing the longitudinal bars from returning.

In three of the four figures, the average strains over the interface are almost identical to the average strains 7 in. below the interface, in the debonded region. This suggests that the bars were in fact debonded in that region. The figure that does not show this is Figure 5-25; it shows the strain distributions for V18 in specimen LB6-PT that had

the broken gauge at that location. The strains decreased dramatically between the gauges located 7 in. below and the ones located 15 in. below the interface.

5.9.2 Bar Curvatures

The curvatures of bars V00 and V18 were calculated with Equation 5-6 by using the strain-gauge data from pairs of gauges that had been placed on the bars.

$$\varphi = \frac{\varepsilon_N - \varepsilon_S}{d_b} \qquad \textbf{5-6}$$

The curvature profiles of bars V00, for both LB6-PT and LB7-PT and V18 for LB7-PT, are presented in figures 5-28 through 5-30. As expected, little or no curvature was measured in the bars below the debonded region, but at the interface and in the debonded region, the bars did appear to bend.

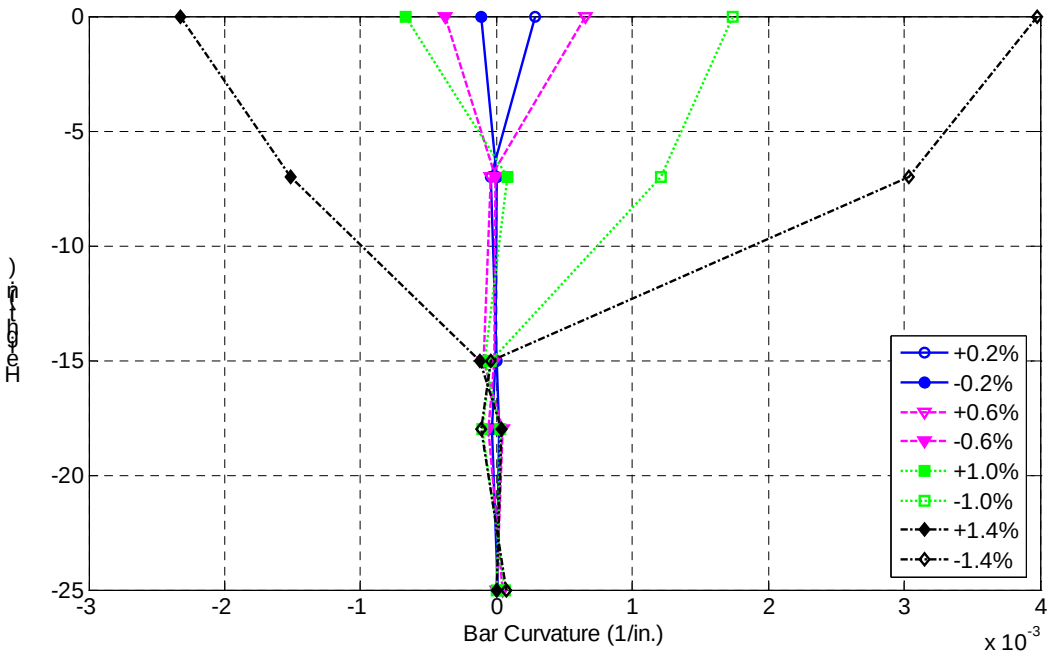

Figure 5-28. Specimen LB6-PT: curvature profile for Bar V00.

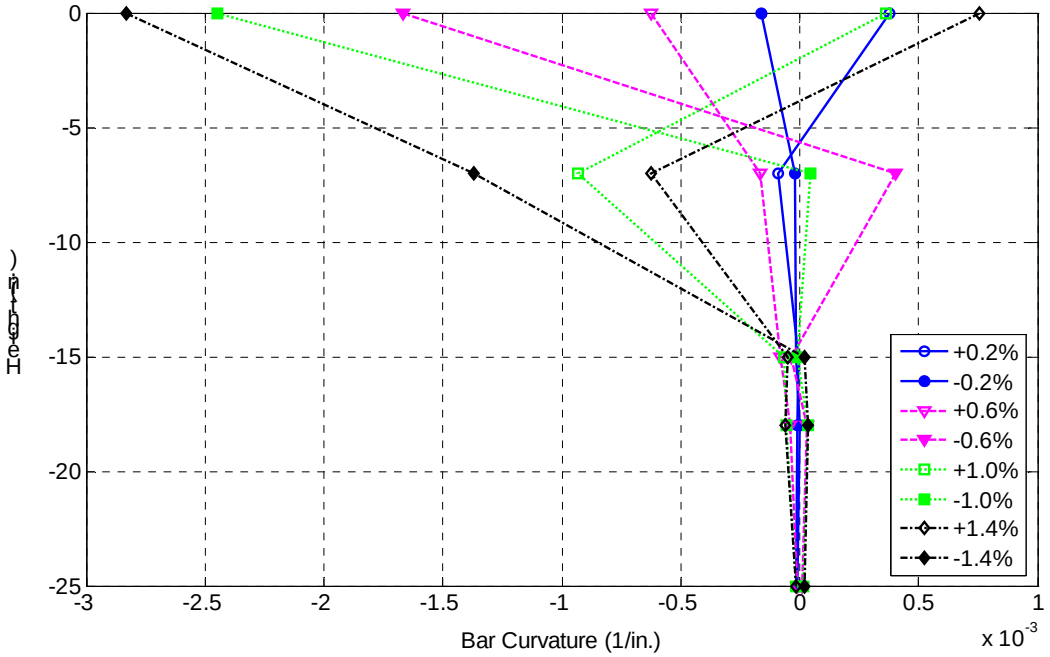

Figure 5-29. Specimen LB7-PT: curvature profile for Bar V00

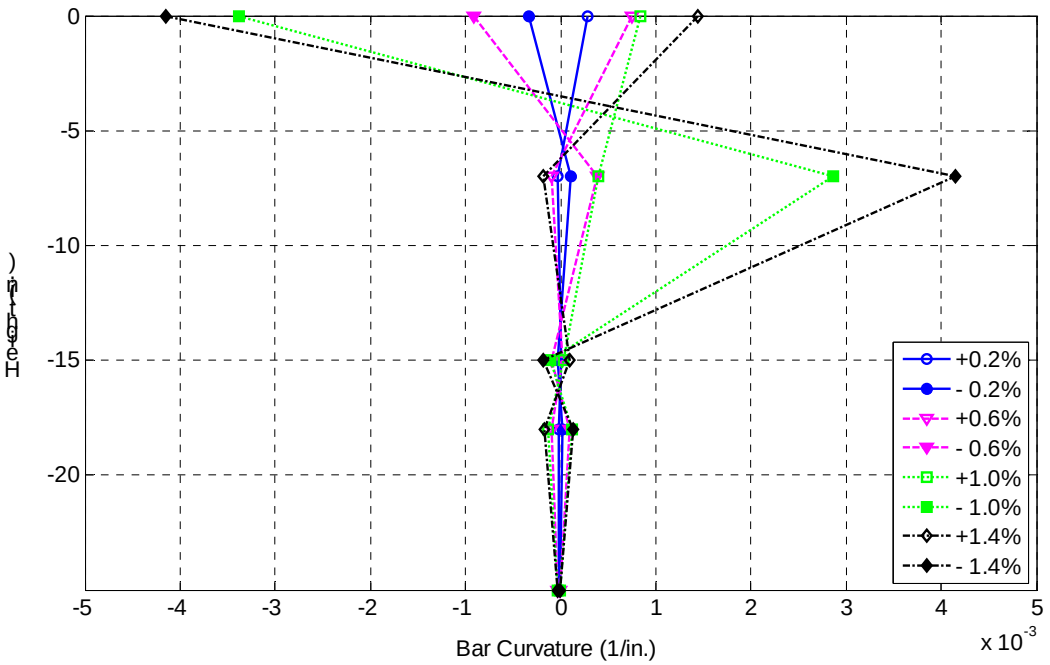

Figure 5-30. Specimen LB7-PT: curvature profile for Bar V18.

CHAPTER 6: DATA ANALYSIS

6.1 Strength Degradation

Figure 6-1 shows the envelope curves for the effective force vs. drift for all three specimens. The envelope curves for specimens LB7-PT and LB8-D1 are almost identical up to the maximum and minimum forces, which were reached at around 3 percent drift. The LB6-PT curve follows the other two curves up to a drift ratio of about 0.5 percent but then has lower positive and negative forces than either LB7-PT or LB8-D1. Figure 6-2 shows these envelope curves for the effective force normalized by the overall maximum force vs. drift for each specimen. Between drift ratios of about 2 percent and 7 percent, all three specimens lost strength at approximately the same rate.

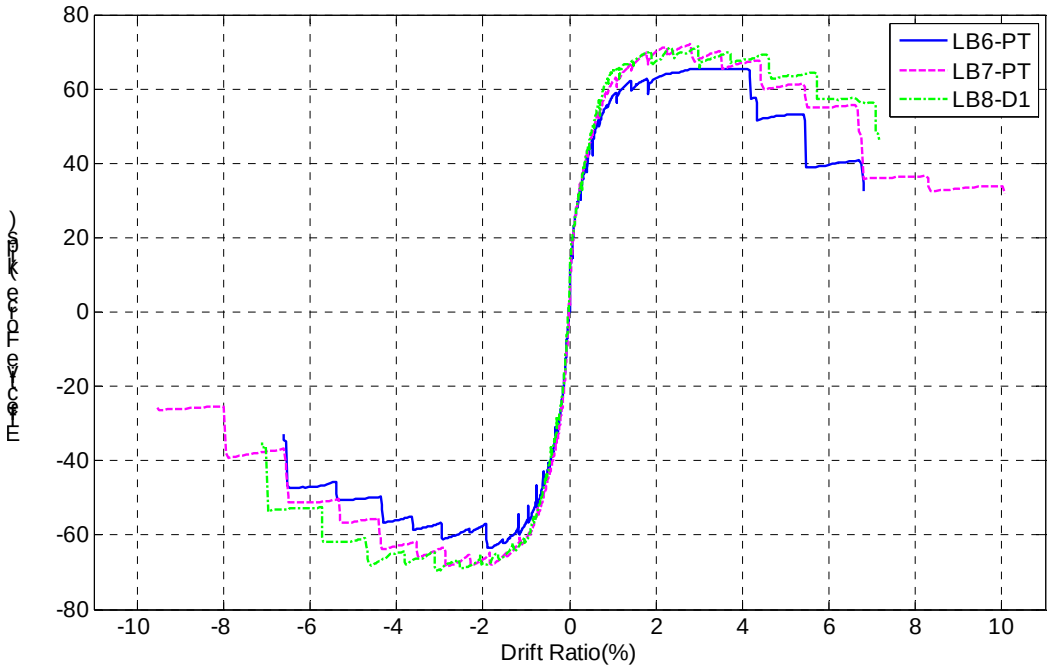

Figure 6-1. Comparison of effective-force vs. drift ratio.

LB6-PT started to lose strength at a drift ratio of about 2 percent, according to the negative portion of Figure 6-1. The positive portion of the plot for LB6-PT contains the unintended overloading at that drift level, and therefore it retained its strength until just

after 4 percent drift. A strength reduction of up to 80 percent of the peak strength is often used as an identification of member failure. This state was reached in specimen LB6-PT at a drift ratio of just over 4 percent.

Specimen LB7-PT started losing strength at a drift ratio of about 3 percent. This decrease is noticeable for both the positive and negative drifts. A strength reduction of up to 80 percent of the peak strength took place at a drift ratio of about 5 percent in the positive direction and 4 percent in the negative direction.

Overall, the three specimens lost strength at very comparable rates, with the two PT specimens losing strength slightly faster than did LB8-D1.

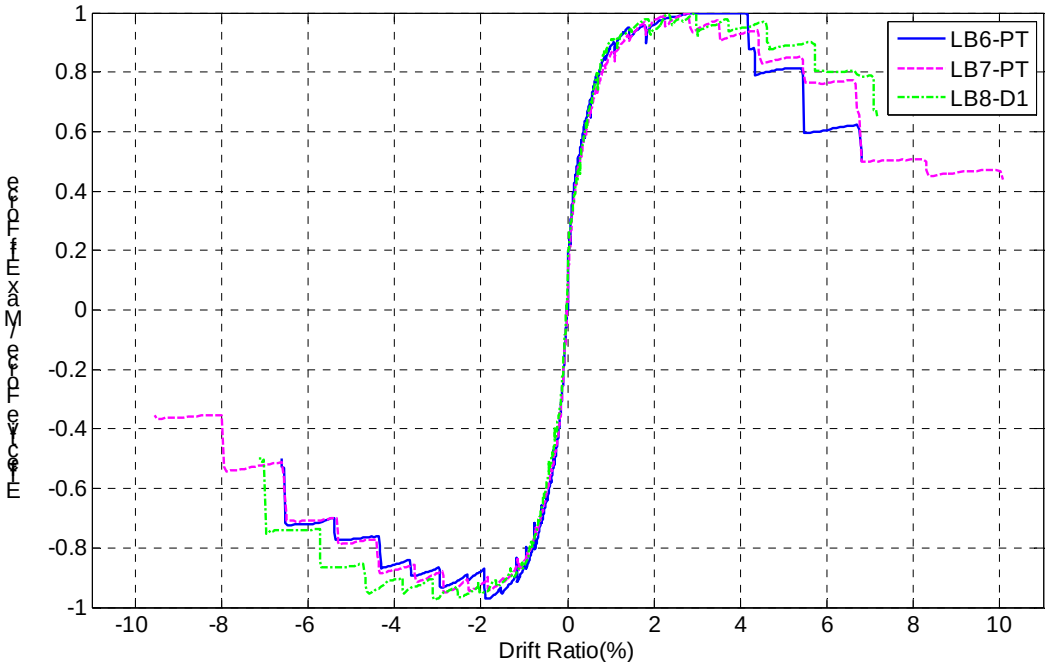

Figure 6-2. Normalized effective force vs. drift ratio.

6.2 Energy Dissipation

The energy dissipated during the tests was a measure of the effective damping during an earthquake. The energy dissipated during each cycle is equivalent to the area inside the force-displacement curve. It was calculated per cycle, and then the results for all cycles are added to find the cumulative energy dissipation. The energy per cycle was

calculated by using the trapezoidal integration procedure given in Equation 6-1, and it is demonstrated with Figure 6-3

$$E_{cycle} = \sum_i \frac{F_{i+1} + F_i}{2} \cdot \left(\Delta_{i+1} - \Delta_i\right) \qquad \textbf{6-1}$$

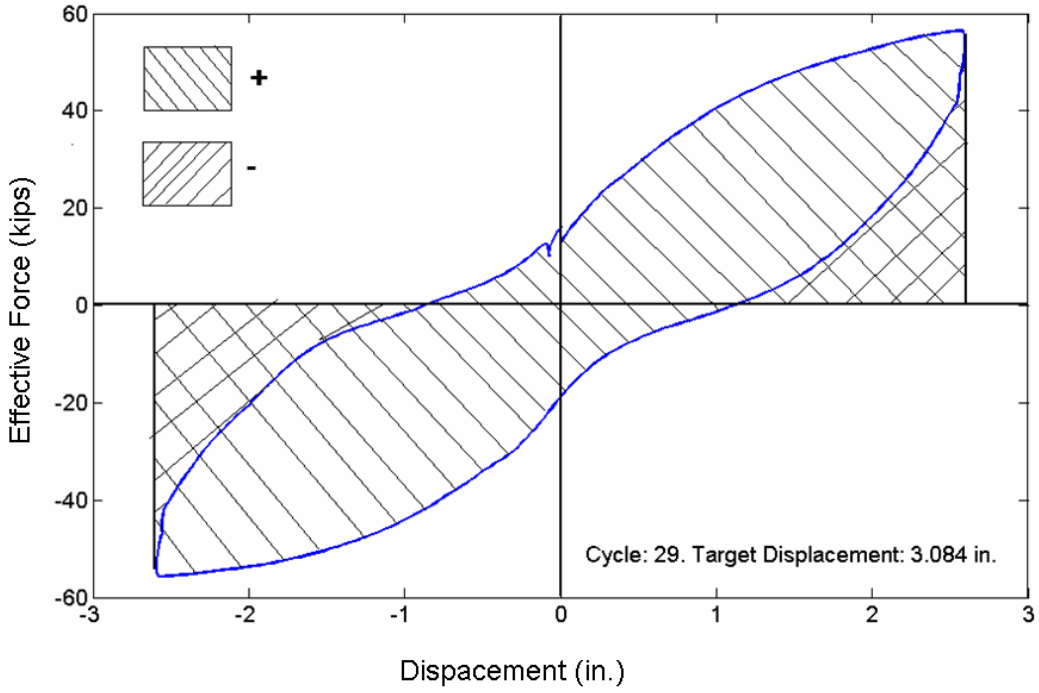

Figure 6-3. Example of energy dissipation calculations for one cycle.

The energy dissipation per cycle and the cumulative energy dissipation for the two PT specimens and LB8-D1 are presented in Figure 6-4.

The energy dissipation per cycle for all three specimens was the same up to a drift ratio of about 1.4 to 1.7 percent (Cycle 20-21); at this drift level, the hysteresis loops for the two PT specimens and LB8-D1 started to differ. As expected, LB7-PT dissipated less energy per cycle than LB8-D1 at those higher drift levels, and LB6-PT dissipated less energy than LB7-PT. Tests for both LB6-PT and LB8-D1 were terminated at a drift level of 6.5 percent (Cycle 34). Specimen LB7-PT reached a drift ratio of 10 percent (Cycle 37).

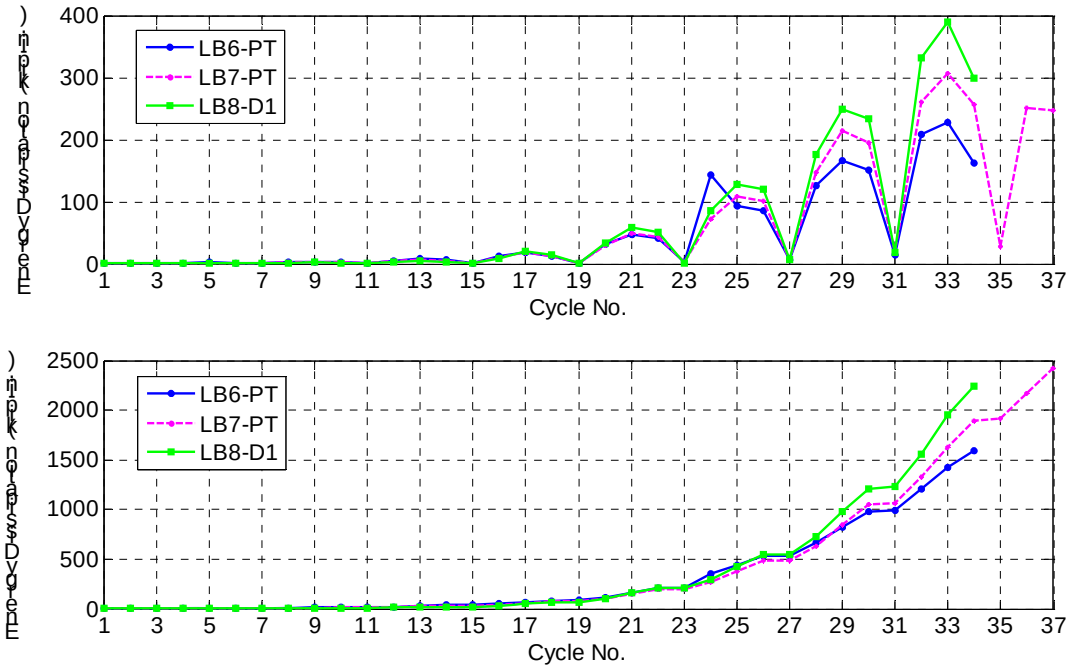

Figure 6-4. Above: energy dissipation per cycle. Below: cumulative energy dissipation.

Figure 6-5 shows energy normalized by the area of the rectangle defined by the overall maximum and minimum forces of the test, and the maximum and minimum displacement during the cycle being evaluated. This form provides a good basis for comparison of the later cycles in the tests (Cycle 17 and above). In the lower cycles, the deducted friction force had a big influence on the difference between tests. The peak displacement in a cycle also differed somewhat, which had a substantial effect on the ratio. The computed energy dissipation through Cycle 17 (peak drift ratio of 1.4 percent) of the tests must therefore be treated as unrepresentative of the true energy dissipation in that range. It was only about 2 to 4 percent of the total energy dissipation.

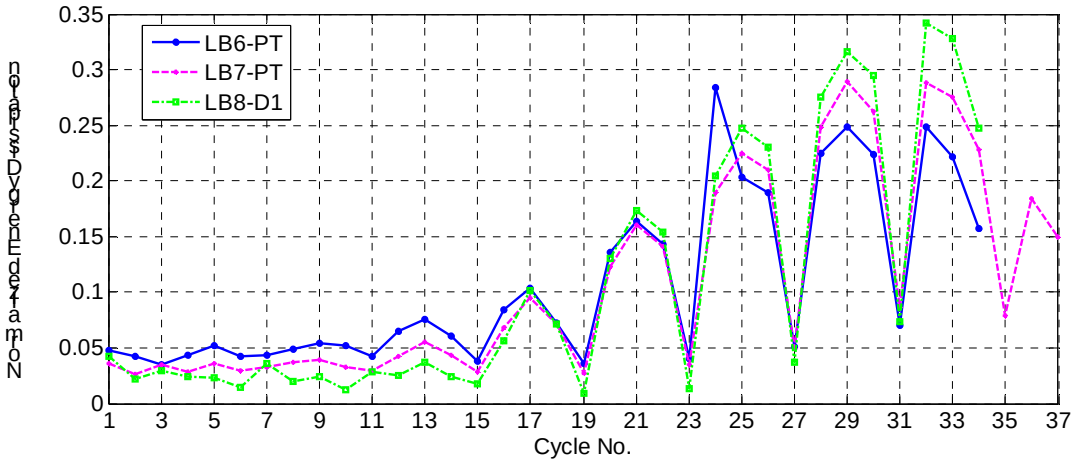

Figure 6-5. Normalized energy dissipation per cycle.

Figure 6-6 shows the energy dissipation of the PT specimens normalized with respect to that of Specimen LB8-D1, at only these larger cycles. It shows that LB7-PT dissipated about 85 percent of the energy of specimen LB8-D1. Specimen LB6-PT dissipated around 85 percent in Cycle 17 but dropped fairly linearly to about 55 percent in Cycle 34. The lower energy dissipation associated with Specimen LB6-PT is consistent with the fact that it contained relatively less mild steel. Tests for both LB8-PT and LB6-PT were terminated after Cycle 34, at which point both extreme longitudinal bars had fractured. Specimen LB7-PT's first longitudinal bar fractured during Cycle 35.

The big spike in the plot of LB6-PT at Cycle 24 is due to the previously mentioned unintended overload at the positive drift of that cycle. LB6-PT was cycled to an almost 70 percent higher drift level, in one direction, than were the other two specimens; therefore, the energy dissipation for LB6-PT for that cycle was much higher.

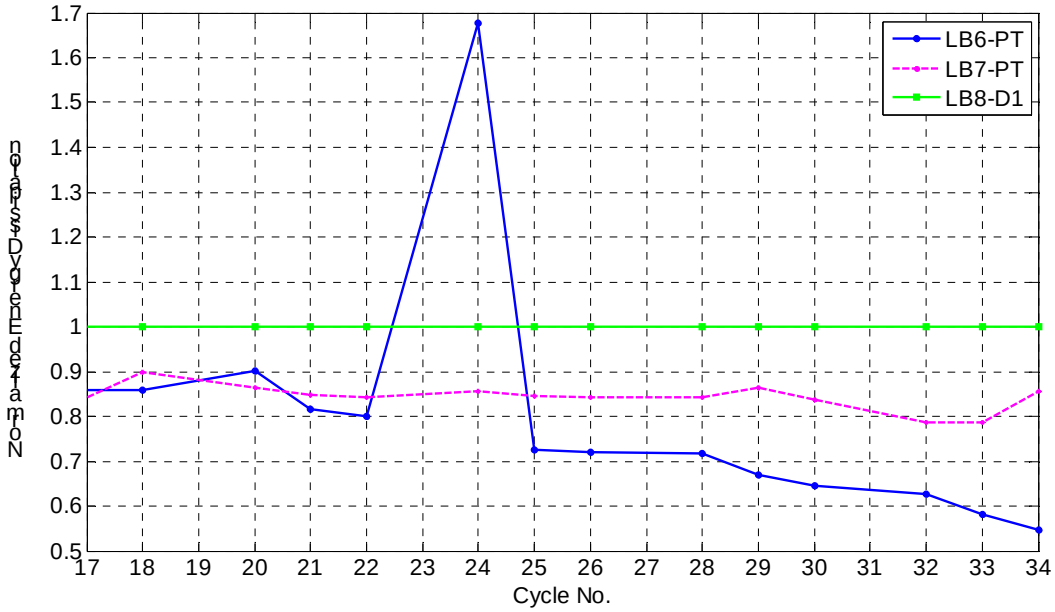

Figure 6-6. Normalized energy dissipation for cycles 17 through 34.

The equivalent viscous damping ratios are plotted against cycle number in Figure 6-7 for the three specimens. Here every fourth cycle of the displacement history is plotted, beginning with the first cycle. Each cycle plotted has an increase in displacement amplitude equal to 1.4 times that of the one before. The equivalent viscous damping is calculated by multiplying the energy dissipation, that has been normalized by the area of a rectangle circumscribing the loop, by $2/\pi$. As with the energy dissipation, the damping values through Cycle 17 should be treated as unrepresentative of the real damping properties. The two PT systems might be expected to show less damping than specimen LB8-D1 because the PT bar remained nearly elastic. This was indeed observed, but the differences in damping up to a drift ratio of 2 percent were small. In Figure 6-8 the same information regarding the equivalent viscous damping is plotted against the average peak drift ratio for the cycles mentioned above.

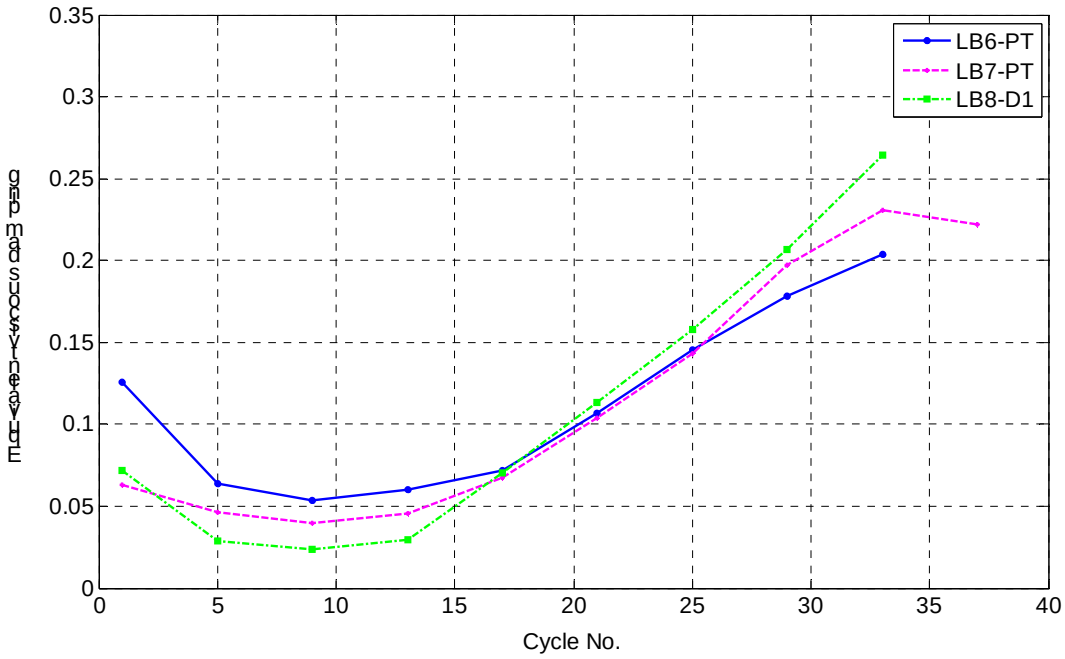

Figure 6-7. Comparison of the equivalent viscous damping coefficient per cycle.

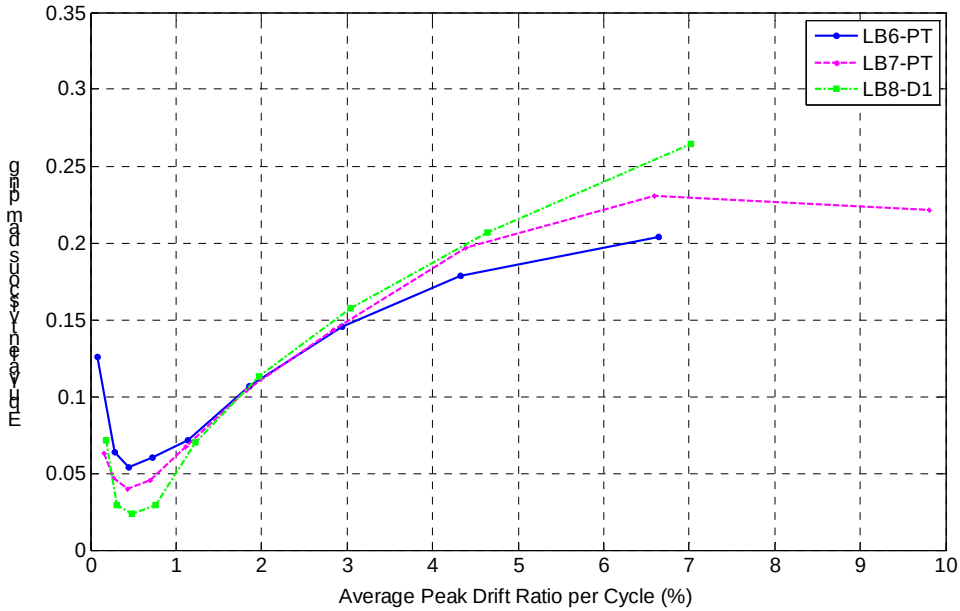

Figure 6-8. Equivalent viscous damping coefficients vs. drift ratio.

6.3 PT Bar Behavior

Section 5.8 discusses how the column lengthened as the tests progressed (figures 5-22 and 5-23). The measurements were obtained by taking the average displacements

recorded by the vertical "curvature" potentiometers on opposite sides of the column. The sum of theses averages gave a measurement of the elongation at the center of the columns. The fact that the column lengthened conflicts with the assumption that the PT bar force at zero drift was decreasing because of shortening of the column as a result of crushing of the concrete.

The other plausible hypothesis, that the PT bars were yielding, appears likely. To confirm this hypothesis, the measured forces in the PT bars were plotted against the axial lengthening of the columns, shown in figures 6-9 and 6-10. In both figures a noticeable change in slope of the plots is visible at 170 kips.

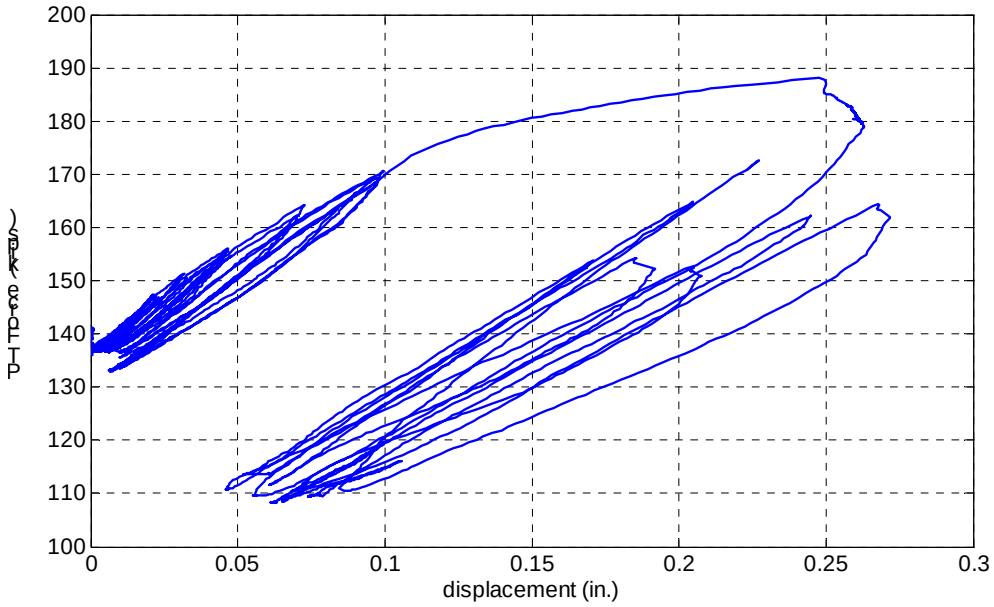

Figure 6-9. LB6-PT: PT force vs. column axial lengthening.

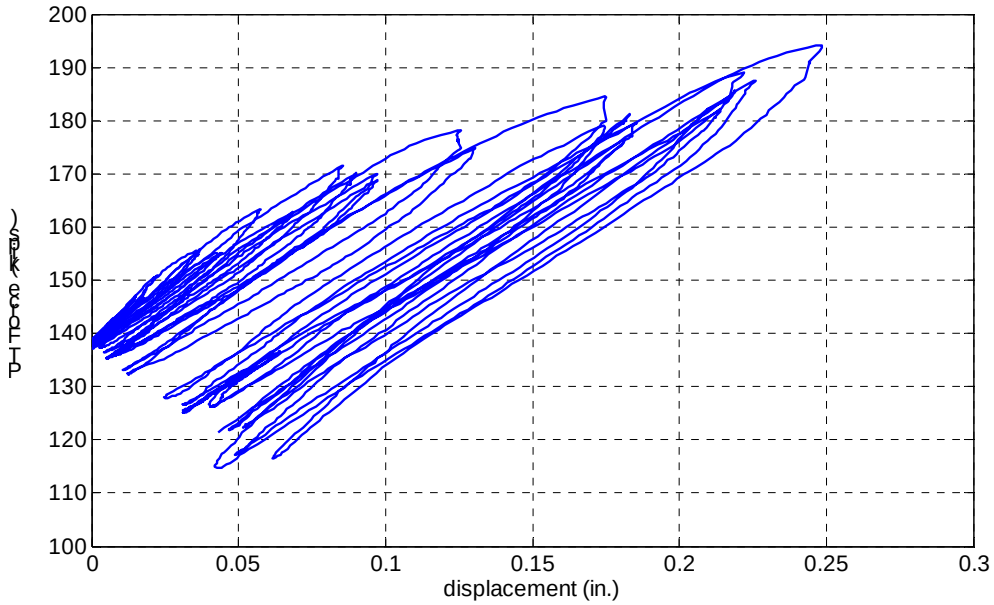

Figure 6-10. LB7-PT: PT force vs. column axial lengthening.

This information regarding the axial lengthening of the columns calculated from the specimen tests was compared with the data from the tension tests. Figures 6-11 and 6-12 show the stress-strain curves from both tests. For these plots, the measured force in the PT bars was divided by the nominal bar area, and the elongation of the specimen test was divided by the unbonded length. The elongation of the bar for the tension tests was divided by the gauge length.

The PT bars in the specimens had been tensioned prior to testing and, therefore, had some initial elongation. This initial elongation had not been measured; therefore, for comparison, the specimen data were offset horizontally so that that initial data matched up with the tension test data of the unused bar. As can be seen in Figure 6-11, both data sets match well. Figure 6-12 also had tension test data from the used LB7-PT bar; it was offset horizontally by the horizontal length of the specimen data.

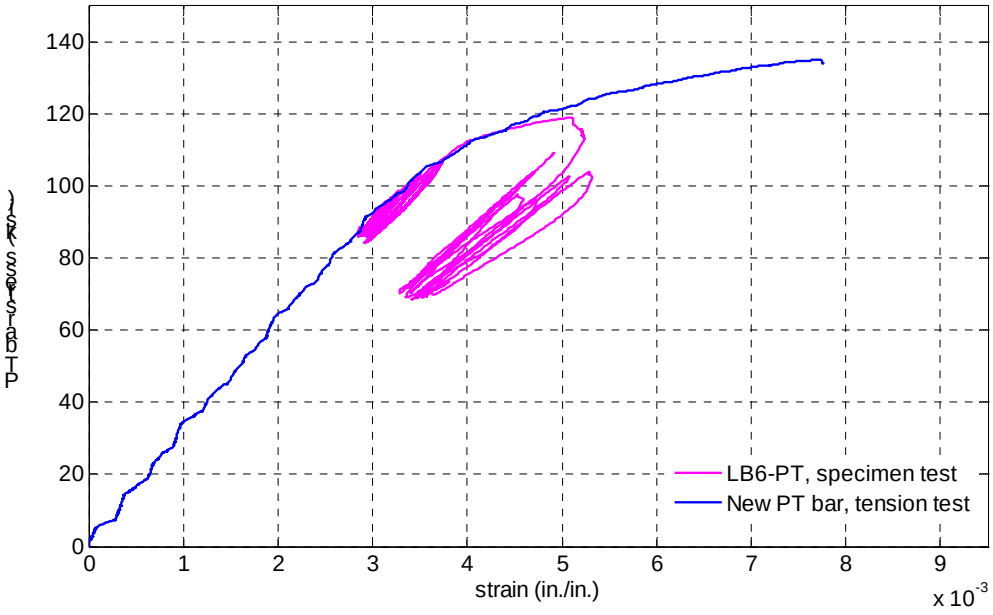

Figure 6-11. Comparison of tension tests and Specimen LB6-PT bar stress vs. strain from column test.

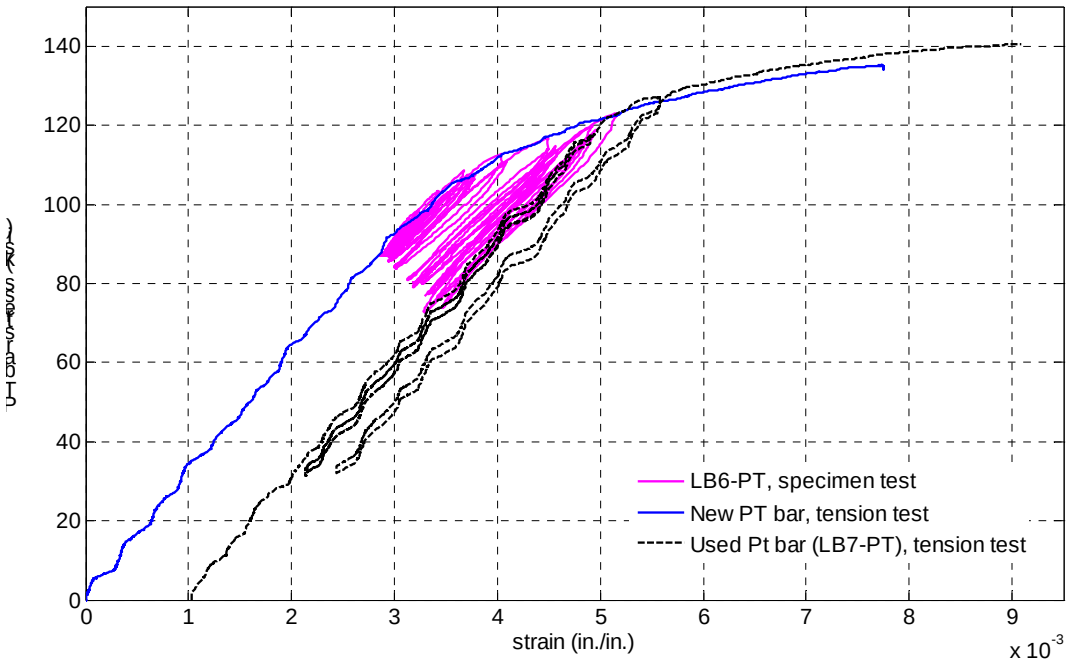

Figure 6-12. Comparison of tension tests and Specimen LB7-PT bar stress vs. strain from column test.

6.4 Column Residual Displacements

The unbonded post-tensioning had been added to the large-bar system to supply a force that would return the column to vertical, or close to vertical, after a seismic event.

As the tests were displacement-controlled, residual displacements could not be measured directly. To provide an indirect measurement of the different residual displacements between test specimens, the displacements at zero lateral force were extracted. Because the hysteresis loops were not exactly centered about the origin, the residual displacement for a given load cycle was determined as half the distance from the first zero-force displacement point to the second one. It was then normalized by half the distance between the peak displacement points of that cycle. These terms are shown in Figure 6-13 for explanation.

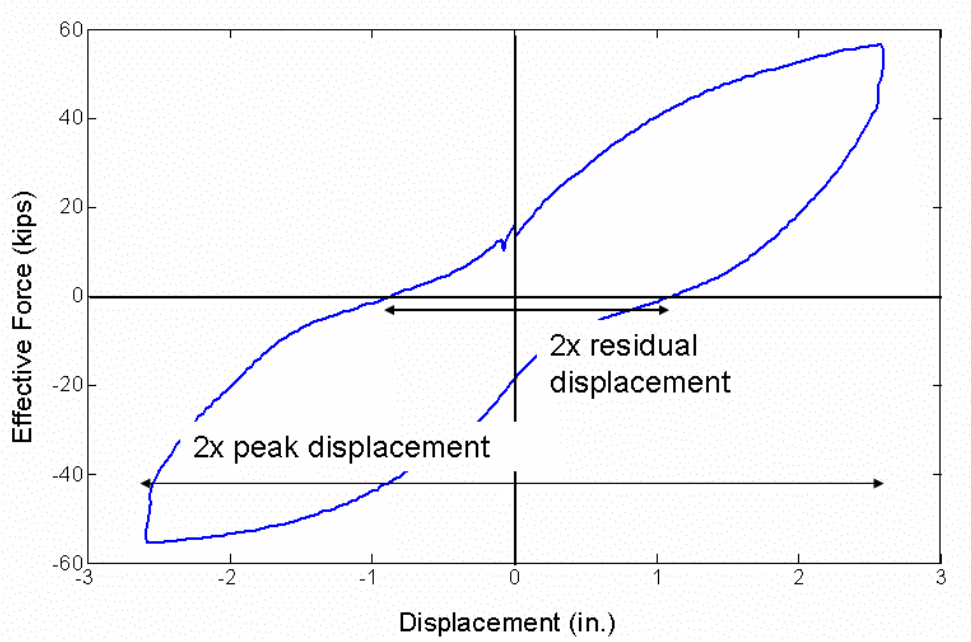

Figure 6-13. Explanation of terms used to calculate the residual displacements.

Figure 6-14 presents the normalized residual displacement for specimens LB6-PT, LB7-PT, and LB8-D1 plotted against the peak drift ratio. In a shaking table test or a real earthquake, the column would be subjected to a ground motion. Depending on the ground motion, the forces applied might have some origin-oriented component, which would, along with the PT bar force, help re-center the column. Also, earthquakes tend to hit a maximum acceleration fairly early, with the accelerations decreasing thereafter. In a

displacement-controlled, pseudo-static test there is no such assistance, so the values shown in Figure 6-14 can be viewed as worst case values.

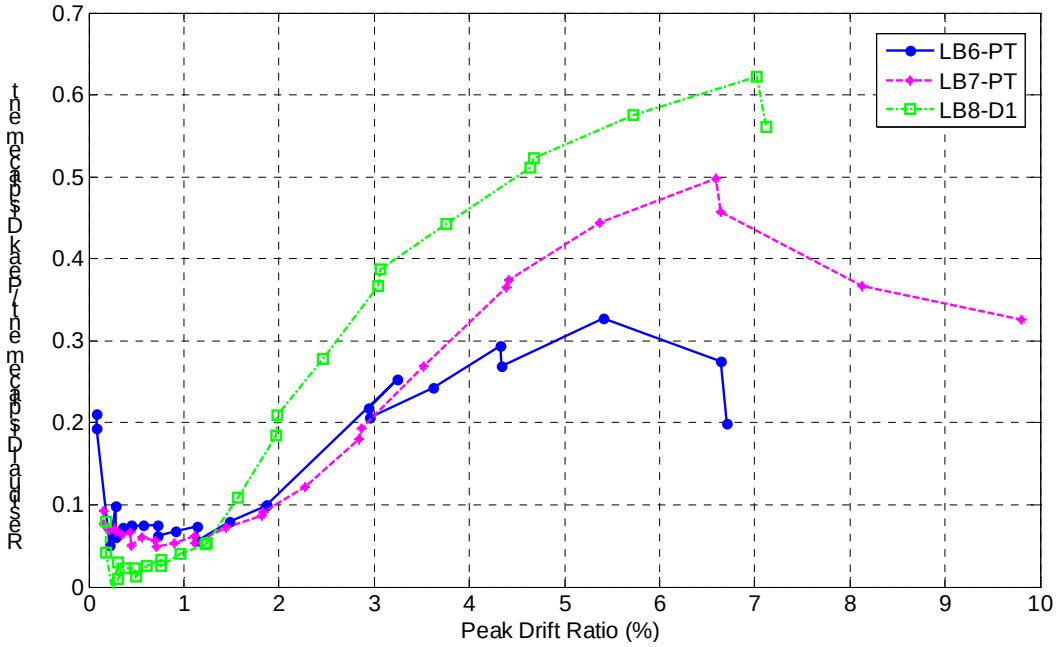

Figure 6-14. Comparison of the normalized residual displacement vs. peak drift ratio.

For peak drift ratios of greater than 1.4 percent, the ranking of the residual displacements for the three specimens was as expected: the specimen with no post-tensioning, LB8-D1, had the largest residual displacements, and the two PT specimens had lower residual displacements. For drifts of up to about 3 percent, the residual displacements of the two PT specimens were almost the same. At higher drift levels the residual displacements of LB6-PT, the specimen with the larger re-centering ratio, were smaller than those of LB7-PT. This behavior is consistent with the concept of the re-centering ratio.

At drifts of lower than 1.4 percent the post-tensioning appeared to inhibit, rather than help, the re-centering. However the data in that region were strongly affected by the correction for friction in the test machine head and should not be used to draw conclusions about the behavior. Because specimen LB8-D1 had twice the external axial load of that imposed on the other two columns, it experienced approximately twice the friction force, which was therefore subtracted in the data processing. Uncertainties in

modeling the friction mean that the corrected force data were least accurate for the smaller cycles.

The external axial load on the PT specimens was half that of the axial load on the non-post-tensioned one, LB8-D1. This decision was made early on in the project to keep the total moment strength of all specimens similar and thus comparable. Because of this difference in external axial load, the effect of the PT force, and thus the re-centering ratio, on the residual displacements (see Figure 6-14) was not as great as one might expect it to be for two similar systems with the same external axial load, one with no PT and the other with it. The friction correction made and discussed in Section 5.2 also affected the outcome of the residual displacements, as the friction force deducted was a multiple of the coefficient of friction, which was kept unchanged, and the externally applied axial load.

The slope of the force-displacement curve at zero force was quite small, at least at larger peak drift ratios. Consequently, a small shift in force would lead to a large change in the displacement at which the curve crossed the zero force axis, which is interpreted here as the residual displacement. To illustrate the sensitivity of the residual displacement calculations, the slope of the force-displacement curve where it crossed the zero force axis was plotted against the peak displacements for that cycle. Figure 6-15 shows this relationship, with the slope normalized by the slope of the cycle where the first column bar yielded.

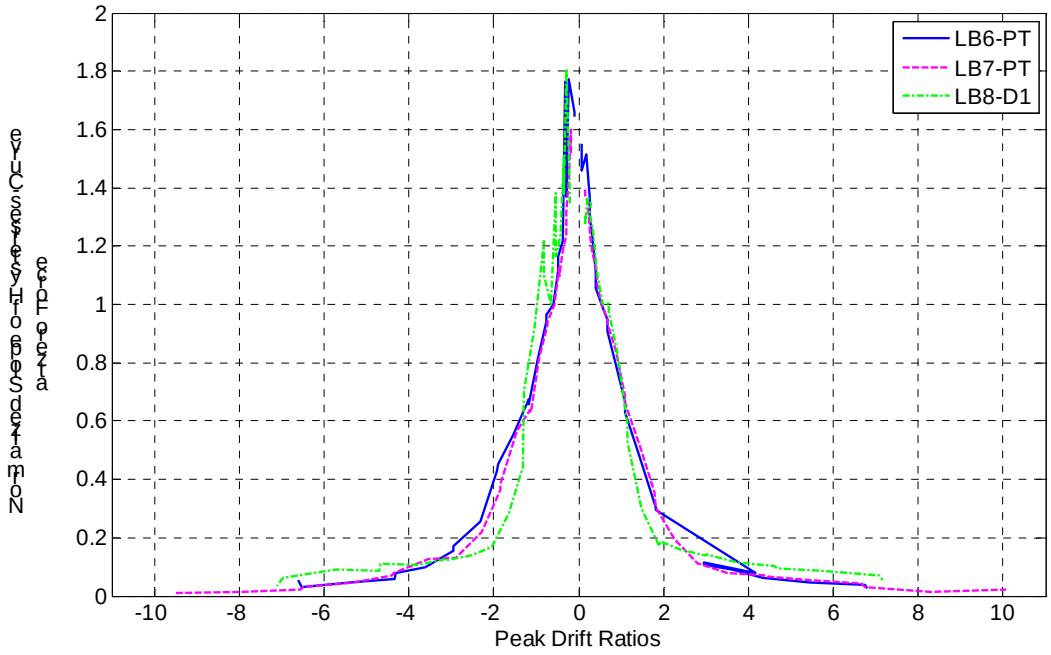

Figure 6-15. Normalized hysteresis curve slopes at zero force vs. drift ratio.

The slope was determined as the slope of a best fit line through a number of points on the hysteresis curve above and below zero-force. Because of a constant loading rate and increasing peak displacements, fewer points were needed to capture the correct slope at larger drift levels than at smaller ones.

The changes in slope for both PT specimens are nearly identical. It is interesting to note that the slope for LB8-D1 is less than that of both LB7-PT and LB6-PT in the drift ratio interval of 1.2 to 3 percent. At a drift ratio of 1.7 percent, the re-centering ability of the PT specimens becomes noticeable in the hysteretic performances, and the geometry of the hysteresis loops changes, which probably contributes to the difference in slope. Around the origin, the PT-bar specimens both have a "neck" region that is longer and narrower than that of LB8-D1. This difference in the hysteresis loops is demonstrated in Figure 6-16.

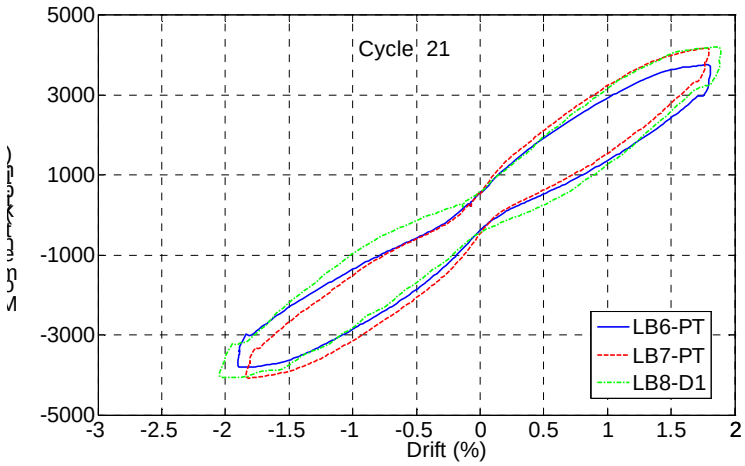

Figure 6-16. Comparison of hysteresis loop shapes for a cycle.

6.5 Effectiveness of Re-Centering Ratio at Predicting Residual Displacements

The two specimens tested, LB6-PT and LB7-PT, were built with different ratios of prestressing steel to mild steel. The ratio was higher in LB6-PT than in LB7-PT, and consequently, LB6-PT had a higher nominal re-centering ratio of 1.6. Specimen LB7-PT had a re-centering ratio of 1.2. These two specimens were then compared to LB8-D1, which had no prestress and a re-centering ratio of 0.9.

During design the nominal yield strength of the mild steel, 60 ksi, was used for calculation of the re-centering ratios. Tensile tests provided actual yield strengths that were just above 60 ksi for the #7 bars and around 70 ksi for the #6 bars. This meant that the calculated re-centering ratio for specimen LB6-PT decreased to 1.4, and therefore, the difference in re-centering capabilities between the PT specimens was expected to be less than intended.

The re-centering ratio was calculated by using Equation 2-4 and the actual yield strength of the bars. Calculating the stress in the mild steel throughout the displacement history would have required a cyclic stress-strain relationship for the mild steel, which was not readily available. Therefore, the monotonic yield strength of the bars was used. The PT bar force and the external axial load used in Equation 2-4 were actual values measured during the test.

Throughout the test, the re-centering ratio increased with increasing drift from zero to peak, with the re-centering ratio at zero-drift decreasing as the specimen went through higher cycles, following the PT bar force decrease described earlier.

Figure 6-17 shows the re-centering ratio, at the time the specimens passed through zero displacement, plotted against the maximum/minimum drift the specimen had seen thus far during the test. Because the re-centering ratio is directly related to the PT bar force, it stays fairly constant out to a drift ratio of 2 percent and then starts decreasing because the PT bar started to yield at that drift.

Figure 6-18 shows the re-centering ratio, at the time the specimens experienced zero lateral force, plotted against the maximum/minimum drift the specimen had seen thus far during the test. The re-centering ratio calculated for the latter provides a means of comparison with the residual displacement calculations.

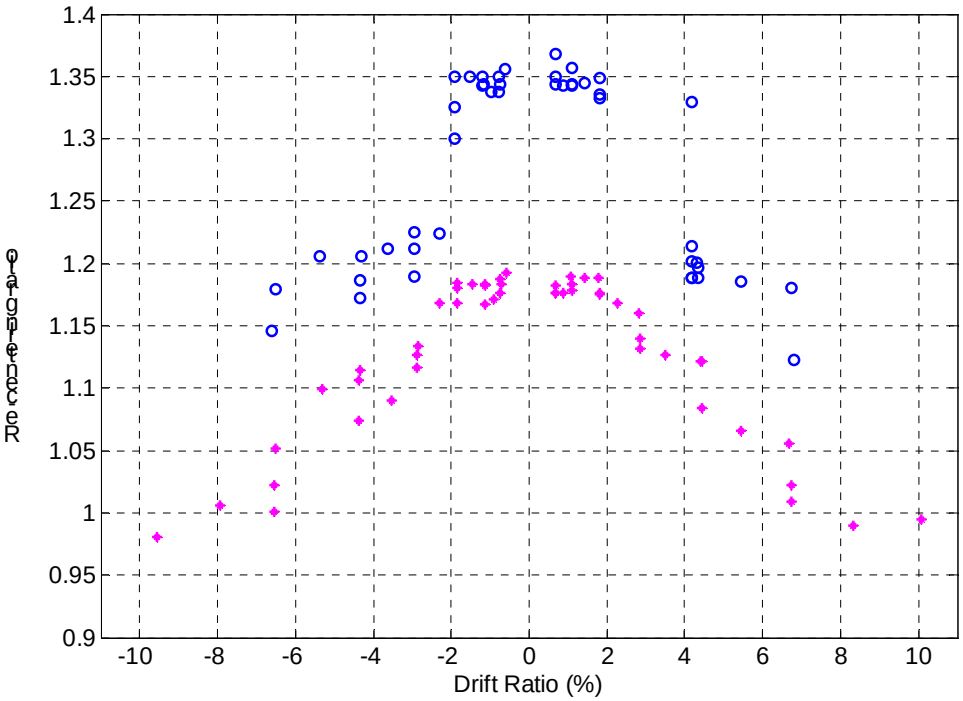

Figure 6-17. Re-centering ratio at zero drift vs. peak drift.

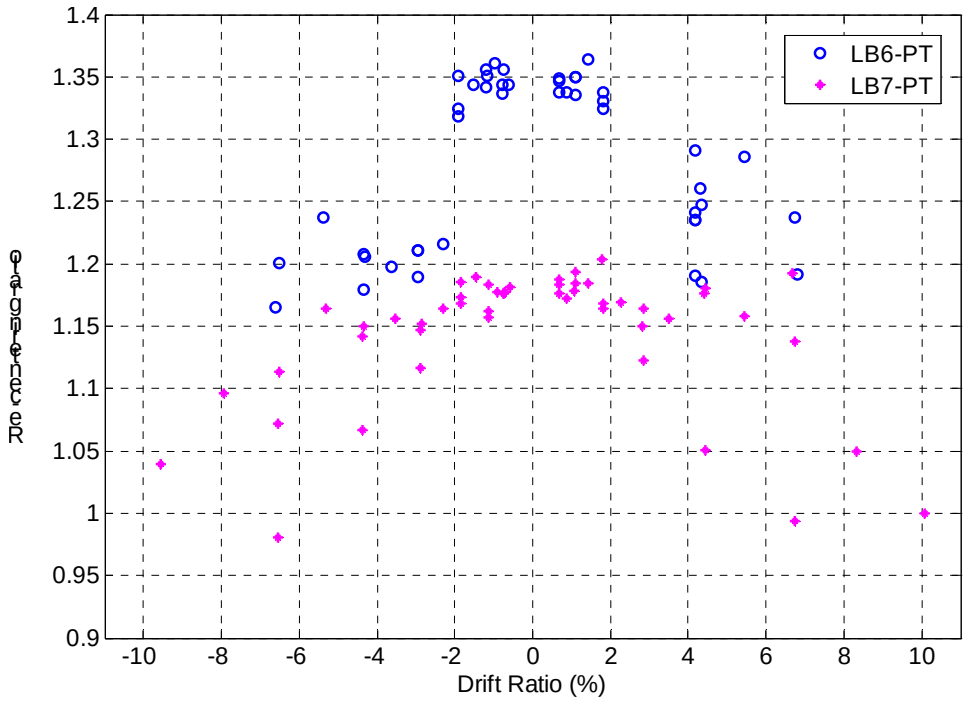

Figure 6-18. Re-centering ratio at zero lateral force vs. peak drift.

Figure 6-19 illustrates the relationship between the recorded residual displacements and the re-centering ratios (which were calculated as described above) at zero lateral force. The residual displacements calculated for each cycle were, in a sense, average values because the hysteresis loops were not exactly centered about the origin. The residual displacement calculations are presented in Section 6.4. For the re-centering ratios, two values were calculated at zero force for each cycle, and the values plotted in Figure 6-19 are the averages of those two values.

Each line on the plot is made up of three points, one from each specimen. For each line, Specimen LB6-PT always has the highest re-centering ratio and LB8-D1 always has the lowest one. The re-centering ratio for LB8-D1 calculated with the yield strength acquired from tension testing and the actual applied external axial force during the test turned out to be somewhat lower than the one calculated with nominal values because the yield strength of the bars was higher than the nominal strength, and the applied axial load was a little lower than the target load. The lines correspond to cycles 20 through 34 (excluding the small cycles) of the displacement history. The drift ratios used in the figure were target drift ratios for those cycles; the actual drift ratios were a bit smaller and varied somewhat between tests.

The large residual displacement for LB6-PT at the target drift ratio of 2.97 percent is due to the unintended overloading mentioned previously.

At the lower drift ratios the residual displacements for all three specimens are small, and the post-tensioning appears to have had no effect. As the drift ratios increase, a definite negative correlation can be seen between re-centering ratio and residual drift. This supports the hypothesis that the re-centering ratio is an indication of residual drift. However, the number of test specimens was too small to develop a reliable quantitative relationship between the two parameters.

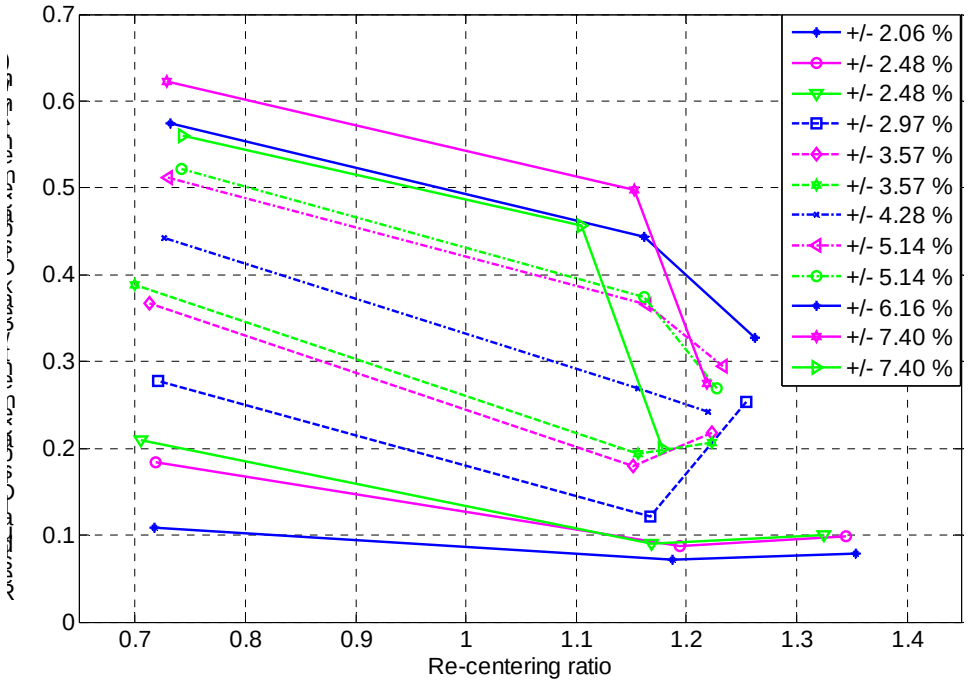

Figure 6-19. Residual displacement vs. re-centering ratio.

6.6 Debonding of Mild Steel Reinforcing Bars

In both PT specimens, all of the large bars were debonded from the concrete, from the interface down 8 in. into the cap beam by using method D1 described in Section 3.2.2. This was done to decrease the strain concentration at the interface, where most of the rotation due to the applied lateral load was expected to take place.

The total effective debonded length was calculated by using information supplied by the two interface potentiometers and the data from the interface strain gauges on bars V00 and V18. It was computed as:

$$L_{u,eff} = \Delta / \varepsilon \qquad \textbf{6-2}$$

where Δ is the elongation of the bar and ε is the average strain at the interface measured by the strain gauges. The strain gauges provided reliable data up to a drift ratio of 1.4 percent, so this was also the range of the effective debonded length calculations.

The calculations were undertaken to estimate the additional debonded length, and to gain insight into the nature and rate of progressive debonding. The values calculated for the effective debonded length before the bars yielded were larger than expected, but they dropped fairly suddenly after yield, sometimes to values below the deliberately debonded length. The scatter in the calculated lengths was quite large. This made any conclusions about the debonded length or the bond of the bars impossible. More detailed discussion of the effective debonded length can be found in Appendix D. The primary difficulties were associated with the fact that the measured strain was a local value, whereas an average value was needed. Under elastic conditions, the strain concentration at the gauge is likely to be small. However, grinding the bar to apply the gauge introduces a strain concentration that becomes significant when the bar first yields. Equation 6-2 then gives a lower bound to $L_{u,eff}$.

6.7 Analysis of Curvatures of Mild Steel Reinforcing Bars

The bar curvatures were presented in figures 5-28 through 5-30. In this section an attempt is made to better identify the nature of this phenomenon in the sleeved portion of the bars. Below that region, little or no curvature was observed.

Because data were available from only two sets of gauges per bar (one pair at the interface and one pair at the bottom of the sleeved region), constructing a complete deflected shape for the bars was not possible. However, several trends could still be identified:

- As the column displacement increased in magnitude, so did the bar curvature.
- The magnitude of the curvature was greater when the bar was in tension than in compression on the same cycle.
- Generally, a positive displacement resulted in a positive curvature at the interface and vise versa. At least one exception to this trend was found in all but one bar. They are discussed below.

- The curvatures of the bars at 7 in. below the interface could have the same sign as the interface curvature, the opposite sign, or be almost zero with no pattern observed.

There were a few exceptions to the curvature vs. displacement direction relationship at the interface. In bars V00 of both specimens and bar V18 of Specimen LB6-PT the curvature sign did not change with the change in loading direction. In Specimen LB6-PT bar V00 had a small negative curvature at a drift ratio of -0.6 percent. The next observed drift ratio was 0.8 percent, at which time the curvature was still negative and larger in absolute magnitude. The curvature did not change signs until at -1.0 percent drift, and from then on it had a sign opposite to that of the loading direction. A similar phenomenon was observed for bar V00 in Specimen LB7-PT and bar V18 in Specimen LB6-PT; changing from -0.4 percent to 0.6 percent and from -0.6 percent to 0.8 percent drift, respectively, the curvatures at the interface stayed negative. This took place, in all cases, just after both interface gauges on the bar had yielded in tension, so it is possible that a change in curvature was at that point more easily made higher up the bar, but gauges were not placed there on both sides of the bar, so the curvature there could not be calculated. Bar V18 in specimen LB7-PT was the only one that did not demonstrate this behavior. After a drift ratio of 0.6 percent to 1.0 percent the bars always had a net tensile strain, even on the compression side. Schematics showing the bar curvatures can be found in Appendix E.

CHAPTER 7: COMPARISON WITH PERFORMANCE MODELS

7.1 Damage Progression Models

Damage models developed by Berry and Eberhard (2003a, 2003b, and 2005) were used to predict the occurrences of cover spalling, bar buckling, and bar fracture. These values were then compared with measured values from the tests. Berry and Eberhard gave the following equations for predicting the drift ratio at which spirally reinforced columns reach the three damage states:

Spalling:
$$\frac{\Delta_{sp}^{calc}}{L}(\%) = 1.6\left(1-\frac{P}{A_g f_c'}\right)\left(1+\frac{L}{10D}\right) \quad \textbf{7-1}$$

Bar Buckling:
$$\frac{\Delta_{bb}^{calc}}{L}(\%) = 3.25\left(1+150\rho_{eff}\frac{d_b}{D}\right)\left(1-\frac{P}{A_g f_c'}\right)\left(1+\frac{L}{10D}\right) \quad \textbf{7-2}$$

Bar Fracture:
$$\frac{\Delta_{bf}^{calc}}{L}(\%) = 3.5\left(1+150\rho_{eff}\frac{d_b}{D}\right)\left(1-\frac{P}{A_g f_c'}\right)\left(1+\frac{L}{10D}\right) \quad \textbf{7-3}$$

where P is the applied axial load; L is the distance to the point of contraflexure; D is the column diameter; A_g is the gross area of the cross section; f'_c is the concrete compressive strength; and ρ_{eff} is $\rho_s f_{ys}/f'_c$, where ρ_s is the volumetric ratio of transverse reinforcement and f_{ys} is the yield stress of the transverse reinforcement. Berry and Eberhard's database contained no tests with prestressed columns, so equations **7-1** through **7-3** were calibrated by using the external load for P. However the **value of *P* used here was the axial load plus prestress.**

Figure 7-1 compare predicted and observed drift ratios for the three damage states for specimens LB6-PT and LB7-PT by using the initial prestress force (force in the PT bar at the start of testing). This resulted in a total axial load of 260 kips for LB6-PT and 261 kips for LB7-PT. For both columns, the damage model overestimated the drift ratios for spalling and bar buckling by an average of 14 percent, with the overestimation ranging from 0 percent to 29 percent. The drift ratios for bar fracture, on the other hand, were underestimated by about 19 percent.

Table 7-1. Comparison of damage model predictions and observed occurrences (using initial PT force).

	Drift ratio at onset of spalling(%)			Drift ratio at onset of bar buckling (%)			Drift ratio at the onset of bar fracture (%)		
Specimen	Pred.	Obs.	Pred./ Obs.	Pred.	Obs.	Pred./ Obs.	Pred.	Obs.	Pred./ Obs.
LB6-PT	1.82	1.41	1.29	4.97	4.45	1.12	5.35	6.74	0.79
LB7-PT	1.82	1.81	1.00	5.17	4.32	1.20	5.57	6.75	0.82
Mean	1.82	1.61	1.13	5.07	4.39	1.15	5.46	6.75	0.81

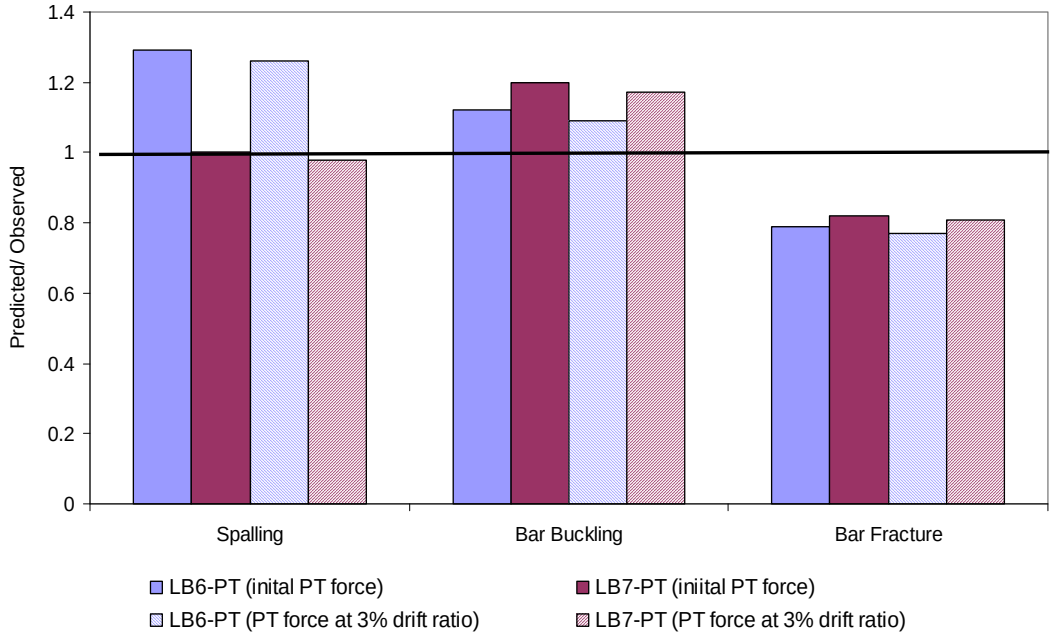

Figure 7-1. Comparison of damage model predictions and observed occurrences

The damage calculations were repeated by using the prestress force at a drift ratio of 3 percent. This resulted in a total axial force of 302 kips for LB6-PT and 305 kips for LB7-PT. Results for these calculations are presented in Table 7-2 and Figure 7-1. With the increase of total axial load, all the predicted drift ratios decreased slightly from their values calculated for the initial prestress force. The onset of spalling and bar buckling was now overestimated by an average of 12.5 percent, and the drift ratio at bar fracture was underestimated by 21 percent.

Table 7-2. Comparison of damage model predictions and observed occurrences (using PT force at 3 percent drift ratio).

	Drift ratio at onset of spalling(%)			Drift ratio at onset of bar buckling (%)			Drift ratio at the onset of bar fracture (%)		
Specimen	Pred.	Obs.	Pred./ Obs.	Pred.	Obs.	Pred./ Obs.	Pred.	Obs.	Pred./ Obs.
LB6-PT	1.77	1.41	1.26	4.84	4.45	1.09	5.21	6.74	0.77
LB7-PT	1.78	1.81	0.98	5.05	4.32	1.17	5.44	6.75	0.81
Mean	1.77	1.61	1.12	4.95	4.39	1.13	5.33	6.75	0.79

7.2 Force-Deformation Models

The measured force-displacement responses of the two post-tensioned specimens were compared with the responses predicted by the analytical model developed by Mookerjee (1999) and calibrated by Elwood and Eberhard (2006). The model is based on moment-curvature analysis and simple models of anchorage slip and shear flexibility. The total compressive load on the columns was due to the externally applied axial load and the varying prestress force. Two conditions were considered: 1) using the external axial load plus the initial prestress force (force in the PT bar at the beginning of testing); 2) using the external axial load plus the prestress force at a drift ratio of 3 percent. The first condition was considered to underestimate the flexural strength of the columns because of the increasing prestress force at larger drifts. A description of the modeling methodology provided by Pang et al. (2008) is repeated here for convenience:

> The model used different methods to determine the force-displacement response before and after peak lateral-force capacity. Up to the lateral-force capacity, the displacements were calculated for twenty, evenly spaced levels of force. At each force level, the column height was divided into 100 segments for which the axial load and moment were known. For each segment the average curvature was computed from moment-curvature analysis, using the Mander, Priestley, and Park (1988) concrete model, and the modified Burns and Siess (1962) steel model. The moment curvature analysis did not account for the twelve #3 bars in the column, which stopped at the interface.
>
> Shear deformations were computed assuming elastic, gross-section properties. Displacements at the top of the column attributable to anchorage slip at the base were accounted for using the bond-slip model proposed by Lehman (1998). The initial average bond stress resistance was taken as $9.6\sqrt{f'_c}$ for development of bars at the surface of the concrete or grout, and as $14.4\sqrt{f'_c}$ for the anchorage of the debonded bars,

which were anchored at a depth of 8 d_b below the interface. The debonding was assumed to be 100 percent effective.

Beyond the lateral-force capacity, lateral forces were calculated from deflections using a plastic-hinge approach (Priestley et al., 1996) for 40 levels of displacement. For each deflection beyond yield, the curvature of the plastic hinge was estimated, and then corresponding moment and lateral force was determined from the moment-curvature relationship. [...] The model included the effects of debonding in the slip component of the total displacement (Pang et al., 2008).

Table 7-3 presents the key results from the moment-curvature analysis. In this table, the "Ideal" flexural strength corresponds to the moment calculated by assuming that the concrete has a maximum strain of 0.004 and by neglecting strain hardening.

The components of the total displacement due to flexure, slip, and shear are reported in Table 7-4 and Figure 7-2. For both columns, the calculated displacements were dominated by flexural (53 percent) and anchorage slip (46 percent) components of displacement. The shear contribution was less than 2 percent for all calculations. The higher axial load had the effect of decreasing the total displacement somewhat, while decreasing the contribution from flexure and slip slightly, and increasing slightly the contribution from shear.

Table 7-3. Results from moment-curvature analysis.

	$P_{PT,\ initial}$		$P_{PT,\ at\ 3\%\ drift}$	
	LB6-PT	LB7-PT	LB6-PT	LB7-PT
Cracking Curvature (1/inch) 10^{-6}	28.7	28.5	31.9	31.5
Cracking Moment (kip-inch)	1034	1044	1166	1172
First Yield Curvature (1/inch) 10^{-6}	216	191	224	197
First Yield Moment (kip-inch)	2682	2754	2931	2983
Ideal Flexural Strength (kip-inch)	3157	3313	3397	3540
Maximum Moment (kip-inch)	3399	3743	3598	3925

Table 7-4. Displacement components at initial yield from force-displacement analysis

Components of Displacement		$P_{PT,\ initial}$		$P_{PT,\ at\ 3\%\ drift}$	
		LB6-PT	LB7-PT	LB6-PT	LB7-PT
Flexure	Displacement (inches)	0.19	0.17	0.19	0.18
	Drift Ratio (%)	0.31	0.29	0.32	0.30
	Contribution to Total (%)	52.6	53.8	52.3	53.0
Slip	Displacement (inches)	0.16	0.14	0.17	0.15
	Drift Ratio (%)	0.27	0.24	0.28	0.25
	Contribution to Total (%)	46.0	44.6	46.2	45.3
Shear	Displacement (inches)	0.01	0.01	0.01	0.01
	Drift Ratio (%)	0.01	0.01	0.01	0.01
	Contribution to Total (%)	1.40	1.61	1.49	1.68
Total	Displacement (inches)	0.36	0.32	0.37	0.34
	Drift Ratio (%)	0.60	0.54	0.61	0.56
	Contribution to Total (%)	100	100	100	100

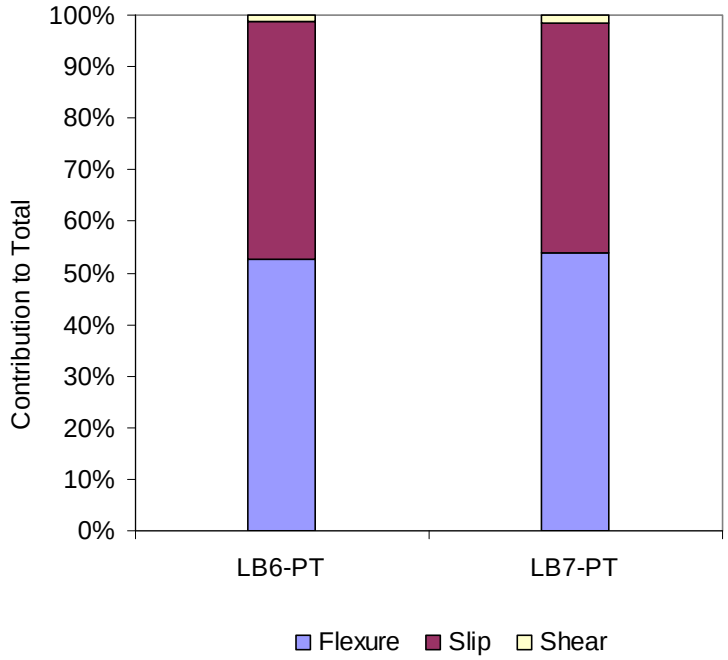

Figure 7-2. Displacement components' contribution to total at initial yield for $P_{PT,\ initial}$.

Figures 7-3 and 7-4 compare the measured and calculated force-displacement envelopes for specimens LB6-PT and LB7-PT. In both cases *P* was taken as the external axial load plus initial prestress force. The results presented in Table 7-5 indicate the precision of the prediction based on the model vs. the measured response; this is presented as the ratios of the measured moment to the calculated moment and the ratios of the measured effective stiffness to the calculated effective stiffness. Table 7-5 also

gives information for Specimen LB8-D1. It was not post-tensioned and acted as a reference for the PT specimens.

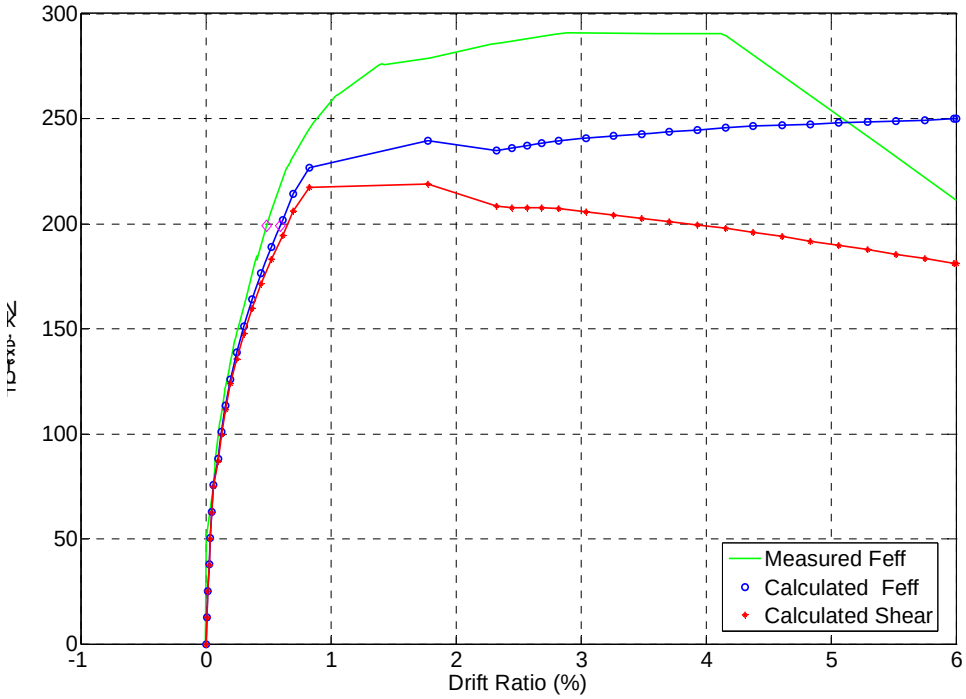

Figure 7-3. Specimen LB6-PT force-displacement envelopes (with $P_{PT,\ initial}$).

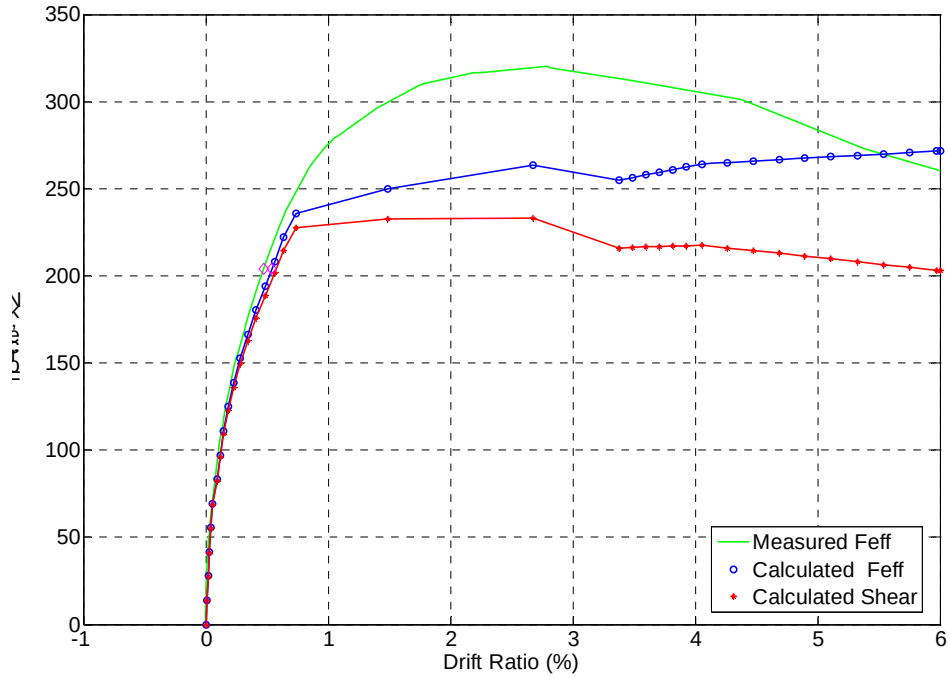

Figure 7-4. Specimen LB7-PT force-displacement envelopes (with $P_{PT,\ initial}$).

Table 7-5. Comparison of results: model vs. measured.

Specimen		LB6-PT	LB7-PT	LB8-D1	Mean	Standard Deviation	Coefficient of Variation
	$M^{meas.}_{(max)}$ (kip-inch)	3924	4323	4335	4194	191	4.55 %
$P_{PT,\ initial}$	$\frac{M^{meas.}_{(max)}}{M^{calc.}_{(max)}}$	1.16	1.18	1.01	1.12	0.08	6.79 %
	$\frac{K^{meas.}_{effective}}{K^{calc.}_{effective}}$	1.23	1.12	0.92	1.09	0.13	11.77 %
$P_{PT,\ at\ 3\%\ drift}$	$\frac{M^{meas.}_{(max)}}{M^{calc.}_{(max)}}$	1.10	1.12	1.01	1.08	0.05	4.44 %
	$\frac{K^{meas.}_{effective}}{K^{calc.}_{effective}}$	1.04	0.98	0.92	0.98	0.05	5.00 %

As can be seen in figures 7-3 and 7-4, the calculated stiffness of the specimens was lower than the measured stiffness for both PT columns. The measured maximum moment exceeded the calculated maximum moment by about 17 percent for the PT columns when the input compressive load was the initial prestress force in addition to the external axial load. The same calculations performed with a total compressive load equal to the prestress force at a drift ratio of 3 percent plus the external axial load resulted in a slightly better prediction by the model for the PT columns. The measured maximum moment was then only 11 percent larger than the calculated one. For LB8-D1, which was not post-tensioned, the model predictions were extremely good, giving 101 percent and 92 percent of the measured strength and stiffness, respectively.

The model's under-prediction of the peak moment by 8 percent on average may have been influenced by the presence of twelve #3 bars in the column right up to the interface. These may have both carried some axial load in compression and added to the concrete confinement. Both effects would have reduced the size of the concrete stress block, increased the lever arm, and increased the moment strength. These effects were not represented in the model.

7.3 Comparison with ACI Nominal Flexural Strength

The nominal flexural strengths for the specimens were calculated according to the ACI 318-05 Building Code Requirements for Structural Concrete (ACI Committee 318 2005). and are reported in Table 7-6. The measured moments were about 30 percent larger than the ones calculated according to the ACI procedure, when the axial load included the initial prestress value. The fit improved when the prestress force at a drift ratio of 3 percent was used.

Table 7-6. Comparison of results: ACI vs. measured.

Specimen		LB6-PT	LB7-PT	LB8-D1	Mean	Coefficient of Variation
	$M^{meas.}_{(max)}$ (kip-inch)	3924	4323	4335	4194	4.56 %
$P_{PT,\ initial}$	M^{ACI} (kip-inch)	3063	3247	3880	3397	10.3 %
$P_{PT,\ initial}$	$\frac{M^{meas.}_{(max)}}{M^{ACI}_{(max)}}$	1.28	1.33	1.12	1.24	7.3 %
$P_{PT,\ at\ 3\%\ drift}$	M^{ACI} (kip-inch)	3357	3462	3880	3566	6.3%
$P_{PT,\ at\ 3\%\ drift}$	$\frac{M^{meas.}_{(max)}}{M^{ACI}_{(max)}}$	1.17	1.25	1.12	1.18	4.5%

CHAPTER 8: SUMMARY AND CONCLUSIONS

8.1 Summary

This research study addressed the seismic performance of reinforced concrete columns that also contain unbonded post-tensioned reinforcement. The primary goal of the research was to study the influence of the ratio of prestressed to mild steel reinforcement on the residual displacements after an earthquake.

Hieber (2005) proposed a simple equation to calculate the re-centering ratios of such columns:

$$\lambda_{re} = \frac{P_{col} + A_p \cdot f_{po}}{A_s \cdot f_y}$$

The primary variables in it are the external axial load on the column (P_{col}), the yield strength of the mild steel reinforcement (f_y), and the initial prestressing force ($A_p f_{po}$). According to this equation a column with a re-centering ratio of less than 1.0 would have no re-centering ability, and columns with re-centering ratios of larger than 1.0 would have good re-centering capabilities. This predicted behavior is based on an idealization of the column.

Experiments were conducted to investigate the relationship between the re-centering ratio and the cyclic displacement at zero lateral force, an indirect measure of the residual displacement. Two scaled columns were built and tested under cyclic lateral load. The two columns had nominal re-centering ratios of 1.2 and 1.6, which were achieved by using similar initial prestress forces but different mild steel reinforcement ratios. The external axial load was the same in both cases. A column tested previously by Pang (2008) had similar dimensions but no post-tensioning. It had a nominal re-centering ratio of 0.91 and was used for comparison.

The data from the tests were used to evaluate the relationship between re-centering capability, as predicted by Hieber's equation, and the re-centering achieved in practice, as measured by the displacements at zero lateral force.

8.2 Conclusions

The following conclusions were drawn from the study:

- The three columns had been designed to have approximately the same lateral strength. Their moment-drift envelopes were all similar. Slight differences occurred because of the need to select specific bars in each column. The non-PT column showed a slightly greater resistance at drifts of greater than 4 percent.
- The two PT columns showed better re-centering abilities than the non-PT one, but only at drift ratios of larger than 2 percent. Re-centering was judged by the displacements at zero force.
- The sequence of damage was comparable for all three columns. Little damage occurred at drift ratios of below 2 percent. Significant spalling began at a 2.8 percent drift ratio. Bar buckling was first observed at a 4.3 percent drift ratio for the PT columns, a little earlier than for the non-PT column. Spiral fracture and column bar fracture also occurred earlier in the PT columns, which was not surprising, as the total axial load on the PT columns was considerably higher than that on the non-PT column at those larger drifts. The PT columns also had a lower mild reinforcement ratio than the non-PT column.
- Each post-tensioned column simulated precast construction. As expected, the column rotated essentially as a rigid body, with almost all of the deformations taking place at the interface section. This behavior was accentuated by the fact that some of the column bars were discontinuous across the interface.
- The PT bars started to yield at a drift ratio of 2 percent, which reduced the PT force at zero displacement. In turn, the yielding reduced the theoretical re-centering ratio and would likely lead to an increase in residual displacements. The PT bars started to yield gradually and did not exhibit a flat yield plateau, so their proportional limit lay below their nominal yield strength. This fact should be taken into account when an initial post-tensioning stress is selected. The actual steel yield stress, as opposed to the nominal one, should also be used to calculate the re-centering ratio.
- Damage progression models predicted damage states within 21 percent of the measured ones on average. Force-Deformation models better predict the measured

moment strength by using the prestress force at 3 percent drift, within 8 percent on average, as opposed to using the initial prestress force.

8.3 Recommendations for Further Research

The re-centering ability of the PT bars started to decline because of the bars reaching their proportional limit at the same time as re-centering started to take effect. To engage the full effect of the post-tensioning on minimizing the residual displacements, it is suggested that future columns be built with an initial stress that is a smaller fraction of the proportional limit. This could be achieved by using larger PT bars with a smaller initial stress or by using strands instead of bars. Strands have much higher yield strengths and strains than bars.

Additional work is still needed on modeling the behavior of re-centering systems to be able to predict the residual displacements accurately.

Further experiments are also needed to study alternative details for the column base, where the damage accumulates. For example, adding a jacket around the column in the plastic hinge region would confine the concrete better and possibly delay the onset of bar buckling. The jacket would also prevent spalling of the cover, which would probably minimize the repairs needed after a small to moderate earthquake. If the column is precast, the jacket could possibly be cast in with the column at the precast plant

REFERENCES

AASHTO (2005). "LRFD Bridge Design Specifications," 4th ed., American Association of State Highway and Transportation Officials, Washington, DC.

ACI Committee 318 (2005). "Building Code Requirements for Structural Concrete and Commentary." *ACI 318-05/ACI 318-05R*, American Concrete Institute, Farming Hills, MI.

Berry, M., and Eberhard, M. (2003a). "Performance Models for Flexural Damage in Reinforced Concrete Columns." *Pacific Earthquake Engineering Research Center Report 2003*, University of California, Berkeley California.

Berry, M., and Eberhard, M. (2003b). "Performance Modeling Strategies for Modern Reinforced Concrete Bridge Columns." *Pacific Earthquake Engineering Research Center Report 2003*, University of California, Berkeley California.

Berry, M., and Eberhard, M. (2005). "Practical Performance Model for Bar Buckling." Journal of Structural Engineering, ASCE, Vol 131, No 7, July 2005, pp 1060-1070.

Brown, W. (2008). "Bar Buckling in Reinforced Concrete Bridge Columns." Master's Thesis, University of Washington, Seattle, WA.

Building Seismic Safety Council. (2003). "NEHRP Recommended Provisions for Seismic Regulations for New Buildings and Other Structures (FEMA 450)." *National Earthquake Hazards Reduction Program*, National Institute of Building Sciences, Washington, D.C.

Burns , N. and Seiss, C. (1962). "Load-Deformation Characteristics of Beam-Column Connections in Reinforced Concrete." *Civil Engineering Studies Structural Research Series No. 234*, University of Illinois, Urbana, Illinois.

Elwood, K. and Eberhard, M. (2006). "Effective Stiffness of Reinforced Concrete Columns," *PEER Research Digest 2006-1*, March 2006, pp 4.

Hieber, D.. (2005). "Precast concrete pier systems for rapid construction of bridges in seismic regions," Master's thesis, University of Washington, Seattle, WA

Hieber, D., Wacker, J., Eberhard, M., and Stanton, John F. (2005a). "Precast Concrete Pier Systems for Rapid Construction of Bridges in Seismic Regions." *Washington State Department of Transportation Report No. WA-RD-611.1*, Washington State Department of Transportation, Washington, 2005.

Hieber, D., Wacker, J., Eberhard, M., and Stanton, J. (2005b). "State of the Art Report on Precast Concrete Systems for Rapid Construction of Bridges." *Washington State Department of Transportation Report No. WA-RD-549.1*, Washington State Department of Transportation, Washington, 2005.

Jeong, H. (2005). "Seismic Response of New Methods for Reducing Residual Displacement of Reinforced Concrete Bridge Columns." Master's thesis, University of California, Berkeley, CA.

Lehman, D. (1998). "Performance-Based Seismic Design of Well-Confined Concrete Columns.' Ph.D. Dissertation, Department of Civil and Environmental Engineering, University of California, Berkeley, CA.

Mander, J. Priestley , M., and Park, R. (1998). "Theoretical Stress-Strain Model for Confined Concrete." *Journal of the Structural Division ASCE 114(8)*, 1804-1826.

Mookerjee, A. (1999). "Reliability of Performance Estimates of Spiral/Hoop Reinforced Concrete Columns." Master's Thesis, University of Washington, Seattle, WA.

Nakaki, S., Stanton, J., Sritharan, S. (1999). "Overview of the PRESSS five-story precast test building," PCI Journal, v 44 n2, Mar-Apr 1999, p 26-39.

Palermo, A., Pampanin, S., and Calvi, G. (2005). "Concept and Development of Hybrid Solutions for Seismic Resistant Bridge Systems." Journal of Earthquake Engineering, Vol. 9, No. 6. pp 899-921

Pang, J. (2008). "Large-Bar Precast Bridge Bent Connection for Rapid Construction in Seismic Regions," Master's thesis, University of Washington, Seattle, WA

Pang, J. Steuck, K., Cohagen, L., Stanton, J., Eberhard, M. (2008) "Rapidly Constructable Large-Bar Precast Bridge-Bent Seismic Connection." *Washington State Department of Transportation Report No. WA-RD 684.2 Draft*, Washington State Transportation Center.

Priestley, M., Seible, F., and Calvi, G. (1996). "Seismic Design and Retrofit of Bridges." John Wiley and Sons, Inc., New York.

Stanton, J., Stone, W. and Cheok, G. (1997). "A Hybrid Reinforced Precast Frame for Seismic Regions". PCI Jo. 42(4), Mar-Apr, 20-33.

Steuck, K., Pang, J., Stanton, J., and Eberhard, M.. (2007) "Anchorage of Large Bars in Grouted Ducts." *Washington State Department of Transportation Report No. WA-RD 684.1*, Washington State Transportation Center.

Wacker, J., Hieber, D., Eberhard, M., and Stanton, J. (2005). "Design of Precast Concrete Piers for Rapid Construction of Bridges in Seismic Regions." *Washington State Department of Transportation Report No. WA-RD-629.1*, Washington State Department of Transportation, Washington, 2005.

APPENDIX A: SPECIMEN CONSTRUCTION DRAWINGS

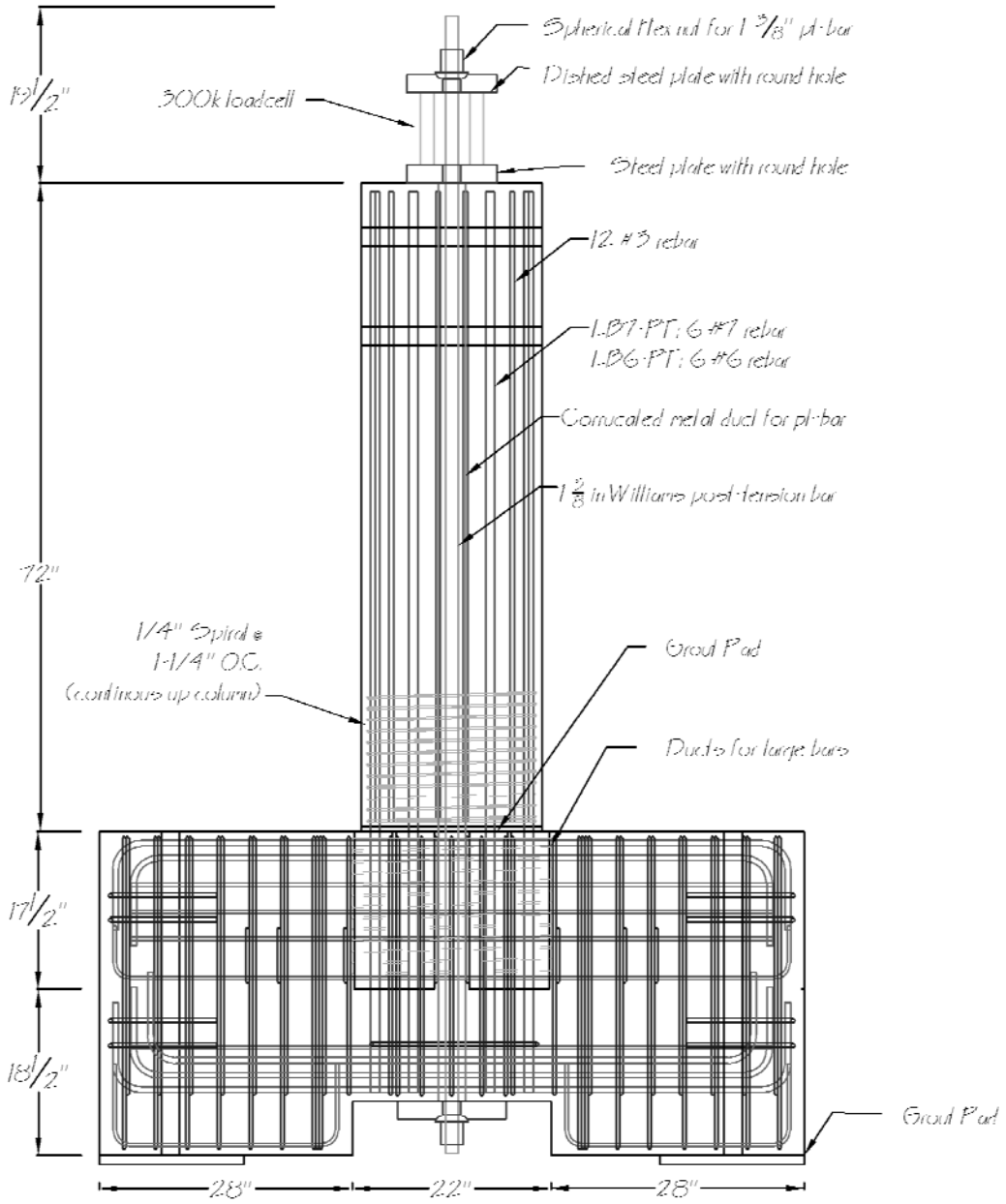

Figure A-1. Specimen west elevation.

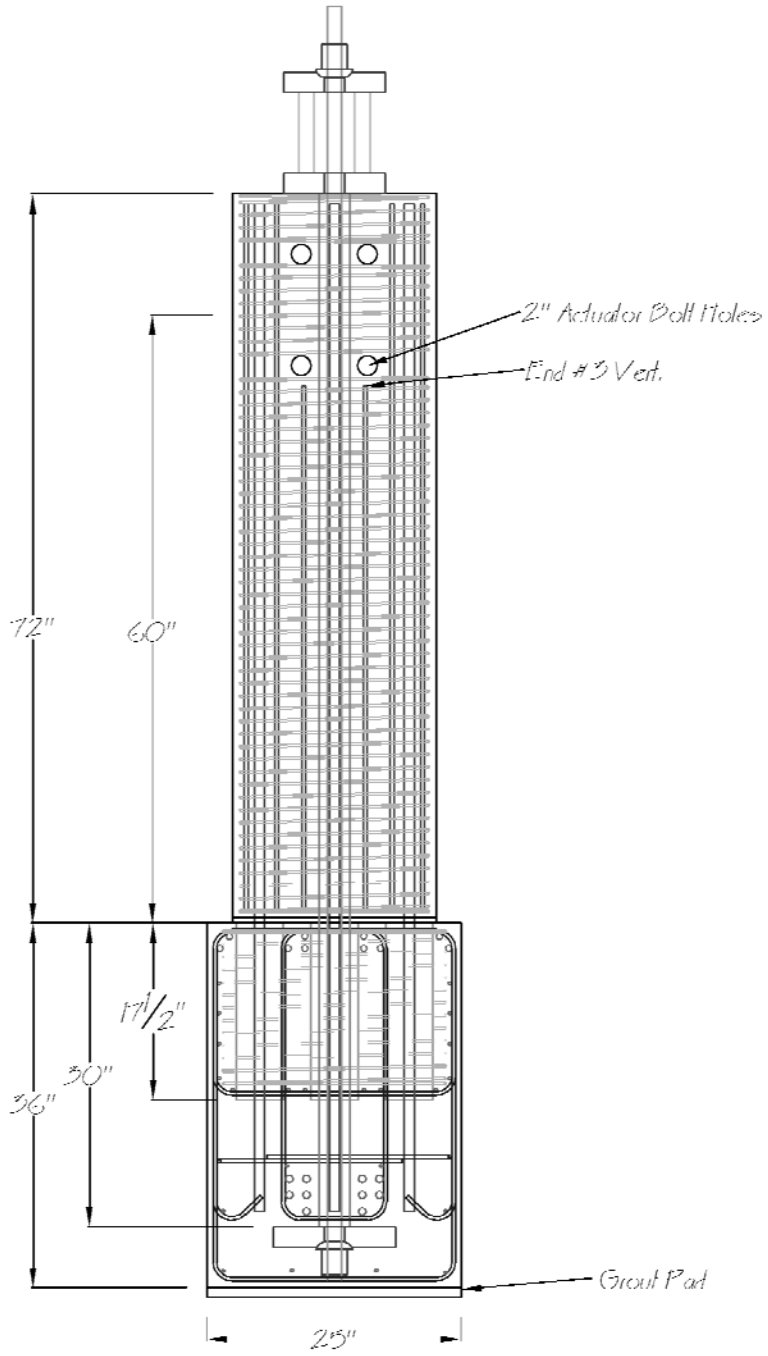

Figure A-2. Specimen north elevation.

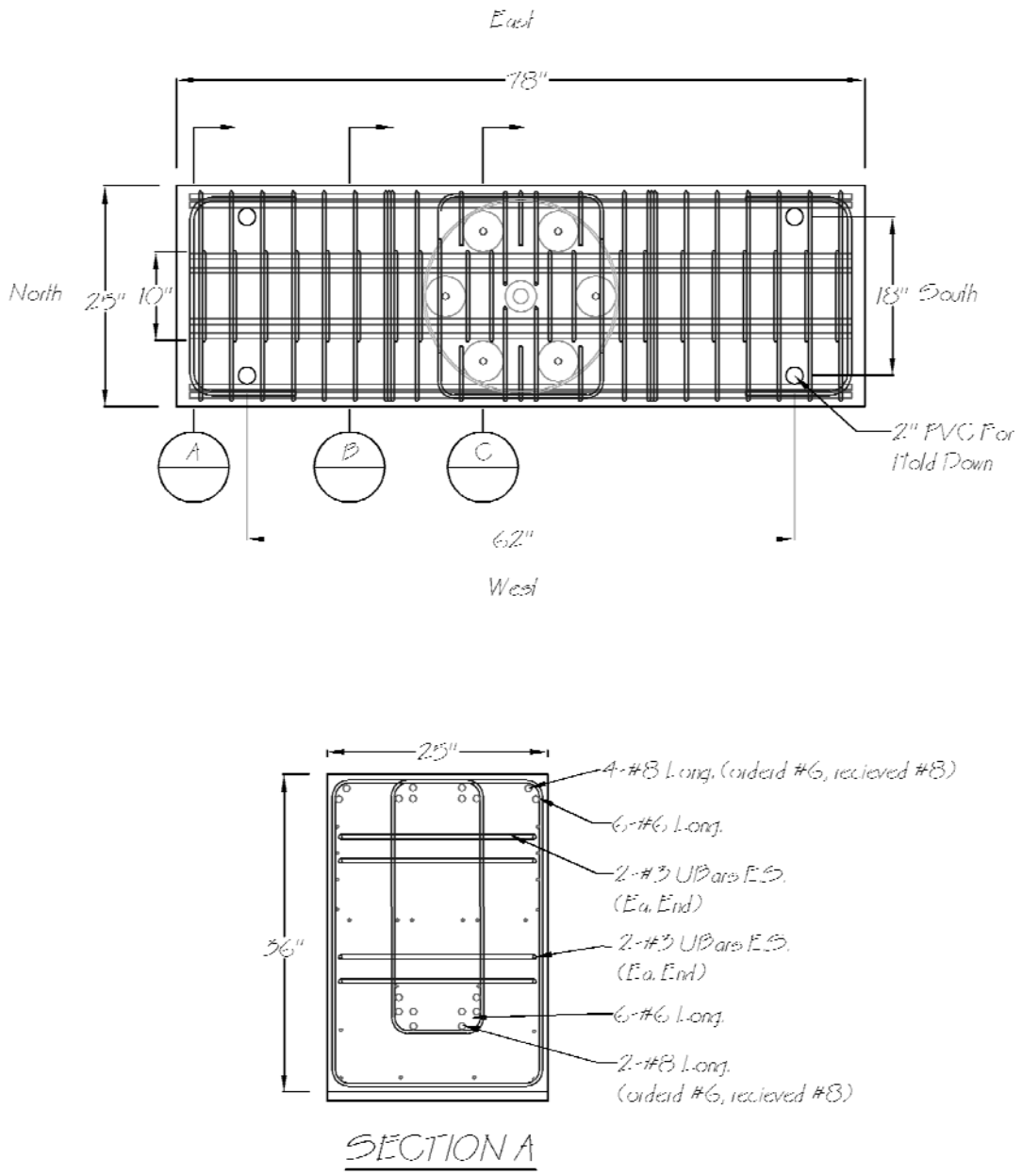

Figure A-3. Above: Specimen cap beam plan view. Below: Cap-Beam section.

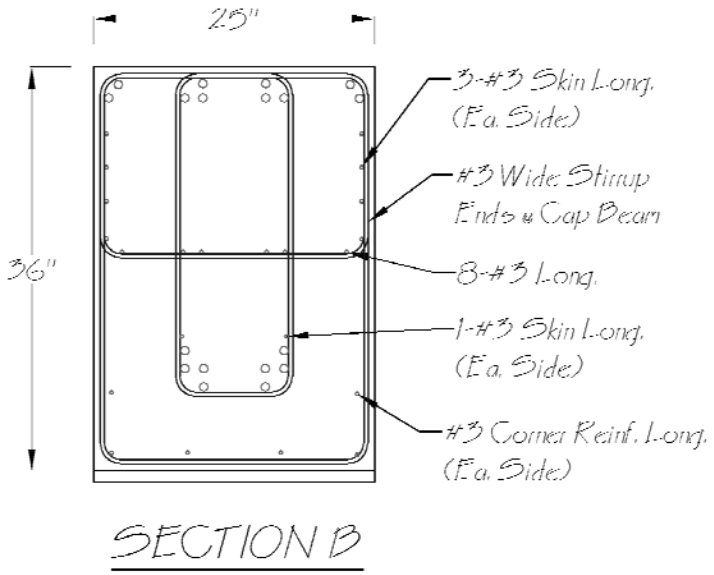

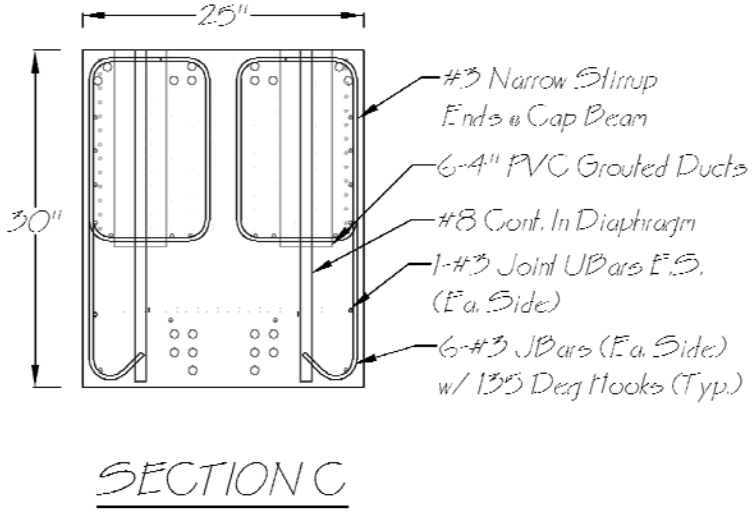

Figure A-4. Specimen cap-beam sections.

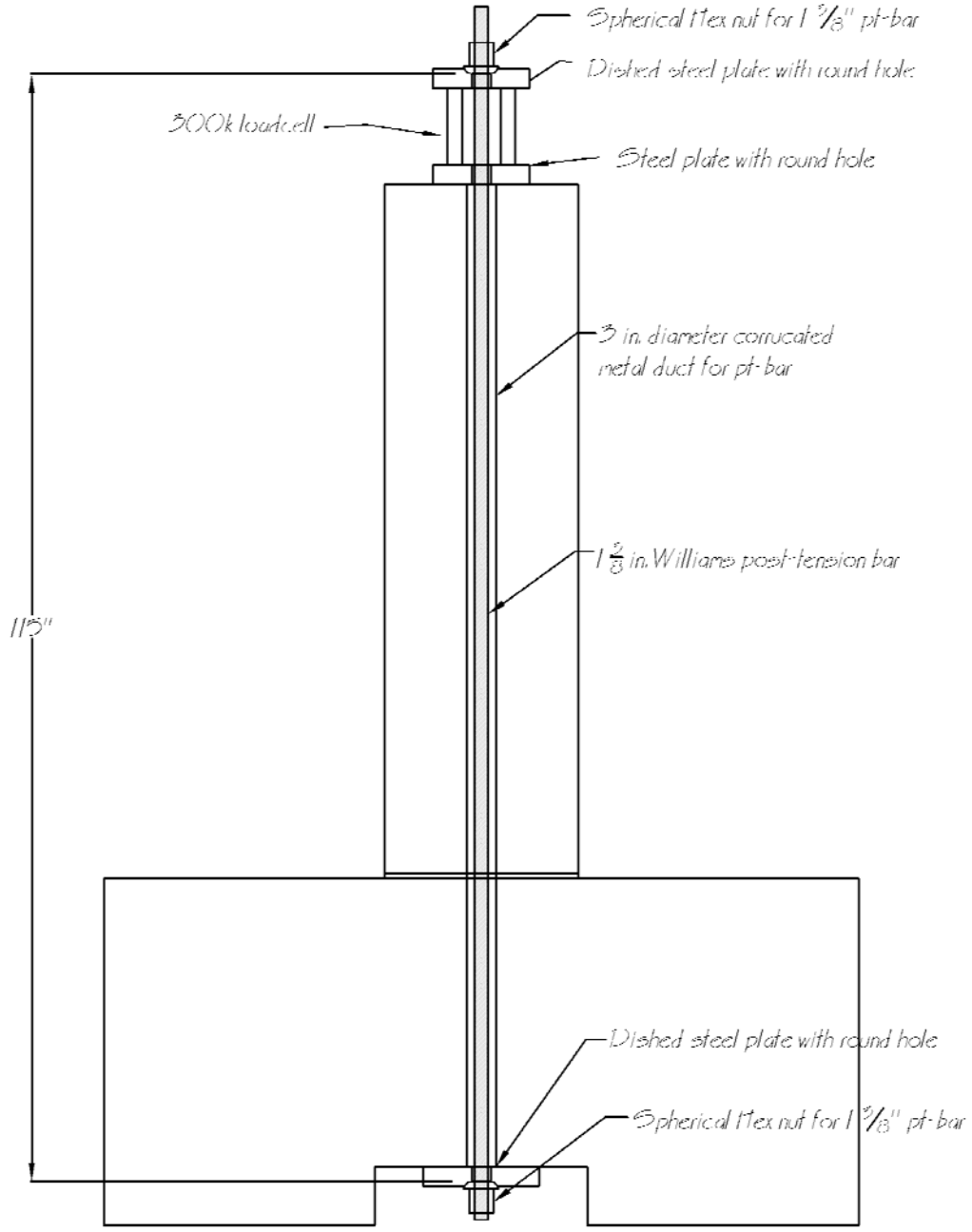

Figure A-5. PT bar unbonded length and setup.

APPENDIX B: MATERIAL TESTS

B.1 Concrete Strengths

The average cylinder strengths are presented in Section 5.1.1. Here all the concrete strength measurements that were taken are reported in Table B-1 and Figure B-1.

Table B-1. Concrete cylinder strength test results.

	Cap-Beam Cylinders			Column Cylinders		
days	#	lbs	psi	#	lbs	psi
7	1	98797	3494	1	111130	3930
	2	114650	4055	2	117340	4150
	3	100710	3562	3	111210	3933
14	1	144100	5096	1	160080	5662
	2	141820	5016	2	153870	5442
	3	139270	4926	3	-	-
28	1	153290	5422	1	173070	6121
	2	172810	6112	2	171840	6078
	3	-	-	3	-	-
49 (LB6-PT test day)	1	193930	6859	1	178250	6304
	2	208530	7375	2	191990	6790
	3	193400	6840	3	183830	6502
67 (LB7-PT test day)	1	199390	7052	1	174140	6159
	2	213060	7535	2	194310	6872
	3	217230	7683	3	189680	6709

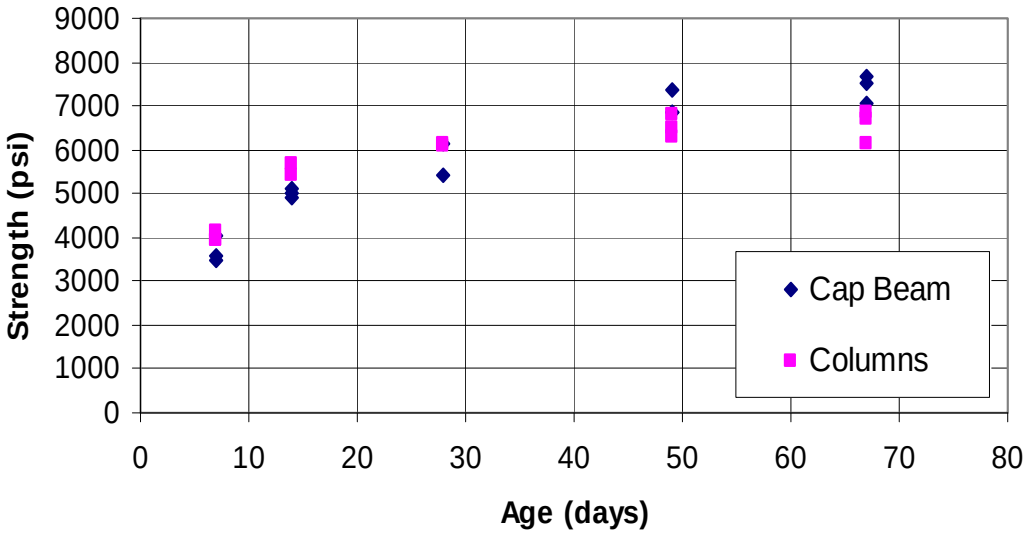

Figure B-1. Concrete strength results.

B.2 Grout Strengths

Section 5.1.2 reports only average strengths for the test days. This section presents all the grout cube measurements taken in tables B-2 and B-3. The same results are presented in Figure B-2.

Table B-2. Specimen LB7-PT grout cube strengths.

LB7-PT	cube	dimensions		measured strength	
days	#	in. x in.		lbs	psi
5	1	1.989	1.953	20010	5151
	2	1.990	2.024	24330	6041
	3	1.991	1.961	23010	5893
16	1	1.978	1.990	24640	6260
	2	1.991	2.012	24040	6001
	3	2.008	1.989	23010	5761
29	1	1.986	1.965	24240	6211
	2	1.991	1.963	28060	7180
	3	1.995	1.959	25730	6584
90	1	1.999	1.990	36090	9072
	2	1.971	1.968	35780	9224
	3	1.992	1.992	42630	10743

Table B-3. Specimen LB6-PT grout cube strengths.

LB6-PT	cube	dimensions		measured strength	
days	#	in	in	lbs	psi
16	1	2.002	2.012	29770	7391
	2	2.018	2.021	25790	6324
	3	1.997	2.004	29260	7311
29	1	2.008	2.011	30460	7543
	2	2.001	2.002	34830	8694
	3	2.003	2.009	30310	7532
66	1	2.031	2.003	37850	9304
	2	2.013	1.996	40400	10055
	3	2.016	1.994	40030	9958

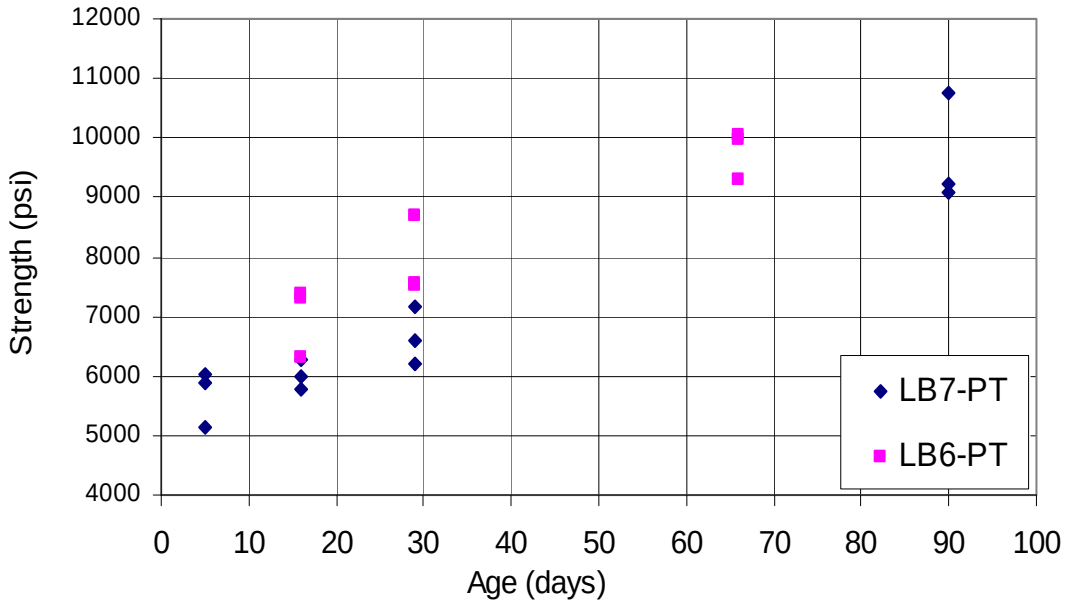

Figure B-2. Grout cube strengths.

B.3 Mild Steel Reinforcement Stress-Strain Behavior

All the mild steel conformed to either ASTM standard A706 or A615, with all the longitudinal column bars belonging to the first (A706).

The tension tests were performed in a 300k Baldwin Universal Testing Machine. Key measured mild steel properties are presented in Section 5.1.3. The full stress-strain curves for the tested bars are shown in figures B-3 through B-5.

During the tension tests, load and elongation were measured. To obtain the stress, the load was divided by the nominal bar area, and to find the strain, the elongation was divided by the gauge length, which was 3 inches for the #6 and #3 bars, and 3.25 inches for the #7 bar.

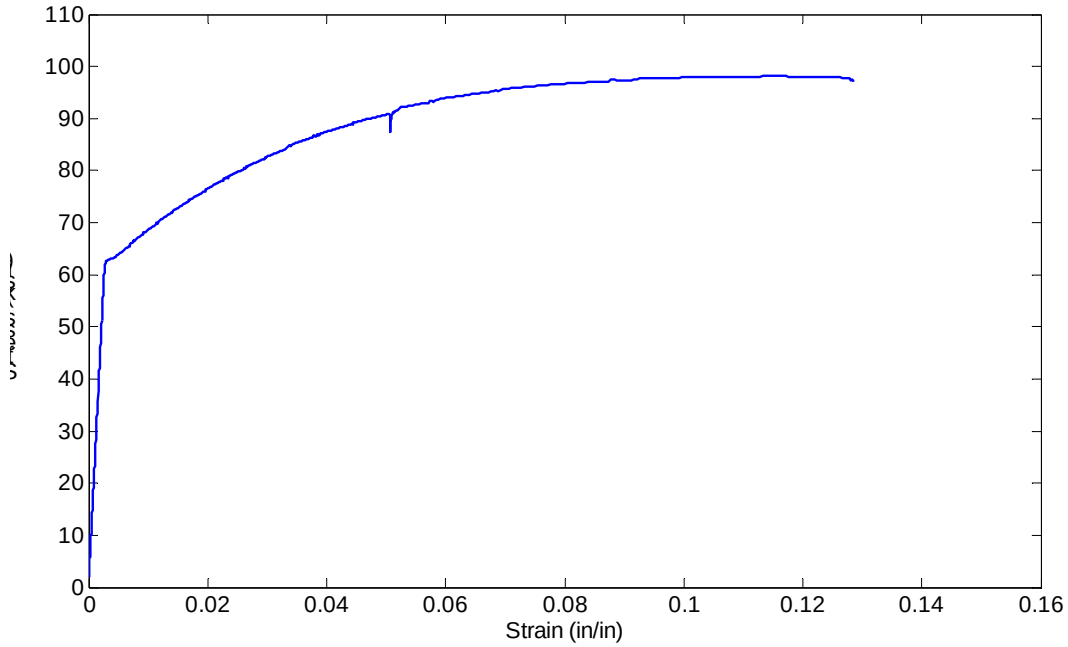

Figure B-3. Stress-strain curve for the #6 reinforcing bars.

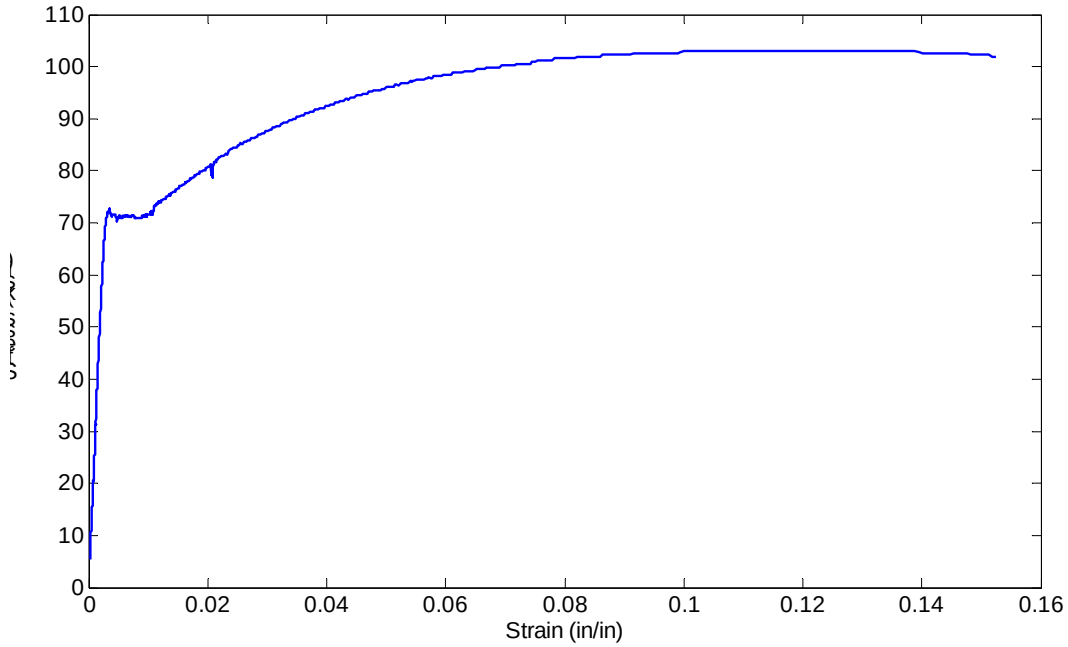

Figure B-4. Stress-strain curve for the #7 reinforcing bars.

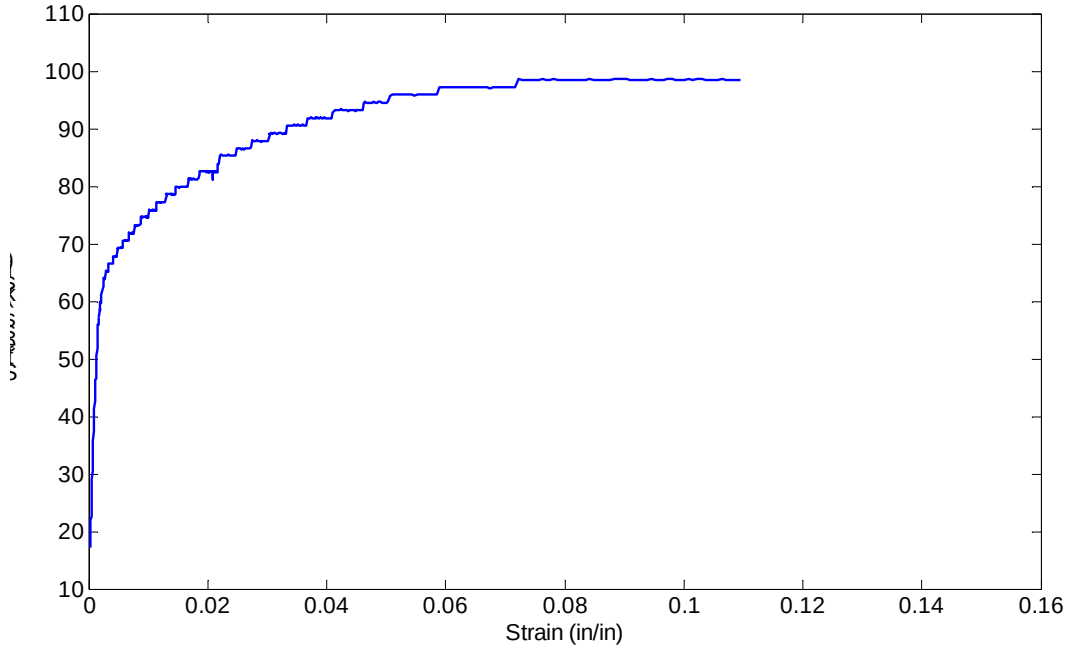

Figure B-5. Stress-strain curve for the #3 reinforcing bars.

B.4 PT Bar Stress-Strain Behavior

The PT bars used in the specimen columns were 1 3/8-inch, 150-ksi, all-thread bars from Williams Form Engineering Corp. They conformed to ASTM A722 standards and AASHTO M275 Highway Specifications. According to the manufacturer the bars were specified to have a minimum yield strength of 190 kips and a minimum ultimate strength of 237 kips.

The tension tests were performed in a 300-k Baldwin Universal Testing Machine. The tests were carried out on two coupons: one on an unused piece of bar that was cut off a bar that was then used in the specimen test; the other one was a piece of the used LB7-PT bar. Load was measured throughout the whole test, but elongation was only measured until just over the yield strength to spare the instrument from damage. The bar stress was calculated by dividing the load by the nominal bar area. The strain was calculated by dividing the measured elongation by the gauge length, which was 24 inches.

Although the test machine had a capacity of 300 kips, when the bars were first tested it only reached a load of about 250 kips and did not fracture the bars. At this point, the stress had surpassed the ultimate strength supplied by the manufacturer, and the stress

exceeded that experienced during the tests. The unused bar was tested conventionally, but the used bar was loaded, unloaded, and reloaded a few times during the testing to simulate the cyclic deformations that the PT bars in the specimens went through. Figures B-6 and B-7 show the stress-strain curves for the bars.

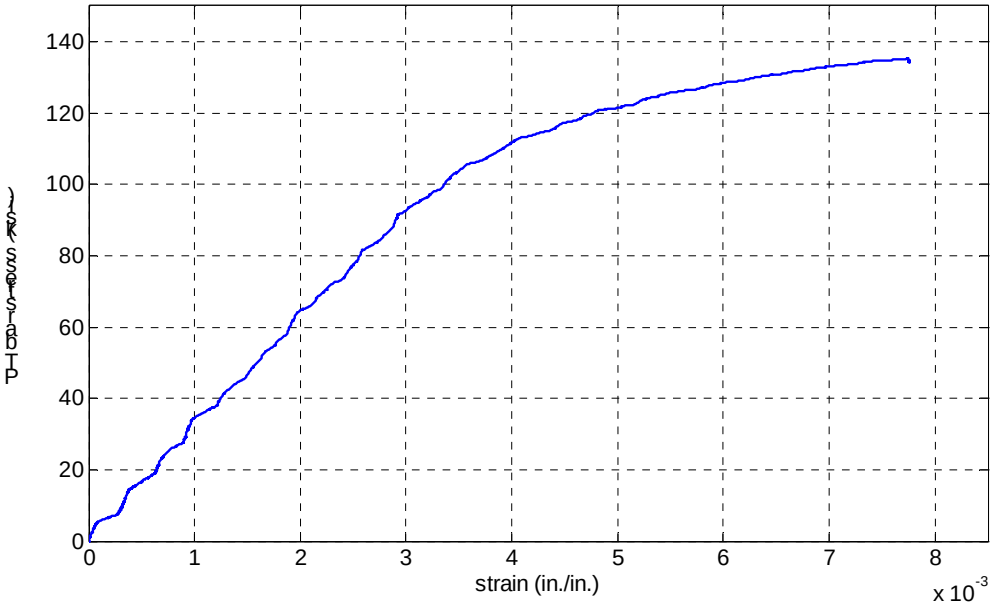

Figure B-6. Stress-strain curve for the unused PT bar.

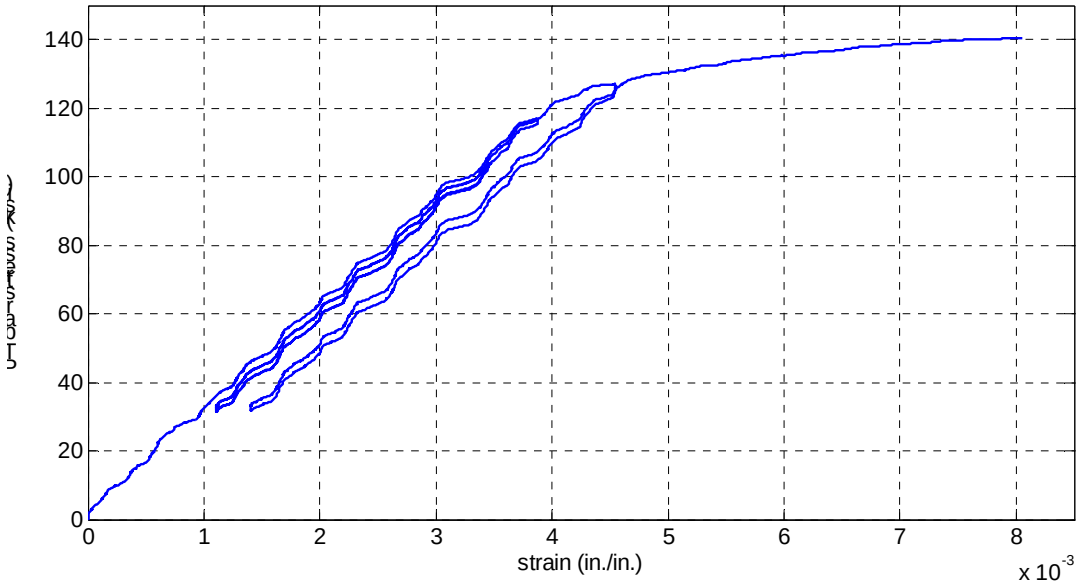

Figure B-7. Stress-strain curve for the used (LB7-PT) PT bar.

The coupon lengths were 67.625 in. for the unused bar and 72.125 in. for the used bar. The threads were machined off over a length of 6 inches and centered about the gauge length, on two opposite sides, as shown in Figure B-8. This was done to make sure that the bar would fracture in that location. Marks were made in the bar on two sides at center, ±2 in. from center, and then at 4-in. intervals so that the elongation of the bar could be calculated.

Both bars were tested a second time to obtain the ultimate strength of the bars, but the elongation was not measured. This time the unused bar was tensioned until it fractured. It fractured in the machined region shown in Figure B-8, in-between the centerline, and 2 in. down. This region experienced considerable necking.

Figure B-8. PT bar used in tension test.

The used bar was tested until it started necking (which happened in the center of the machined section) but was not fractured; at that time the bar had already reached its maximum strength. The ultimate strength of the unused bar was 266 kips (168 ksi on the nominal bar area) and 269 kips (170 ksi on the nominal bar area) for the used LB7-PT

bar. That is about 13 percent higher than the ultimate strength provided by the manufacturer.

Table B-4 provides measurements of the bar section lengths before and after the first set of tests to about 250 kips. Table B-5 presents these measurements for the second set of tests to the ultimate load capacity. As can be seen in Table B-4 the elongation of the coupons was quite evenly distributed over all the measured sections for the first set of tests. For the second set of tests, in which the bars were tested up to their ultimate capacity, both bars necked, which resulted in considerably larger elongation in the necked regions in comparison to other sections. Sections outside the necked regions had fairly even amounts of elongation.

According to ASTM A722 standards, the minimum elongation after rupture is 4.0 percent using a gauge length of 20 bar diameters (27.5 in. for a 1 1/8-in. bar), or 7.0 percent with a gauge length of 10 bar diameters (13.75 in. for a 1 1/8-in. bar). The fractured bar from the tension test had an average elongation of 6.9 percent over the 24-in. gauge length. For comparison, a number 11 A706 Low-Alloy Steel Deformed Bar has a specified minimum elongation of 12 percent over a gauge length of 8 in. If we look at the fractured PT bar over the section from 2 inches up from center to 6 inches down from center, the average elongation was 11 percent, which is fairly close.

Table B-4. PT bar section lengths for test to 250 kips.

	New bar section lengths (in.)			Used bar section lengths (in.)		
Section	Before test	After test	% Elongation	Before test	After test	% Elongation
+14 in. - +18 in.	3.988	4.092	2.61	4.011	4.104	2.32
+10 in. - +14 in.	4.024	4.112	2.19	3.996	4.086	2.25
+6 in. - +10 in.	3.987	4.083	2.41	4.009	4.111	2.54
+2 in. - +6 in.	4.01	4.112	2.54	4.018	4.12	2.54
Center - +2 in.	2.012	2.083	3.53	2.018	2.064	2.28
Center - -2 in.	2.01	2.084	3.68	2.021	2.063	2.08
-2 in. - -6 in.	3.991	4.081	2.26	3.99	4.087	2.43
-6 in. - -10 in.	4.018	4.125	2.66	4.003	4.09	2.17
-6 in. - -10 in.	3.998	4.108	2.75	4.012	4.109	2.42
-10 in. - -14 in.	4.039	4.11	1.76	4	4.117	2.93
-14 in. - -18 in.	3.995	4.073	1.95	3.999	4.106	2.68

Table B-5. PT bar section lengths for test to ultimate load and fracture.

	New bar section lengths (in.)			Used bar section lengths (in.)		
Section	Before test	After test	% Elongation	Before test	After test	% Elongation
+14 in. - +18 in.	3.988	4.205	5.4	4.011	4.262	6.3
+10 in. - +14 in.	4.024	4.217	4.8	3.996	4.280	7.1
+6 in. - +10 in.	3.987	4.208	5.5	4.009	4.318	7.7
+2 in. - +6 in.	4.01	4.267	6.4	4.018	4.298	7.0
Center - +2 in.	2.012	2.178	8.2	2.018	2.300	14.0
Center - -2 in.	2.01	2.504	24.6	2.021	2.286	13.1
-2 in. - -6 in.	3.991	4.235	6.1	3.99	4.220	5.8
-6 in. - -10 in.	4.018	4.228	5.2	4.003	4.246	6.1
-6 in. - -10 in.	3.998	4.264	6.7	4.012	4.285	6.8
-10 in. - -14 in.	4.039	4.272	5.8	4	4.306	7.7
-14 in. - -18 in.	3.995	4.249	6.3	3.999	4.205	5.2

APPENDIX C: RE-CENTERING RATIO CALCULATIONS

The nominal re-centering ratio is defined in Section 2.2 with Equation 2-3. Equation 2-4 further assumes that all the longitudinal steel bars in the column are at the yield stress, in compression. In reality this is unlikely to be the case; therefore, two other assumptions for the stresses in the steel were made to investigate the sensitivity of the re-centering ratio. The results for all three cases are presented in Figure 2-4, with the calculations described here.

The re-centering ratio was calculated by using Equation 2-3, and it is presented again below:

$$\lambda_{re} = \frac{M_{closing}}{M_{resisting}}$$

where

$$M_{closing} = \left(P_{col} + F_p\right) \cdot \alpha D$$

and

$$M_{resisting} = F_s \cdot \beta D$$

Both the moments defined above are taken about the centroid of the concrete compression area. Therefore, αD is the distance from the center of the column to the centroid of the concrete compression area, and βD is the distance from the centroid of the mild steel bars to the centroid of the concrete compression area. These distances are shown in Figure C-1.

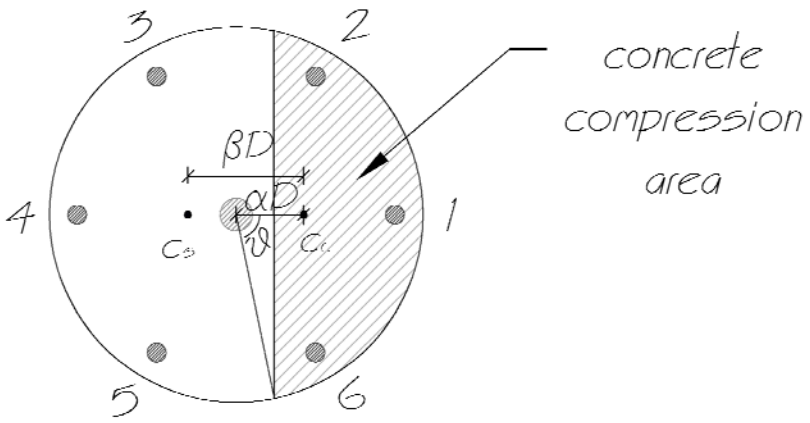

Figure C-1. Column cross-section.

For case 1, assuming that all the longitudinal mild steel bars were approximately at yield in compression, the lever arms for both the closing and resisting moments would be equal ($\alpha = \beta$), so they would cancel out. The re-centering ratio would then simplify to the ratio of the total compressive load ($P_{col} + F_p$) to the mild steel force (F_s), as is the case in Equation 2-4. Case 2 assumed that half the bars were approximately at yield and the other half were at zero stress. The case 3 assumptions were the same as the ones for case 2 with the exception of the one extreme tension bar; it was assumed to have a tensile stress of one-fourth of the yield stress.

For the two additional cases, the lever arms needed to be calculated. To calculate the lever arm for the closing moment, the forces acting on the column cross-section were assumed to be in equilibrium:

$$F_{conc} + F_s = F_{col} + F_p \qquad \textbf{C-1}$$

For simplicity, a uniform concrete compression force was assumed:

$$F_{conc} = 0.85 f_c^{'} A_c \qquad \textbf{C-2}$$

The concrete compression area shown in Figure C-1 is given with the following equation, which was used to find the angle ϑ, shown in Figure C-1.

$$A_c = D^2 \frac{\vartheta - \sin\vartheta\cos\vartheta}{4} \qquad \textbf{C-3}$$

This ϑ value was then input into the following equation, along with the column diameter, to find the distance from the center of the column to the centroid of the cross-section.

$$\alpha D = \frac{D}{3}\frac{\sin^3 \vartheta}{\vartheta - \sin\vartheta\cos\vartheta} \qquad \textbf{C-4}$$

The distance from the center of the column to the centroid of the mild steel bars was calculated as:

$$c_s = \frac{\sum c_{s,i} F_i}{\sum F_i} \qquad \textbf{C-5}$$

This allowed the length of the lever arm βD to be calculated.

Table C-1 presents the stress values assumed for the column bars for all three cases and the computed re-centering ratios for the two PT specimens. Bar numbers refer to Figure C-1. Case 2 and case 3 had nearly the same re-centering ratios, which were, for both specimens, larger than that for case 1, on which the re-centering calculations were based. Case 1 was therefore considered a lower bound to the "real" re-centering ratio.

Table C-1. Three cases of stress value assumptions in the column bars.

Bar #	1	2	3	4	5	6	LB6-PT λ_{re}	LB7-PTλ_{re}
Case 1	$-F_y$	$-F_y$	$-F_y$	$-F_y$	$-F_y$	$-F_y$	1.6	1.2
Case 2	$-F_y$	$-F_y$	$-F_y$	*0*	*0*	*0*	1.88	1.42
Case 3	$-F_y$	$-F_y$	$-F_y$	*0*	*0*	$¼F_y$	1.87	1.41

APPENDIX D: DEBONDED LENGTH CALCULATIONS

The debonding of the large bars is discussed in Section 6.6, and as described there, no conclusions regarding the debonded length could be made. The calculations of the nominal debonded length are explained here.

The total effective debonded length was calculated by using Equation D-1:

$$L_{u,eff} = \Delta / \varepsilon \qquad \textbf{D-1}$$

where Δ is the elongation of the bar, and ε is the average strain at the interface measured by the strain gauges. The strain gauges only provided reliable readings up to about 1.4 percent drift, when the interface gauges started to delaminate, so the debonded length could only be estimated up to that point. Equation D-2 was used to calculate the elongation of the bar:

$$\Delta = \vartheta(D - (c + b)) \qquad \textbf{D-2}$$

where ϑ is the rotation at the interface section that was calculated by using the measurements from the two potentiometers located near the interface. D is the column diameter, c is the distance for the column edge to the neutral axis, and b is the distance from the column edge to the center of the extreme tension bar. These parameters are shown in Figure D-1.

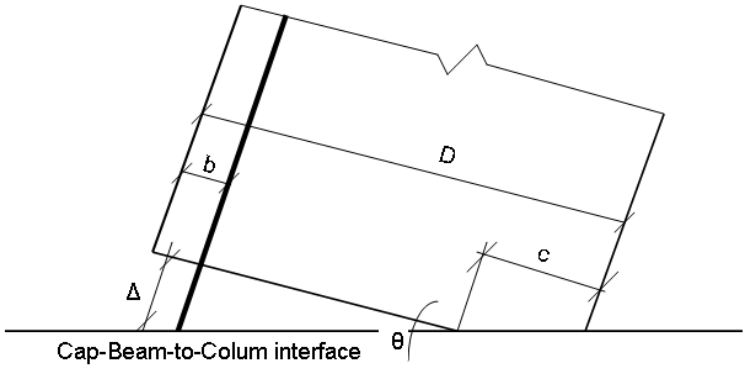

Figure D-1. Parameters used for calculating the bar elongation.

The depth of the neutral axis was calculated in two ways: first using the potentiometer measurements located at the interface section and second using the

information from the force in the PT bar. Equation D-3 was used to calculate the depth of the neutral axis in the second case.

$$c = \frac{D}{2} - \frac{dF}{d\vartheta}\frac{L}{EA} \qquad \textbf{D-3}$$

where D is the diameter of the column, $dF/d\vartheta$ is the slope of the PT force, which is plotted against drift ratio in Figure 5-20. Here, however, the slope was calculated only for the linear part of the curves, and not using the peak and zero values as was done in Section 5.7. L is the unbonded length of the PT bar, E is the elastic modulus, and A is the nominal bar diameter.

In the test specimens, the bar was deliberately debonded over a length of 8 in. and undoubtedly became partially debonded for a short additional distance at each end of that region. The effective debonded length is defined here as the length of bar that would, if it were totally debonded, provide the same relationship between elongation and strain as was found in the test specimen. To determine an approximate length over which the bar was debonded as a result of the applied displacements, the deliberate debonding of the bars over 8 in. was subtracted from the total effective debonded length to give the total effective debonded length at both ends of the sleeve. Half was attributed to each end of the sleeved region. The bond stress in that region was assumed to be uniform, leading to a linear variation in bar stress. Thus the length, l_d, in inches at each end over which the bar was being developed is

$$l_d = 2\left(\frac{l_{de} - 8}{2}\right) = \left(l_{de} - 8\right) \qquad \textbf{D-4}$$

Figure D-2 shows the debonded length vs. drift ratio for both methods and for both specimens. In the very first cycles of the tests, both the drift and the measured strains were extremely small so the debonded length calculations at those drifts were not reliable. They are not shown in Figure D-2.

The total effective debonded length, l_{de}, calculated for the drift ratio interval of 0.2 to 0.6 percent was in the range of 14 to 21 in. for both specimens LB6-PT and LB7-PT, based on calculations with the PT bar. Using the potentiometer measurements resulted in slightly larger debonded length values, especially for LB6-PT for the same interval. These values seemed quite large in relation to the small drift ratios they were

calculated for, especially considering that the true debonded length was most likely larger than the effective one, and in the calculations made here, only the rotations from the interface segment were included. For small drift ratios it is likely that the rotations from other segments higher up in the column contributed more to the total rotation of the column. This would lead to a larger calculated elongation of the bar and thus a larger effective debonded length.

For drift ratios of larger than 0.6 percent the debonded length dropped to 6 to 14 in. Possible reasons for this decreased length are discussed in Section 6.6. The fact that a few points had a total effective debonded length that was smaller than the deliberately debonded length is surprising. As drift ratios increase post-yield, so does the effective debonded length, which is to be expected.

It is likely that the stress decrease was more rapid, and thus this length was shorter, in the cap-beam than in the column because the bars there were grouted into ducts as opposed to being cast directly into the concrete, and they were also much better confined.

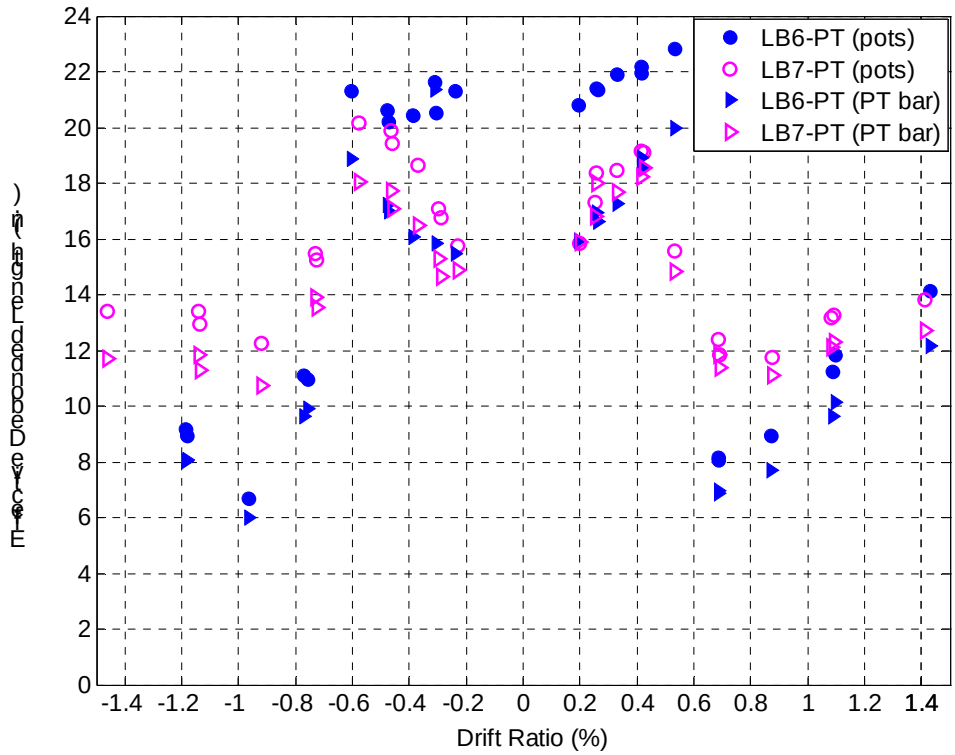

Figure D-2. Debonded length of the mild steel rebar vs. drift ratio.

APPENDIX E: BAR CURVATURE SCHEMATICS

Bar curvatures were presented in Section 5.9.2. Section 6.7 discussed the bar curvature phenomenon.

The bar curvature was defined by Equation 5-6. Because of the way it was defined, the sign of the curvature was constant for all column bars, although, for example, when the column was displaced south, Bar V00 was in tension and Bar V18 was in compression.

Table E-1 presents the curvature directions for the drift ratio interval ±0.2 percent to ±1.2 percent for the column bars in the debonded area. This was done to get a better idea of the behavior of the bar in the debonded area. The magnitudes of the bar curvatures are not represented below, only the direction.

In 40 of the 48 cases shown, the sign of the curvature corresponded to the direction of bending of the column, as might be expected. Most of the contrary cases occurred for Bar V00 in specimen LB6-PT, for drifts of greater than or equal to 0.8 percent. By this drift the bar had yielded at the interface as well as in the debonded area. The yielding of the bar could have caused some permanent deformations in the bar at the yielding location and transferred the bending of the bar as a result of the column lateral displacement farther up into the column. Up in the column, however, gauges were only on the outer sides of the bars, so the curvature could not be calculated there. The good overall correlation suggests that the strain gauge results were reliable.

Table E-1. Bar Curvature schematics.

Drift Ratio		0.2%	-0.2%	0.4%	-0.4%	0.6%	-0.6%	0.8%	-0.8%	1.0%	-1.0%	1.2%	-1.2%
Tens./ Compr.		Tens.	Compr.	Tens.	Compr	Tens.	Compr	Tens.	Compr	Tens.	Compr	Tens.	Compr
LB6-PT V00	0 in. -7 in. -8 in.	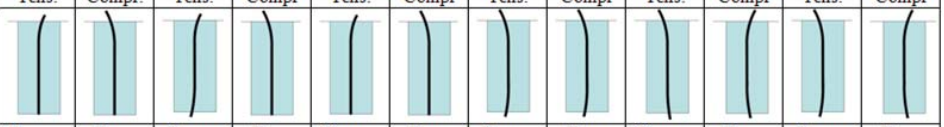											
		Compr.	Tens.	Compr.	Tens.	Compr.	Tens.	Compr.	Tens.	Compr.	Tens.	Compr.	Tens.
LB6-PT V18	0 in. -7 in. -8 in.	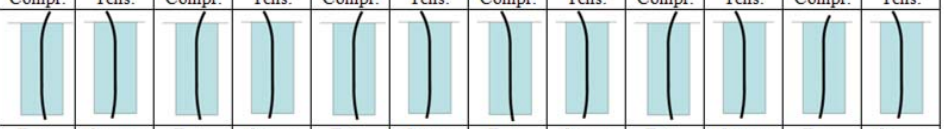											
		Tens.	Compr.	Tens.	Compr	Tens.	Compr	Tens.	Compr	Tens.	Compr	Tens.	Compr
LB7-PT V00	0 in. -7 in. -8 in.	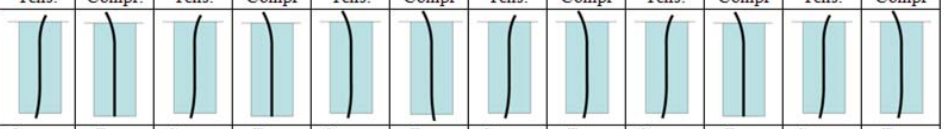											
		Compr.	Tens.	Compr.	Tens.	Compr.	Tens.	Compr.	Tens.	Compr.	Tens.	Compr.	Tens.
LB7-PT V18	0 in. -7 in. -8 in.